LEED and DLEED as modern tools for quantitative surface structure determination

1995 Rep. Prog. Phys. 58 637

(http://iopscience.iop.org/0034-4885/58/6/003)

Rep. Prog. Phys. 58 (1995) 637–704. Printed in the UK

LEED and DLEED as modern tools for quantitative surface structure determination

Klaus Heinz

Lehrstuhl für Festkörperphysik, Universität Erlangen-Nürnberg, Staudtstrasse 7, D-91058 Erlangen, Germany

Abstract

The last decade has seen remarkable new developments in the field of low energy electron diffraction (LEED) which are reviewed in the present paper. The arrival of sophisticated and fast techniques for the measurement of diffraction intensities in the early 1980s was a challenge to theory. Its answer was the development of tensor LEED (TLEED) in 1985. It allows the fast calculation of intensities for structures not too far from a certain reference. This made quantitative surface structure analysis approach new frontiers both with respect to structural complexity and—with the help of the routine use of reliability factors—to precision. Simultaneously, the new experimental techniques allowed access to two-dimensional intensity maps, i.e. the measurement of diffuse intensity distributions. Theory could be modified to calculate such distributions and so gave birth to the diffuse LEED technique (DLEED) which allows the retrieval of the local structure in case of disordered adsorption. The basics and the development of both TLEED and DLEED is reviewed. TLEED is the basis for direct methods and is used in effective search procedures for surface structures structurally close to a certain reference. It can also be used to simulate the substitution of surface atoms by different chemical species as well as to account for surface vibrations. In addition to carrying the information about the local structure, DLEED patterns very recently could be successfully interpreted in a holographic sense yielding real space images directly.

This review was received in February 1995.

0034-4885/95/060637+68$59.50

Contents

1. Introduction

Knowledge of the structure of a crystalline solid is essential for the qualitative and quantitative understanding of its physical and chemical properties. The same holds, of course, for the surface of a solid whose atoms, however, can deviate considerably from the arrangement expected from a mere bulk truncation. This makes *surface crystallography*, i.e. the quantitative investigation of surface structures, an important field already from a basic point of view. However, it gains an additional dimension if one realizes that a solid interacts with the outside world only through its surface. Phenomena like, e.g., corrosion, catalysis and epitaxy as well as the properties of, e.g., sensors and contacts are largely dominated by the surface and so by its structure. Consequently, knowledge of the latter is essential also from a practical point of view.

Deviations from the bulk structure are due to the truncation of chemical bonds during the formation of the surface by which atoms rearrange into new equilibrium positions. Similarly, new and additional chemical bonds offered by adsorbates can modify the structure of the surface, too. There may be only slight deviations such as, e.g., a few per cent change of interlayer distances (*multilayer relaxation*), but also drastic changes with symmetry- and/or bond-breaking movements of atoms (*surface reconstruction*). The depth down to which such relaxations or reconstructions take place is used to define the vertical size of the surface. This slab of atomic layers will be called *the surface* throughout this paper. It is obvious that the extension of this surface towards the bulk depends on the case under consideration and, of course, on the investigator's decision whether a faint atomic movement in some depth is negligible or not. In general, it is commonly accepted today that the surface consists of a slab of about 5–10 Å thickness.

Therefore, in order to retrieve the surface structure a method is needed which is structurally sensitive to a slab of atoms of this thickness. Fortunately, with *l*ow *e*nergy *e*lectron *d*iffraction (LEED) there is a tool at hand which fully meets this condition. Electrons in the energy range of typically 25–600 eV are elastically scattered back with sufficient intensity only from atoms within this thickness regime. This comes by strong inelastic losses mainly due to plasmon excitation which limits the electron penetration depth. The de Broglie wavelength corresponding to the energy range mentioned varies between about 0.5 and 2.5 Å, i.e. it is of the order of interatomic distances in a solid. Consequently, for a crystalline surface large diffraction angles result which lead to well separated and sharp diffraction spots whose intensities carry the structural information wanted. This makes LEED an almost ideal tool for the retrieval of surface structures.

Of course other methods working with electrons in this energy range should be suitable, too. This is true for, e.g., *p*hoto-*e*lectron *d*iffraction (PED), but the necessary experimental efforts exceed those for LEED by far because a dedicated x-ray source is needed in order to sweep the energy. The same holds for *s*urface *e*xtended *x*-ray *a*bsorption *f*ine *s*tructure measurements (SEXAFS) which, as an additional shortcoming, has access only to bond lengths rather than the full structure. Also, surface x-ray diffraction needs a strong synchrotron source whilst LEED manages with a simple electron gun operated in the home laboratory in a comparably inexpensive way. Among the home run techniques ion scattering is also a very valuable tool whereby, however, *l*ow *e*nergy

*i*on *s*cattering (LEIS) provides only limited structural accuracy whilst *h*igh *e*nergy *i*on *s*cattering (HEIS) shows only poor sensitivity to light adsorbates. The *s*canning *t*unnelling *m*icroscope (STM) provides a direct image of the surface (or more precisely of the surface electron density) but is sensitive only to the very first atomic layer. High voltage microscopy with atomic resolution suffers from severe restrictions of sample preparation and the same holds for *f*ield *i*on *m*icroscopy (FIM). Recent historical reviews with many references for the techniques described can be found in *Surface Science: The First Thirty Years* (Duke 1994a).

So, though being the oldest structural tool of surface science, LEED still plays a unique role in surface structure determination. A lion's share of the about 1000 structures known today were solved by LEED. The technique is inexpensive and provides the full structure of the surface rather than, e.g., only bond lengths or top layer atomic arrangements. As always, unique properties have their price: due to their large scattering cross section electrons are multiply scattered until they leave the surface. This makes the kinematic description of diffraction fail, a full dynamical treatment is necessary. The corresponding theory was ready for application in the early 1970s marking the start of *surface crystallography*. The availability of an accurate theory soon proved the necessity for more reliable experimental data. This launched the development of improved intensity measurement techniques which were realized on the basis of video cameras or channel plates as detectors. They allowed access to more complex structures which in turn put new demands on theory. Structural search procedures and even a new and powerful perturbation method for the computation of intensities (*tensor* LEED) were developed. Also, the usual restriction of LEED to long range order was lifted for the case of disordered adsorption on a crystalline surface. With the measurement and full dynamical calculation of diffuse intensity distributions (*diffuse* LEED = DLEED) local adsorption structures became accessible.

The present paper reviews this development and the current status of LEED and DLEED. Emphasis is on the measurement and computation of dynamically determined intensities, i.e. the kinematic analysis of spot profiles is left out. After a short outline of the basics of LEED in the next section, todays sophisticated measurement techniques are described. Section 4 presents the DLEED method followed by a description of the idea, design and potential of tensor LEED. Efficient procedures to find the correct structure from measured intensities are described in section 6 and examples for the structural complexity and precision accessible today are presented in section 7. It will become evident from sections 3–7 that modern LEED and DLEED give access to both ordered and disordered structures of considerable complexity. The structural precision can reach values as low as 0.01 Å for atomic positions of not too complex structures but usually decreases with increasing complexity. Section 8 reviews a more recent development according to which diffuse diffraction patterns may be interpreted in a holographic sense. The final section offers a critical resumé and outlook.

2. Low energy electron diffraction: basic principles

2.1. Basic experimental design

In principle the LEED experiment is very simple and is described only very shortly in the following (for more detailed presentations see Clarke 1985, Ertl and Küppers 1985, Heinz 1988, Henzler and Göpel 1991, Jona *et al* 1982, Van Hove *et al* 1986, Walls

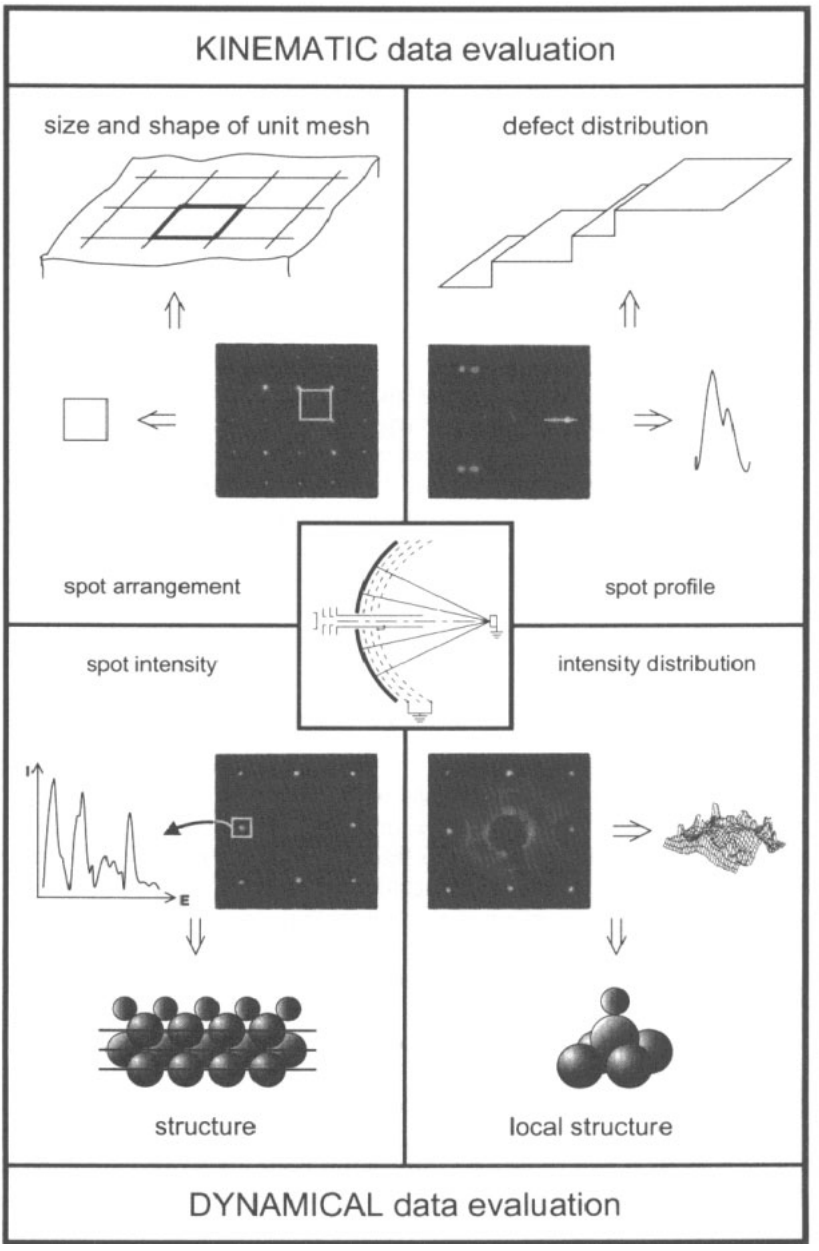

Figure 1. Informational content of LEED patterns and procedures of data evaluation.

1989, Woodruff and Delchar 1986). An electron beam of energy E and momentum $\boldsymbol{k}_i$ is made to impinge on the surface of a crystalline solid. Due to the translational periodicity parallel to the surface elastically back scattered electrons can appear only in directions defined by the surface parallel momentum $(\boldsymbol{k}_{i\|} + \boldsymbol{g})$ where $\boldsymbol{g}$ is a reciprocal lattice vector parallel to the surface as defined by the symmetry of the surface lattice. As displayed in the centre of figure 1, these beams are made to hit a luminescent screen after having

passed an additional accelerating voltage applied between a transparent grid near the screen. Additional grids make the space between sample and the near screen region field free in order to allow for free electron travelling and repel inelastically scattered electrons. So, for a well ordered surface the beams generate bright diffraction spots on the screen with some only low diffuse background due to quasielastic scattering by phonons or defects. For an ideally ordered surface the size of the spots is determined by the quality of the electron gun whose electrostatic lenses make the electron beam focus on the screen. The spot is an image of the electron source, i.e. the emitting area of the gun cathode. As this is of finite extension, the spot must have a corresponding width which is indeed observed. Equivalently, this can be described by the finite spatial coherence of the primary electron beam which for most guns is of the order of 100 Å but can be increased by about an order of magnitude by specially designed electron optics (Lagally and Martin 1983, Henzler 1985a, Scheithauer *et al* 1986). Of course, the finite energy width of the primary electron beam due to the thermal emission of electrons from the cathode, which can be equivalently described by the beam's time coherence, also adds to the spot width, but usually this is of minor importance. The whole experiment must be carried out in ultrahigh vacuum (UHV) with a residual gas pressure of typically 10^{-10} mbar or less. This is necessary to keep the surface under investigation clean during the LEED experiment and was a major difficulty in the early days of surface science. Fortunately, today effectively working pumps are available so that UHV conditions can be realized in a routine way.

2.2. *Informational content of the diffraction pattern*

Due to the translational symmetry of a crystalline surface the geometrical arrangement of the diffraction spots is equivalent to a surface parallel cut through the reciprocal lattice of the surface. Therefore, the unit mesh of the pattern is identical to the surface parallel unit mesh of the reciprocal lattice described by vectors $\boldsymbol{g}_1$ and $\boldsymbol{g}_2$. By Fourier inversion, the real space unit mesh vectors of the surface lattice result, $\boldsymbol{a}_1 = 2\pi(\boldsymbol{g}_2 \times \boldsymbol{n})/A_g$ and $\boldsymbol{a}_2 = 2\pi(\boldsymbol{n} \times \boldsymbol{g}_1)/A_g$ with $\boldsymbol{n}$ the unit vector normal to the surface and $A_g = |\boldsymbol{g}_1 \times \boldsymbol{g}_2|$ the area of the surface reciprocal unit mesh. So, for well ordered surfaces exhibiting sharp spots the diffraction pattern gives easy access to the size and shape of the real space unit mesh. This is indicated in the upper left frame of figure 1.

However, knowledge of the unit mesh must not be confused with knowledge of the structure, i.e. the position of atoms within the unit mesh. This results only from evaluation of spot intensities. In principle this could be done for a single energy and direction of incidence of the primary beam if a sufficiently large number of spots are available. However, in most cases this data base is too poor for a safe extraction of the structure information. Fortunately, it can be easily enlarged by variation of either the angle of incidence or the energy of primary electrons, or both. As angles of incidence are difficult to control and reproduce with high accuracy, today in most cases intensities are taken as a function of the electron energy and for normal incidence of the primary beam. The electron energy E is easy to vary by a suitably applied voltage V. Normal incidence can be checked and adjusted with high precision by comparison of intensities of symmetrically equivalent diffraction beams. So, the data base used nowadays for surface structure determination by LEED consists of intensity versus energy spectra for a set of different diffraction beams, so-called $I(E)$ spectra or I–V curves.

Unfortunately, the evaluation of intensity data to yield the surface structure is not as easy as in case of x-ray diffraction. There, the cross section for photons scattered by

the electrons of an atom is very small compared to the geometric cross section of the atom. So, photons are scattered only once—if ever—and the diffraction amplitude is the Fourier transform of the electron charge distribution in the sample. However, the cross section for electron–atom scattering is of the order of the geometric cross section. Consequently, within an atomic cluster of the size of the electron attenuation length there is a high chance that electrons are multiply scattered before they leave the surface. So, the first Born approximation leading to the Fourier transform for the diffraction amplitude breaks down. A full dynamical theory is necessary to retrieve the surface structure as indicated in the lower left panel of figure 1. The theory and corresponding computer codes were developed in the late 1960s and early 1970s, which period of time marks the start of quantitative surface crystallography by LEED. Detailed descriptions and reviews have been published repeatedly (Pendry 1974, Tong 1975, Van Hove and Tong 1979, Van Hove *et al* 1986, Jona *et al* 1982, Heinz 1988) and the history of this development was illuminated only recently (Duke 1994b, Marcus 1994, Pendry 1994, Tong 1994, Van Hove and Somorjai 1994). So, it will be sufficient to concentrate here only on the essentials (section 2.3).

The scattering scenario described so far is largely incomplete as we have assumed that the surface is characterized by ideal long range order. In experimental reality, however, the surface of a crystal may exhibit various static structural defects of different dimensionality as vacancies (or adatoms), steps and facets. Moreover, even in case of an ideal surface, adsorption of adatoms or molecules on the surface may not lead to long range order. It possibly may end with, e.g., statistically adsorbed species or with the formation of differently ordered but finite adsorption islands which may or may not be mutually in phase. For both clean and adsorbate covered surfaces thermal vibrations must be considered additionally as dynamical defects. Generally, any deviation from long range order leads to background intensities and affects the intensity and/or shape of the diffraction spots. So, as indicated in the upper right panel of figure 1 the existence of steps separating terraces on a surface leads to spot broadening and/or splitting. The shape of the spot and its energy dependence reflects the defect distribution on the surface. If the size of the defect (here the terrace width) is large compared to the electron attenuation length, which defines the size of the atomic cluster within which multiple scattering takes place, the defect distribution can be retrieved by kinematic evaluation for which reference is made to the literature (Henzler 1985b, 1993, Lagally 1985). However, if the size of the defect becomes gradually smaller the broadening of the spot increases correspondingly until covering the full diffraction screen and a diffuse intensity distribution results. This is in particular true for statistically adsorbed species which give rise to a diffuse LEED pattern (DLEED) superimposed on the sharp Bragg spots caused by the crystalline substrate This situation is displayed in the lower left panel of figure 1. When all species adsorbed reside in statistically distributed but locally identical adsorption sites (*lattice gas disorder*) the distribution of the diffuse intensities on the screen reflects the local adsorption structure. As there is strong multiple scattering between the adatom and the neighboured substrate atoms again a full dynamical analysis is necessary to retrieve this local structure. This case will be illuminated in more detail in section 3.

As indicated in the upper part of figure 1, the size and shape of the surface unit mesh as well as the distribution of extended defects can be retrieved by kinematic evaluation. If the structure is wanted, however, for both present and missing long range order a dynamical evaluation of intensities is necessary as indicated in the lower part of figure 1. As this review concentrates on the latter case we sum up the essentials of standard intensity calculations in the following.

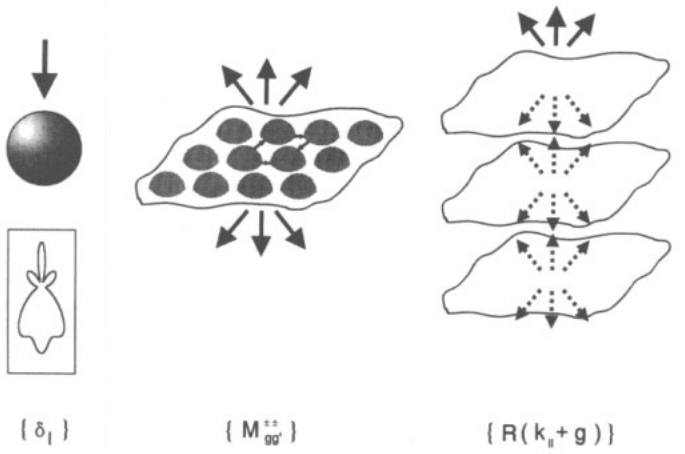

Figure 2. Hierarchy of dynamical LEED intensity evaluation.

2.3. Standard dynamical intensity calculations and reliability factors

As argued above the computation of diffraction intensities must consider multiple scattering due to the large cross section for electron–atom scattering. Though the total of scattering events is complex the calculations can be organized in a clear way by following the hierarchical scheme as displayed in figure 2. First, the scattering of the electrons by a single atom is calculated. Then the atoms are arranged to form an atomic layer for which layer diffraction matrices are computed. Finally, the layers are stacked to a crystal to yield the total reflection matrix of the surface.

The single atom scattering results from solution of the Schrödinger equation assuming an atomic potential of spherical symmetry and finite spatial extension. The radius of the sphere is usually defined so that neighbouring spheres touch each other. Electron orbitals extending over the sphere are redistributed inside the sphere. In the area between atomic spheres the potential is kept constant described by the real part of the inner potential V_{0r}. It adds to the electron energy when the electron enters the solid, so its total kinetic energy within the surface is $E_i = E + V_{0r}$. For an atomic layer the potential looks like an arrangement of muffin tins (see centre part of figure 2), from which the expression *muffin-tin potential* arises. Of course the spherical symmetry of the atomic scattering potential is an approximation only, as the atom is embedded in an arrangement of non-spherical symmetry. However, this approximation works well for LEED energies. These are so much above the Fermi energy that scattering is dominated by the (spherically symmetric) inner electron shells and the nucleus of the atom. Due to the spherical symmetry the scattering is best described in the angular momentum presentation resulting in a set of phaseshifts δ_l with l cut off at a certain maximum value l_{max}. For higher values of l the phaseshifts are assumed to be negligible, thus $l_{max} \approx kR$ with R the radius of the atomic sphere is usually a good approximation. It should be pointed out that by solution of the Schrödinger equation, the phaseshifts fully describe the multiple scattering within the atom.

The scattering within an atomic layer is also described in the angular momentum presentation. Scattered spherical waves outgoing from a certain atom are expanded in spherical waves with respect to the atomic position of a neighbouring atom in order to

account for multiple scattering. As this neighbour may scatter back to the original atom a self-consistent solution of the total sum of the scattering processes is required. This is equivalent to the inversion of a matrix whose dimension scales with $l_{\max}^2$. Calculation and inversion of this matrix usually requires the major part of the computing time. For the total diffraction from a layer of atoms a representation in momentum space is appropriate because of the translational symmetry. Therefore, the sum over all dynamical atomic scattering amplitudes is developed in a set of plane waves with surface parallel momenta $(\boldsymbol{k}_{i\|}+\boldsymbol{g})$ producing layer diffraction amplitudes $M_{gg'}^{\pm\pm}$ where the $\pm$ signs indicate the direction of incoming and outgoing plane waves. Eventually, the matrices $M_{gg'}^{\pm\pm}$ are used to stack the layers in order to produce the full surface diffraction. Of course multiple diffraction between layers has to be accounted for which again leads to the inversion of a matrix. It is sufficient to couple neighbouring layers step by step so that by each matrix inversion the number of layers can be doubled (*layer doubling scheme* (Pendry 1974)). The dimension of the matrix is determined by the number of propagating plane waves for which a natural cut-off is the Ewald sphere, so that $|\boldsymbol{g}| \leqslant k$ results. However, as attenuated waves also couple between neighbouring layers, more beams have to be considered. When the layer spacings are well above about 1 Å one can avoid the matrix inversion and profit from the fact that forward diffraction of a layer (described by $M_{gg'}^{++}$ or $M_{gg'}^{--}$) normally dominates over back diffraction (described by $M_{gg'}^{+-}$ or $M_{gg'}^{-+}$). The corresponding approximative procedure is known as *renormalized forward scattering* (Pendry 1974).

While travelling within a solid an electron undergoes inelastic processes dominated by plasmon excitation by which it disappears from the elastic channel. This can be described by the imaginary part of the inner potential, the so called optical potential V_{0i} which is of the order of 4–5 eV at 100 eV and is slightly energy dependent ($V_{0i} \propto E^{1/3}$) is usually a good approximation (Van Hove and Tong 1979, Van Hove *et al* 1986)). So, the total inner potential is complex, $V_0 = V_{0r} + \mathrm{i}V_{0i}$. This with $\frac{1}{2}k^2 = E + V_0$ (atomic units) results in an imaginary part of the wavenumber, $k_i \approx V_{0i}/k_r$ with $k_r \approx (2E + 2V_{0r})^{1/2}$ for $V_{0i} \ll (E + V_{0r})$. Consequently, spherical and plane waves described by $\exp(ikr)$ and $\exp(i\boldsymbol{k}\cdot\boldsymbol{r})$, respectively, are attenuated whilst travelling. Of course, quasielastic scattering by phonons also removes electrons from the coherent elastic channel. This can be described by a Debye–Waller factor which reduces the atomic scattering factor for a finite temperature to $t(E, T) = t(E, 0)\ \exp(-\frac{1}{2}\Delta k^2 \langle u^2 \rangle)$ with Δk the modulus of the electron's momentum transfer and $\langle u^2 \rangle = \langle (u(T))^2 \rangle$ the mean square atomic displacement due to atomic vibrations at temperature T. The simple relation between t and the δ_l, $t(E, 0) = (k)^{-1} \sum_l (2l+1) \sin \delta_l \exp(\mathrm{i}\delta_l)\ P_l(\cos \vartheta)$ with ϑ the scattering angle, allows simulation of the Debye–Waller factor by complex phaseshifts $\delta_l(T)$. This is a simple way to consider thermal vibrations also for multiple scattering processes though this description is not fully exact.

The proper choice of the atomic scattering also allows the description of the diffraction from substitutionally disordered alloys. In these crystals the different atomic species are statistically distributed over the crystallographic sites, i.e. in a strict sense the translational symmetry is broken though it holds from the mere geometrical point of view. Nevertheless, it turns out that the above procedures to calculate intensities can still be applied. This is consistent with the experimental observation of sharp diffraction spots and a low level of homogeneously distributed background. It is sufficient to use an average t-matrix (Gauthier *et al* 1985) which can even be made layer dependent. In this *average t-matrix approximation* (ATA) the scattering matrix of the average scatterer in the jth layer can be written as $t_j^{\mathrm{ATA}} = c_j t^{\mathrm{A}} + (1 - c_j) t^{\mathrm{B}}$, where t^{A} and t^{B} are the t-matrices

of atomic species A and B and c_j is the concentration of species A in the jth layer. This procedure works remarkably well as has been shown by numerous applications to experimental data (for reviews see Gauthier and Baudoing 1990, Bardi 1994) as well as by theoretical investigations (Crampin and Rous 1991). Of course, it can also be easily applied to ternary and higher order alloys or other disordered compounds. Also, substoichiometric compounds can be handled by mixing with vacancies (Gauthier *et al* 1990). So, besides the geometrical parameters of the surface, the layer-dependent chemical stoichiometry can also be determined by LEED. This holds, if the scattering properties of the different species differ sufficiently, while the sensitivity decreases with increasing layer depth as usual. However, similar to geometrical changes within a layer a new and time consuming self-consistent calculation of the layer diffraction matrix is necessary with each change of the layer stoichiometry. Fortunately, there is an elegant way out of this problem as will be demonstrated in section 5.2.

How close can today's intensity calculations reproduce experimental data? Figure 3 gives an impression for a selected beam of clean metal surfaces of increasing openness, i.e. FCC(111), BCC(110), FCC(100), FCC(110), BCC(211) and FCC(311). Apparently, there is very close resemblance of the curves with respect to both peak positions and heights. It belongs to the best achievable today. In order to measure the agreement between curves quantitatively, so-called reliability factors (R-factors) are widely used today. Due to the complex structure of the spectra, different concepts for the construction have been followed in the past leading to a variety of different R-factors (for a survey see Van Hove and Koestner 1984, Van Hove *et al* 1986). Today, the relative mean square deviations of intensities (R_2) or the Pendry R-factor (R_p) are mostly used. In both cases the summation is over all intensities $I_g(E_i)$ taken for different beams g and at different energies E_i. So, R_2 simply results by $R_2 = \Sigma_{i,g} (cI_{cal} - I_{exp})^2 / \Sigma_{i,g} (I_{exp})^2$, where c is the average normalization constant between experimental and calculated spectra. The Pendry R-factor (Pendry 1980) is more sophisticated and follows the idea that maxima and minima in the spectra are the important features. Their positions come by constructive or destructive interference which depends both on the electron wavelength and the pathlength difference between different interfering diffraction processes. Therefore, emphasis is on the positions of maxima and minima rather than on the absolute height of intensities (though in case of overlapping peaks there is also some sensitivity with respect to peak heights). So, instead of the intensities their logarithmic derivative with respect to energy is used, $L = (\partial I/\partial E)/I$. As for small intensities this is very sensitive to experimental errors, the bounded function $Y = L/[1 + (LV_{0i})^2]$ is used instead of L. The Pendry R-factor then simply results as the mean square deviations of Y functions rather than of the intensities as in the case of R_2, i.e. $R_p = \Sigma_{i,g} (Y_{cal} - Y_{exp})^2 / \Sigma_{i,g} (Y_{cal}^2 + Y_{exp}^2)$. Ideal agreement corresponds to $R_p = 0$, uncorrelated spectra yield $R_p = 1$ and anticorrelated curves produce $R_p = 2$. For the cases displayed in figure 3 the beam averaged values of R_p are very low and best for Cu(100), i.e. $R_p = 0.08$. Apparently, this numerical level of R_p corresponds to an excellent visual comparison, too. The variance of the Pendry R-factor $\mathrm{var}(R_p) = R_{p,min} (\Delta E/8V_{0i})^{1/2}$ with ΔE the energy width of the total data base, allows estimation of the error limits for the model parameters determined (Pendry 1980). All sets of parameters which produce spectra with $R_p \leqslant (R_{p,min} + \mathrm{var}(R_p))$ cannot be excluded to account for the correct model. However, this error estimation is based on statistical errors only and leaves systematic errors—both in theory and experiment—unconsidered. This is due to the fact that almost nothing is known about the latter.

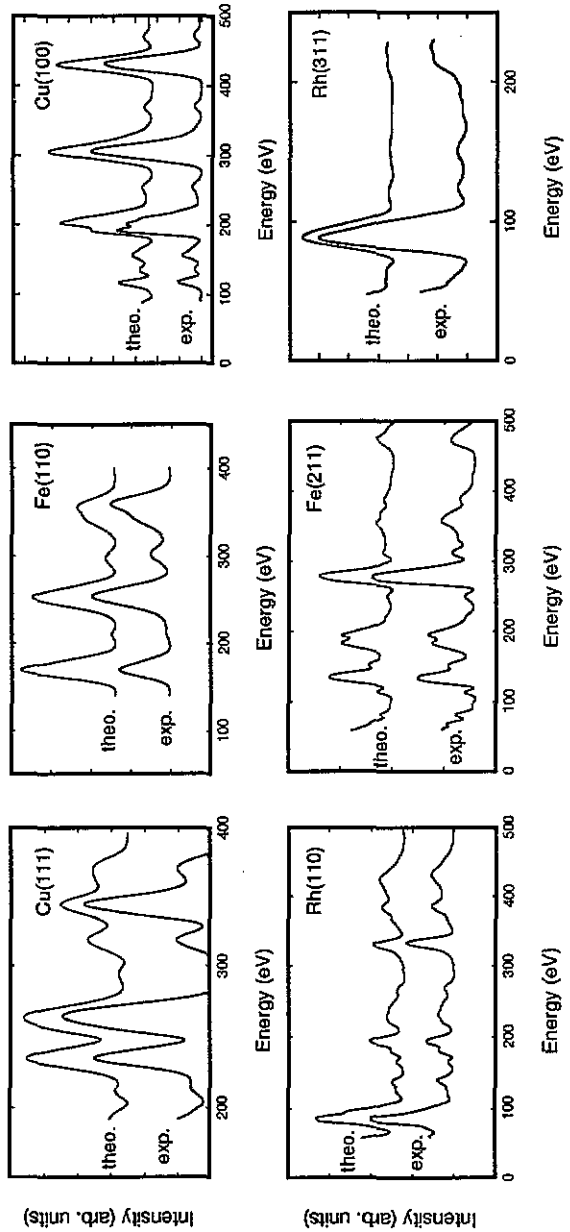

Figure 3. Comparison of experimental and calculated $I(E)$ spectra for selected beams diffracted at normal incidence and 90 K from surfaces with increasing openness, namely Cu(111), Fe(110), Cu(100), Rh(110), Fe(211) and Rh(311).

3. Modern data acquisition: high speed, sensitivity and accuracy

Before experimental data can enter the procedure of structural analysis they need to be carefully measured. Clearly, as a diffracted beam corresponds to an electron current the direct way would be the direct measurement of this current. In fact this has been done for a long time using a Faraday cup within the UHV equipment. However, as the beam moves with the energy sweeping the cup must be made to follow this movement. As this has to be realized under the conditions and restrictions imposed by UHV this tracking procedure turns out to be tedious and time consuming. Moreover, two reasons demand a fast measurement. First, during the measurement the surface under investigation must be kept in the status wanted, i.e. either clean or covered only by the adsorbate wanted. However, there is always residual gas adsorption even under good UHV conditions. So, for, e.g., a base pressure of 10^{-10} mbar and a 1 h measurement time as much as a full monolayer of gas atoms or molecules can adsorb on the surface. This disturbs the required signal seriously. A second reason demanding fast measurements is the damaging influence of the primary electron beam, by which adsorbed molecules can be cracked or made to desorb. Of course, this can only be avoided by a sufficient reduction of the total electron dose necessary to collect the intensity data. Though this can be partly achieved by an increased speed of measurement, there is still need for additional reduction of the primary current for very sensitive adsorbate systems.

Therefore, starting in the mid-1970s, various new techniques were developed in order to speed the measurement up and to reduce the electron dose (for reviews see Heinz and Müller 1982, Jona *et al* 1982, Heinz 1988). The directions followed were twofold. Higher speed was achieved by the measurement of the light generated on a luminescent screen from outside the UHV equipment. Additional to speed, however, the use of channel plates for the amplification of the diffraction beam currents allowed the reduction of the primary beam current and so, correspondingly, the total electron dose. Today, mainly two techniques have survived which are described in the following.

3.1. Video based methods

Though their technical realization can be sophisticated, video based measurement techniques are simple in principle (figure 4). The diffraction pattern is generated on a luminescent screen, whereby modern equipments are provided with glass screens, so that observation can be from the back (*back view optics*) allowing for rather bulky sample holders. A TV camera views the pattern from outside the UHV apparatus and makes it appear on a monitor. In parallel, the video signal is passed to a computer for digitization and data evaluation where an interface ('AUTOLEED unit' in figure 4) provides a fast analogue–digital converter. Various modifications of this technique have been used to date since the first implementation of the method (Heilmann *et al* 1976). They can differ by the speed of the camera (slow scan, TV rate scan), the speed of digitization (on-line or slower) and/or the evaluation method of the digitized data (Lang *et al* 1979, Welkie and Lagally 1979a, b, Leonhard *et al* 1980, Carvalho *et al* 1984, Müller and Heinz 1985, Jona *et al* 1985, Anderegg *et al* 1986, Heinz 1988, Guo *et al* 1990, Adams *et al* 1991).

The Erlangen version of the video system (Müller and Heinz 1985, Heinz 1988), which is among the fastest and is commercially available, uses a standard TV camera. It can be replaced by an image intensifier camera if this becomes necessary in order to measure low signals. The video half-frame can be digitized and stored on-line producing

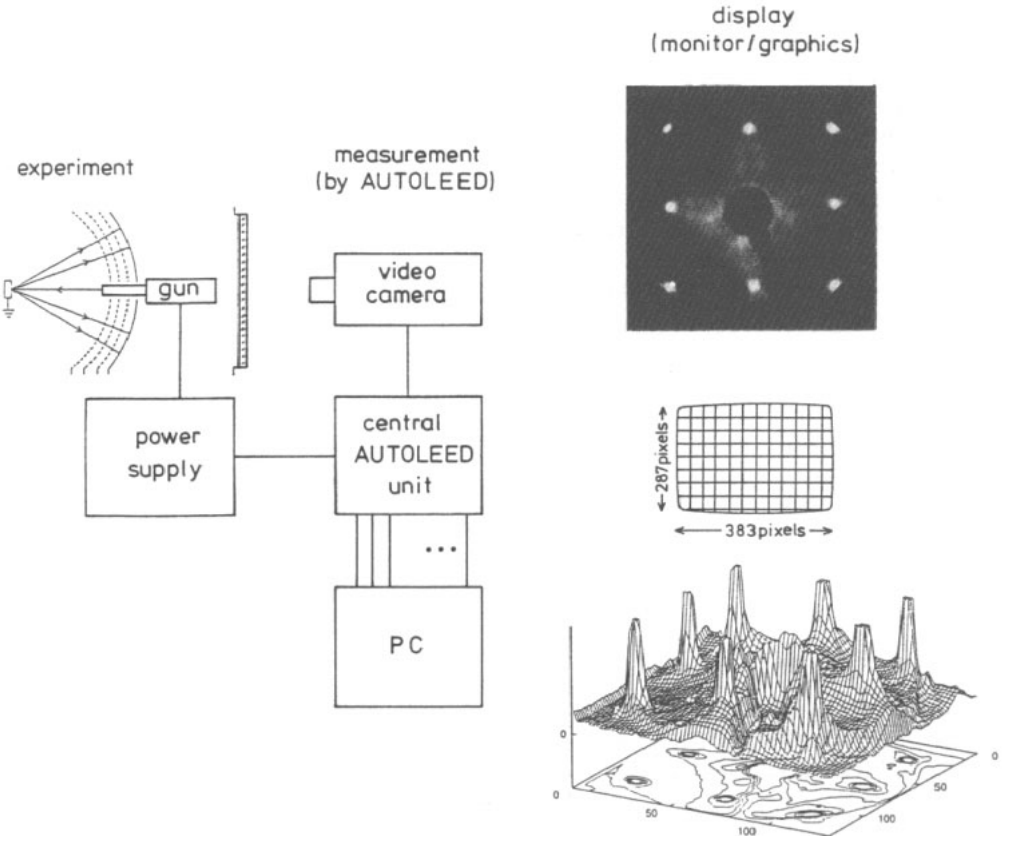

Figure 4. Schematic design of video methods for fast intensity measurements.

an array of 383 × 287 intensity pixels. A three-dimensional plot of a typical half-frame image is displayed in the lower right part of figure 4. However, any subset of data can also be recorded by defining a certain rectangular electronic window within which the intensity distribution is wanted. The window can degenerate to form a slit by which the spatial intensity profile along the slit results. For the measurement of $I(E)$ spectra a square window is chosen and made to frame the spot wanted. The computer determines the average background level at the window's edges and uses this to correct the data within the window. Subsequently, the resulting intensity distribution is integrated to yield the spot intensity. This on-line data evaluation avoids the memory consuming storage of the full image. During integration the position of the intensity maximum is also determined. This is done at each energy, so that by centring the window around the maximum position the software follows the spot automatically when it moves with the energy sweeping under computer control. For each energy all the operations described are completed within a video half-frame (20 ms, European norm). Thus the measurement of a single spot intensity takes 20 ms, i.e. a spectrum of, e.g., 300 intensity–energy points results within 6 s. In order to improve the signal/noise ratio a number of subsequent video half-frames can be added at each energy, the total measuring time increasing accordingly. Of course the latter also scales linearly with the number of beams to be measured. In its newest commercially available version the Erlangen system

is controlled by a 66 MHz 80486 CPU where the software guides the operator by self-explaining menus. An example is given in figure 5, which also contains the full size image of a digitized diffraction pattern. In addition the intensity profile along a certain cut through the image is displayed.

The number of beams necessary for a structure determination is typically of the order of 10 which at minimum requires a total measuring time of about 100 s if one allows for some time for the initial adjustment of the LEED system. At a primary current of typically 1 μA mm^{-2} this leads to an electron dose of about 10^{-4} A s mm^{-2} equivalent to about 10^{15} electrons/mm^2. With the application of an intensifier camera the primary beam current and so the total dose can be reduced by about one to two orders of magnitude. Another order of magnitude can be gained by storage of the TV frames on video tape at each energy and subsequent off-line evaluation. In this case there is no scaling of the total measuring time with the number of beams wanted. Yet, even doses of the order of 10^{12}–10^{13} electrons/mm^2 can still be too large and can make molecules at the surface crack or desorb. Such electron sensitive molecules, in particular organic species, require the application of methods which use much lower primary beam currents.

3.2. *Channel plate methods*

Channel plates with their large amplification for electrons were used quite early in LEED though only occasionally such as, e.g., in front of the usual screen (Chinn and Fain 1976) or with the additional use of an optical multichannel analyser (Welkie and Lagally 1979, Weeks *et al* 1979). However, full image intensity maps had to be stored on disk for later off-line evaluation to yield integrated beam intensities. Both the time and memory needed to store these vast amounts of data were rather large so that routine applications had to await faster computers with cheaper memory. In the meantime dual channel plates (chevrons) were introduced (Stair 1980) allowing for gains even higher than 10^7. The display type screen was replaced by position sensitive devices such as the resistive anode or the wedge-and-strip anode (Martin *et al* 1981) which allowed the acquisition of digitized intensity maps by computer evaluation of their signals (McRae *et al* 1985, McRae and Malic 1986).

The most sensitive system currently and routinely used is that developed by the Berkeley group (Blackman *et al* 1988, Ogletree *et al* 1991). Using a chevron combined with a position sensitive anode and digital electronics for electron counting ('digital LEED', figure 6) primary currents lower than 1 pA can be allowed. Depending on the intensity level the measurement of a single energy intensity pattern takes 10–300 s for a reasonable signal/noise ratio. This is much larger than the value needed by the 'TV methods even if one takes into account the fact that the measurement of the full pattern contains information on all beams at once. Nevertheless, the total electron dose is up to three orders of magnitude lower even if the TV method uses an intensifier camera. However, as the images have to be evaluated off-line the method lacks the immediate availability of intensity spectra provided by the TV method. So, there is no immediate feedback to the experimentalist in order to allow for the adjustment and correction of experimental parameters. This price has to be paid for the measurement of extremely sensitive adsorption systems not accessible by other LEED measurement techniques.

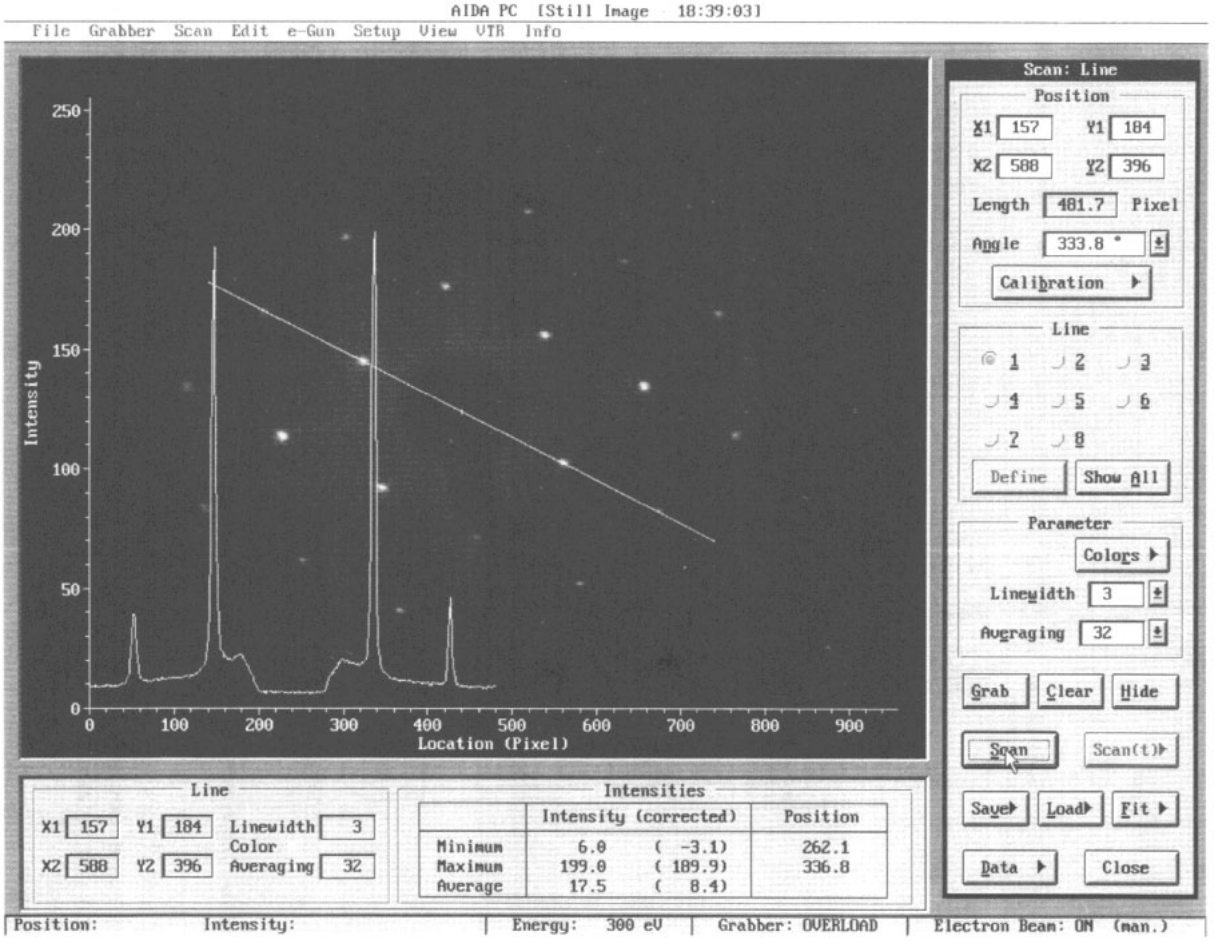
AIDA PC [Still Image 18:39:03]
File Grabber Scan Edit e-Gun Setup View VTR Info
Intensity
Location (Pixel)
Scan: Line
Position
X1 157 Y1 184
X2 588 Y2 396
Length 481.7 Pixel
Angle 333.8 °
Calibration
Line
1 2 3
4 5 6
7 8
Define Show All
Parameter
Colors
Linewidth 3
Averaging 32
Grab Clear Hide
Scan Scan(t)
Save Load Fit
Data Close
Line
X1 157 Y1 184 Linewidth 3
X2 588 Y2 396 Color Averaging 32
Intensities
Intensity (corrected) Position
Minimum 6.0 (-3.1) 262.1
Maximum 199.0 (189.9) 336.8
Average 17.5 (8.4)
Position: Intensity: Energy: 300 eV Grabber: OVERLOAD Electron Beam: ON (man.)

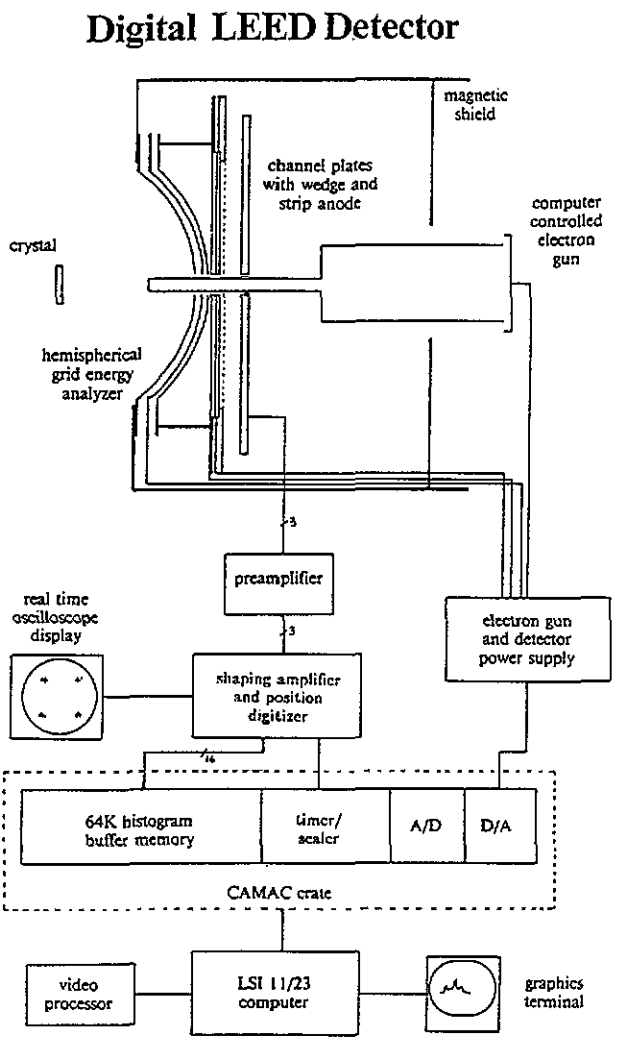

Figure 6. Schematic design of the Berkeley digital LEED system.

3.3. Data improvement and new kinds of data

By the examples given in figure 3 the impressive agreement reachable between experiment and theory has been demonstrated. Of course, this demands reliability of both experimental and theoretical data. Though many mistakes can be made in the process of data computation, experimental data seem to run a higher risk of being unreliable. As mentioned, they are sensitive to residual gas adsorption and electron stimulated desorption or cracking of adsorbates. It was demonstrated above that the fast and low dose methods have largely overcome these difficulties. However, intensity data are also extremely sensitive to more basic parameters such as sample misalignment and incorrect or incomplete background correction. It is also by the new fast methods of data acquisition that the related errors of measurement can be avoided or largely reduced. This is because these methods allow the easy repetition of measurements for different experimental parameters which can be varied to find the most accurate choice. So, spectra of

symmetrically equivalent beams can be used to adjust for precise normal incidence. This is routinely done ahead of the final experiment by repeated measurement of the spectra, their quantitative *R*-factor comparison and stepwise correction of the sample alignment towards normal incidence. Eventually, the equivalent spectra are averaged which reduces the influence of some residual misalignment and improves the signal-to-noise ratio. Of course this method of data improvement requires the measurement of several beams—a tedious task when a Faraday cup or spot photometer is used. With the fast and automated methods at hand, however, these additional measurements can be done with ease and are routinely performed in current structure analyses. In general, the fast and low dose methods have opened access to highly reliable experimental data.

Yet, the new techniques of data acquisition also allow for new kinds of measurement and a few examples are given in the following. Instead of the electron energy an automated method can also control other external parameters, e.g. the sample temperature. So, temperature-dependent measurements can be performed whereby both integrated intensities or spatial spot profiles can be measured. This gives access to intensities for

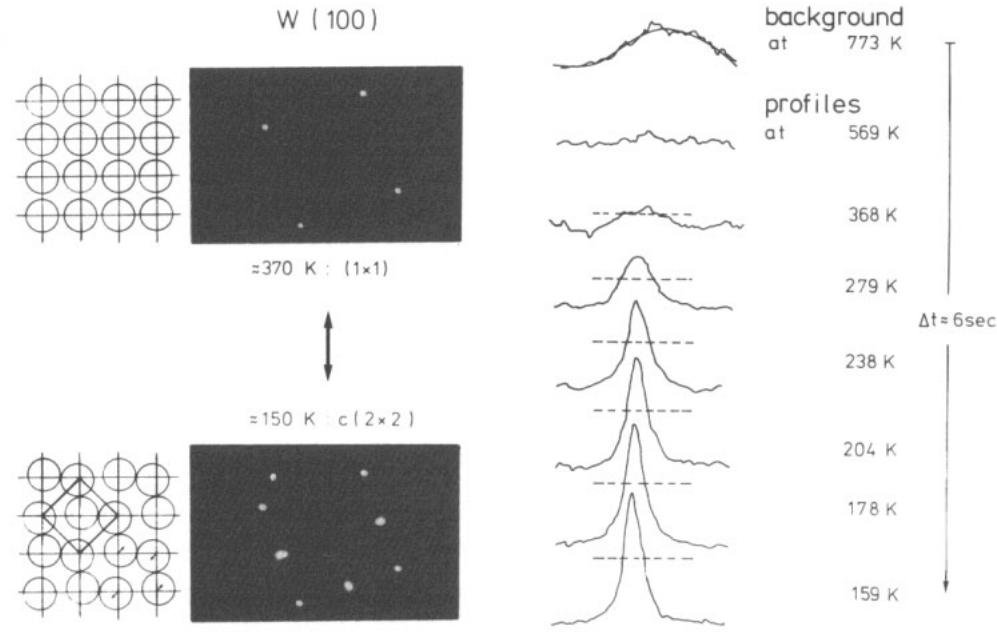

Figure 7. Structural transition $1 \times 1 \rightarrow c(2 \times 2)$ of W(100) by a temperature quench monitored by profiles of the $\frac{1}{2}\frac{1}{2}$ spot. The background determined at 773 K is subtracted from data taken at lower temperatures (Heinz and Müller 1982).

temperature controlled phase transitions. As an example, figure 7 displays the background corrected spatial profile of a superstructure spot which develops during the temperature controlled $1 \times 1 \rightarrow c(2 \times 2)$ phase transition of W(100) (Heinz and Müller 1982). The spot sharpens during the transition due to the growth of reconstructed islands on the surface. For structural phase transitions in adsorbates the temperature- and coverage-dependent intensities can be used to determine the phase diagram of the adsorbate system. The appearance (disappearance) of superstructure spots when entering (leaving) a certain structural phase can be used to determine the phase boundaries. As demonstrated in figure 8 for the system H/Rh(110), rather complex phase diagrams

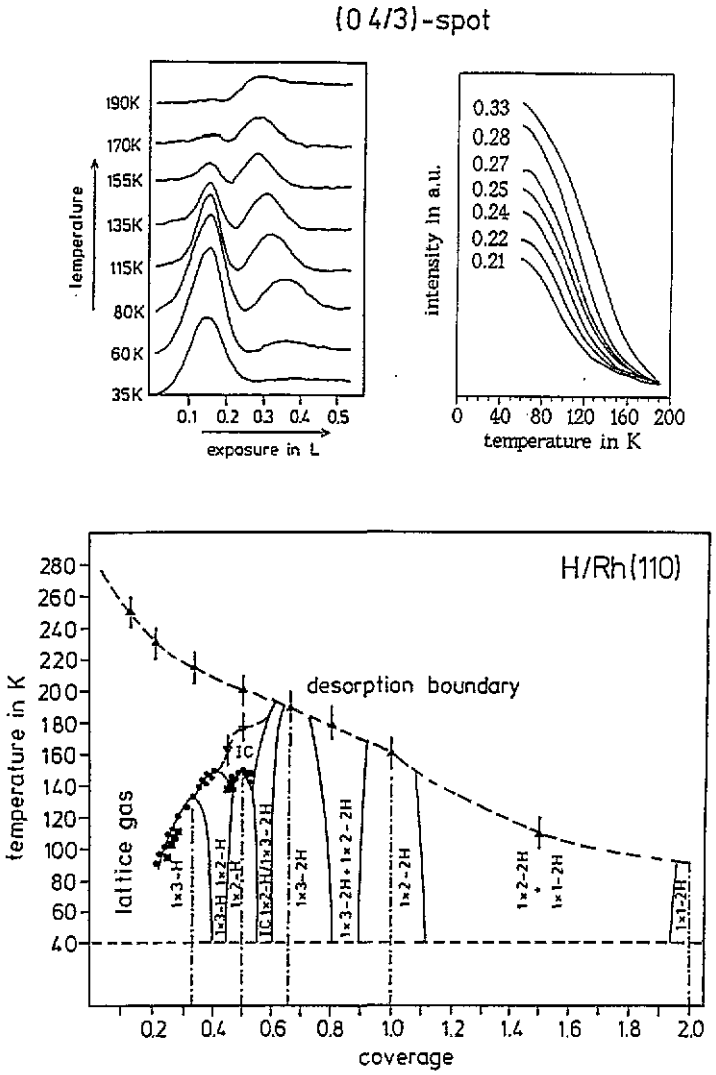

Figure 8. Phase diagram of H/Rh(110) (bottom) as determined by the variation of superstructure spot intensities when phase boundaries are crossed as function of temperature or coverage a displayed at the top for the $0\frac{4}{3}$ spot (after Nichtl-Pecher *et al* 1991, Nichtl-Pecher 1990).

can be determined in this way (Nichtl-Pecher *et al* 1991). Moreover, the high speed of measurement also allows time-resolved measurements, giving access to the kinetics of phase transitions. In this case the external control parameter simply is time, i.e. a certain beam is repeatedly measured while time runs. As an example, figure 9 displays the kinetics of the transition $1 \times 1 \rightarrow 5 \times 1$ of Ir(100), i.e. from the bulk terminated structure to a heavily reconstructed top layer (Heinz *et al* 1985a). From the thermodynamically stable 5×1 phase the metastable 1×1 phase can be prepared by careful gas adsorption and desorption and thermal treatment as described in the left part of figure 9. The kinetics of the transition can then be monitored subsequent to a flash to elevated temperatures. In an activated process superstructure spots develop at the cost of integer

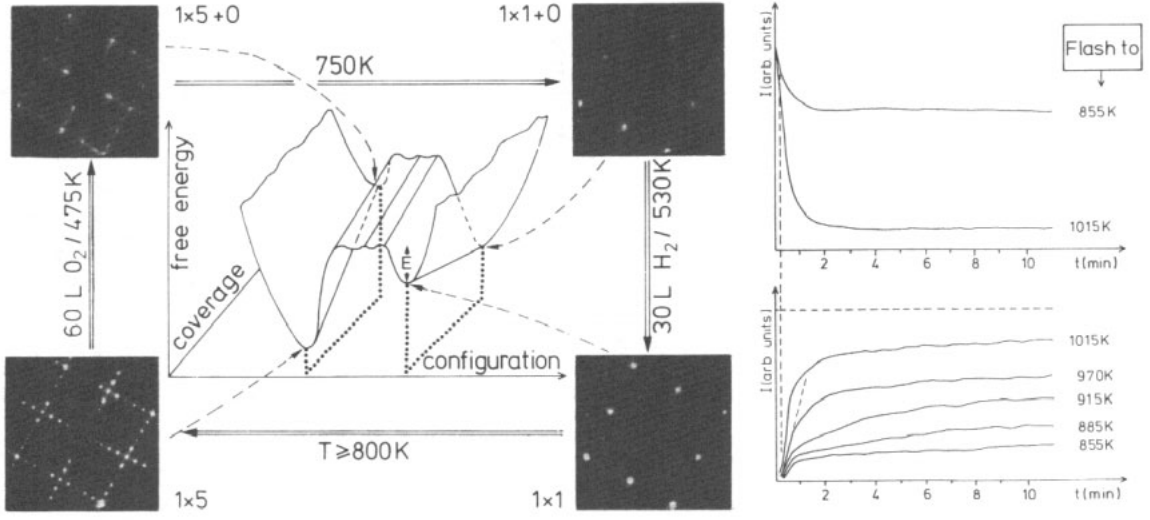

Figure 9. Reconstruction and deconstruction of Pt(100) under gas adsorption and thermal treatment (left) and kinetics of the phase transition $1\times1\rightarrow5\times1$ monitored by LEED intensities (right) (Heinz *et al* 1985).

order spot intensities as displayed in the right-hand panels of figure 9. The temperature-dependent slope of the intensity increase gives access to the activation energy of the transition.

As demonstrated, the modern methods of data acquisition allow for new types of measurements. However, in spite of the variety of possible measurements (spot profiles and integrated intensities; energy, temperature and time dependence), all the examples given above apply to the measurement of spots only, i.e. they are restricted to only a small area in reciprocal space. The new experimental techniques, however, allow fast access to the full reciprocal space. The next section will demonstrate that this opens the door to another new type of measurement and structural information.

4. Access to disordered adsorption structures: diffuse LEED

4.1. The LEED pattern in the case of disordered adsorption

Adsorption of atoms or molecules on surfaces is one of the most exciting fields of surface science because it corresponds to the first step of interaction of the solid with the outside world. The properties of important phenomena such as corrosion, epitaxial growth and catalysis as well as the properties of contacts and interfaces are closely related to adsorption. In the case of crystalline solids the surface offers regularly arranged adsorption sites, and so the surface scientist also expects the development of order in the adsorbate layer. In fact this frequently happens and due to reduced translational symmetry in this layer—if not all possible adsorption sites are occupied—superstructure spots are observed (figure 10, right). They can be measured and analysed in the usual way to yield the adsorption structure. It is because of numerous examples of successful structure determinations in this way (for overviews see Somorjai and Van Hove 1989, Watson *et al* 1994) that most people believe that LEED is restricted to ordered adsorption only.

However, adsorption does not always take place in an ordered way. In a microscopic picture, atoms or molecules arrive at the surface statistically. They must lose their translational kinetic energy and accommodate to thermodynamic equilibrium determined by the temperature of the surface. This may be done during the first contact with the surface atoms or by some subsequent hopping processes. By the latter or/and by surface diffusion at sufficiently high temperatures long range order can develop in the adlayer. It is controlled by the mutual interaction of the adsorbed species and their interaction with the substrate. However, when the surface mobility is too low, the species remain in their accidental initial adsorption site. In particular this happens at low adsorption temperatures. Then, because of lacking translational symmetry, no superstructure spots, but a diffuse intensity distribution is observed (figure 10, top left). It is determined by the superposition of the diffuse distributions generated by the different adsorption clusters, i.e. the adsorbed species and their atomic neighbours in the substrate. When there are many different adsorption sites, many different diffuse distributions overlap, which can lead to a rather unstructured distribution. However, even at low temperatures the adsorbing species usually manage to find the locally 'best' adsorption site, i.e. that of highest binding energy. This might be a hollow site to which it switches when having initially and accidentally adsorbed to, e.g., a bridge or top site. Then all adsorption clusters are structurally equivalent (*lattice gas disorder*) and each of them produces the same diffuse intensity distribution $I_0(E, k_{f\parallel})$ with E the electron

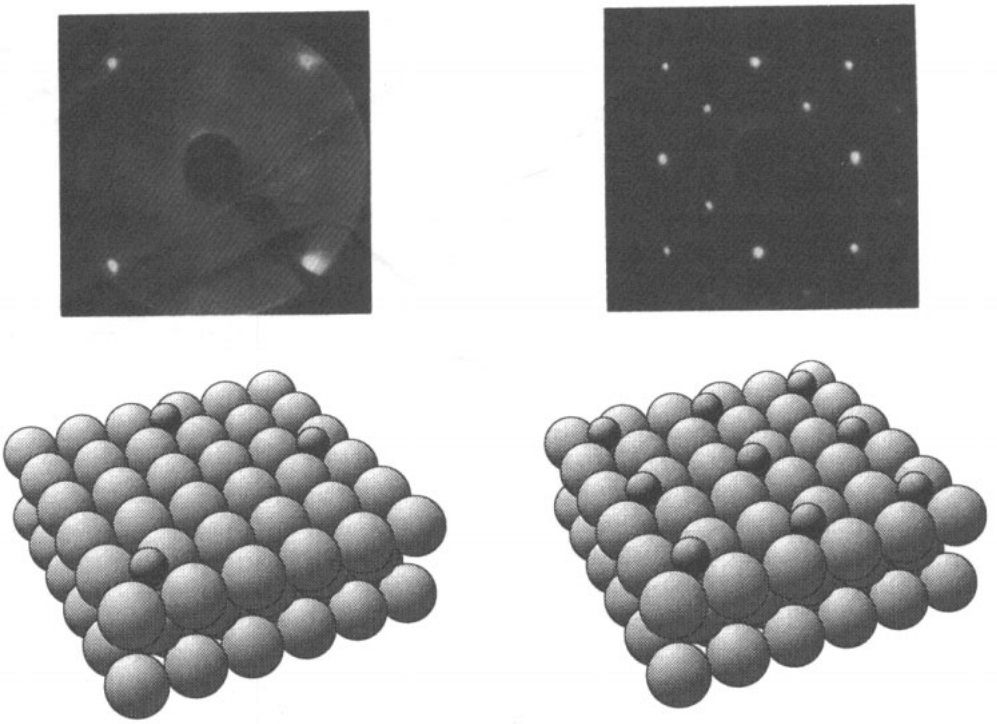

Figure 10. Ordered (right) and disordered (left) adsorption of oxygen on Ni(100) with real space models (bottom) and corresponding diffraction patterns (top).

energy and $\boldsymbol{k}_{f\parallel}$ the surface parallel component of the momentum into the final direction. This is for a fixed momentum of incidence $\boldsymbol{k}_{i\parallel}$ which is omitted in the notation. For low coverages there is almost no multiple scattering between the clusters, so the total intensity results by interference of the single cluster contributions described by the appropriate lattice factor, $I(E, \boldsymbol{k}_{f\parallel}) = I_0(E, \boldsymbol{k}_{f\parallel}) S(\boldsymbol{k}_{f\parallel})$.

When there is no correlation between the different adsorption clusters as it is likely to happen at low coverages, their interference is statistical, $S(\boldsymbol{k}_{f\parallel}) \approx \text{const}$, and the total diffuse distribution is identical to that of the single cluster, $I(E, \boldsymbol{k}_{f\parallel}) \propto I_0(E, \boldsymbol{k}_{f\parallel})$. This case seems to apply for the adsorption of oxygen on Ni(100) taking place at low temperatures (90 K). Figure 10 (left) displays a real space model and the corresponding diffuse LEED pattern superimposed on the sharp spots generated by the crystalline substrate (Starke *et al* 1989). Apparently, the diffuse intensity distribution is not isotropic, and it will be demonstrated below that from this anisotropy information about the local adsorption structure can be evaluated. This DLEED technique was first suggested on theoretical grounds by the London Imperial College group (Pendry and Saldin 1984) and was successfully applied to experimental data shortly after (Heinz *et al* 1985b).

Of course, one never can be fully sure whether the assumption $S(\boldsymbol{k}_{f\parallel}) \approx \text{const}$ holds or not. In particular for higher coverages it is most likely that correlations exist between different adsorption clusters. In this case one must get rid of the unknown factor $S(\boldsymbol{k}_{f\parallel})$. Fortunately, for a flat, i.e. unstepped, surface $S(\boldsymbol{k}_{f\parallel})$ is independent of the electron energy. So, by using the logarithmic derivative of $I(E, \boldsymbol{k}_{f\parallel})$ with respect to energy and

for $k_{f\parallel}$ fixed, $L=(\partial I/\partial E)/I$, the unknown lattice factor cancels (Pendry and Saldin 1984). Similar to the construction of the Pendry R-factor described in section 2.3 it is advisable to use $Y=L/[1+(LV_{0i})^2]$ instead of L in order to avoid artificial divergences. However, it should be emphasized that $S(k_{f\parallel})$ cancels only if all adsorption clusters are equivalent. In the case that adsorption takes place at different sites the situation is much more complex (Le Bossé *et al* 1990).

4.2. Measurement and evaluation of diffuse intensities

With the modern experimental techniques at hand it is easy to measure two-dimensional intensity distributions. This is because both the video and the channel plate methods are provided with spatial parallel detection. However, it is important to realize that even a clean surface exhibits some diffuse background which adds to that caused by disordered adsorbates. This is because no surface is structurally perfect. Various crystallographic defects such as, e.g., vacancies or steps as well as dynamic defects such as atomic thermal vibrations cause diffuse intensities on their own. Fortunately, these defect contributions are only weakly influenced by the adsorption of adatoms or molecules at least as long as the coverage is low. This was quantitatively shown for O/Ni(100) (Ibach and Lehwald 1986) and is likely to hold for other adsorption systems also. Therefore, the additional measurement of the clean surface signal with subsequent subtraction from the signal of the disordered adsorbate corrects for the contributions of surface defects. This corresponds to the measurement of the derivative of the intensities with respect to coverage, $\partial I/\partial\Theta$. For low coverages both signals are usually weak and so generally require a detector of high sensitivity. Whilst there is no problem in this respect with channel plates, the TV method requires the use of an intensifier camera. For both techniques multiple averaging of patterns is advisable in order to improve the signal-to-noise ratio. Moreover, for low coverages the signal of the adsorbate is of the same order of magnitude as that of the clean surface. So, both measurements have to be carried out with extreme care which should not overlook effects such as the change of the primary beam current with adsorption or a time-dependent dark current of the camera.

Figure 11(*a*) demonstrates the measurement procedure for O/Ni(100) for a certain energy (Starke *et al* 1989, Heinz 1990a). For a simple adsorbate system with only a few structural parameters to be determined, the intensity map taken for a single energy might carry sufficient information to yield the structure. Complex structures, however, require maps taken at several energies. Also, if correlations between adsorption clusters exist, the Y-function map rather than the intensity map has to be used as described above. In the latter case the measurement procedure at the energy chosen must be repeated at a near-neighbour energy. After subtraction of the two clean surface corrected maps the Y-function map can be constructed as demonstrated in figure 11(*b*). Evidently this more sophisticated procedure corresponds to the measurement of a second derivative of intensities, $\partial^2 I/(\partial E\,\partial\Theta)$.

As with conventional LEED, the structure only results by comparison of the measured intensities to model calculations. However, for disordered adsorption, one of the ingredients of dynamical LEED intensity calculations—the translational periodicity—is lacking. Therefore, a cluster type approach has been developed as schematically displayed in figure 12 (Pendry and Saldin 1984). First, the species adsorbed is hit both by the primary beam and the wave diffracted back from the substrate. In a second step there is multiple scattering between the adsorbate and the substrate. Finally, the adsorbate scatters to

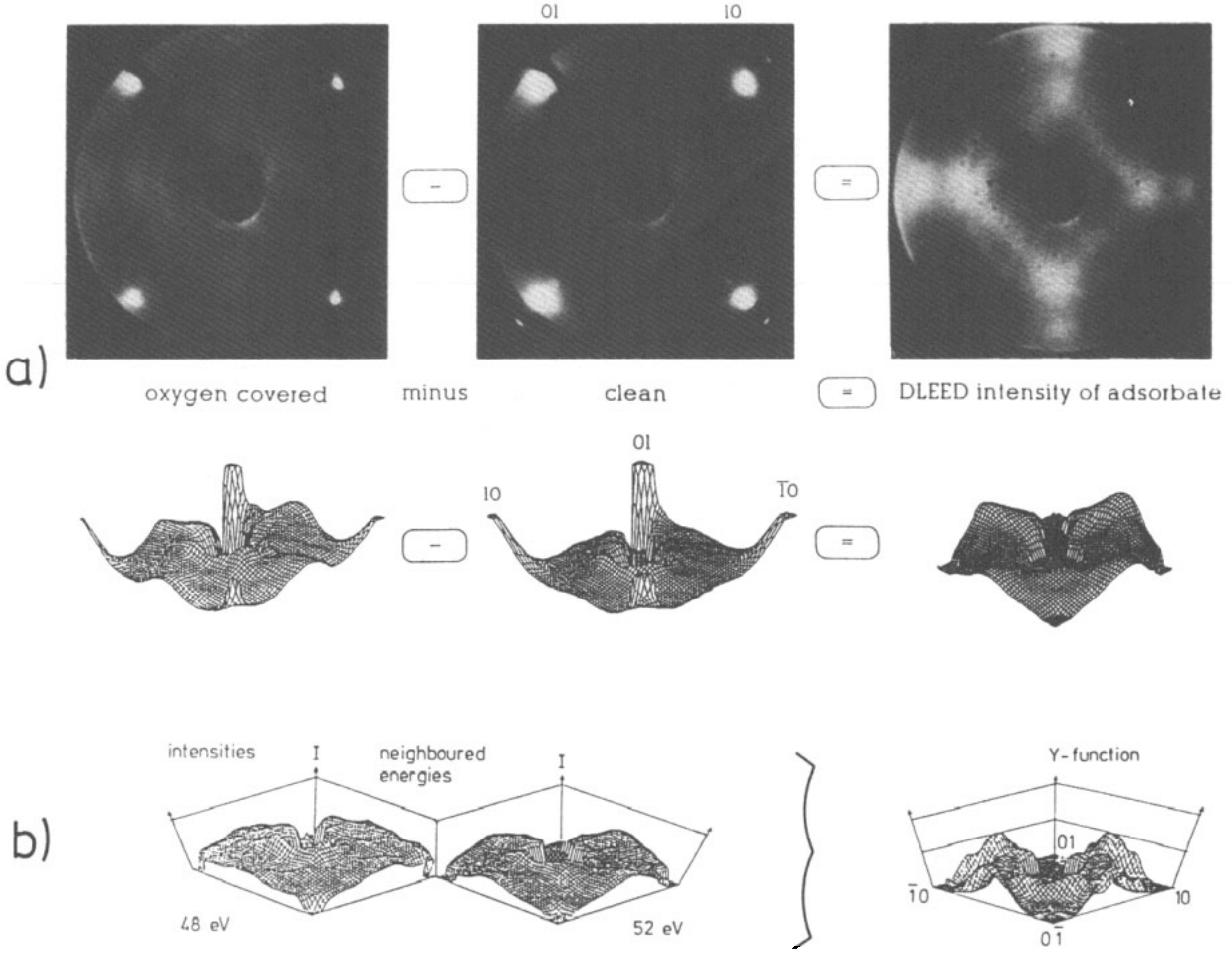

Figure 11. Diffuse intensity maps for disordered O/Ni(100) measured by the TV method. In (a) the patterns and three-dimensional intensity maps at 48 eV are given for the oxygen covered and clean surface, which produce the signal of the pure adsorbate. In (b) the difference of two maps neighbouring in energy (48 and 52 eV) produces the *Y*-function map (after Heinz 1990a).

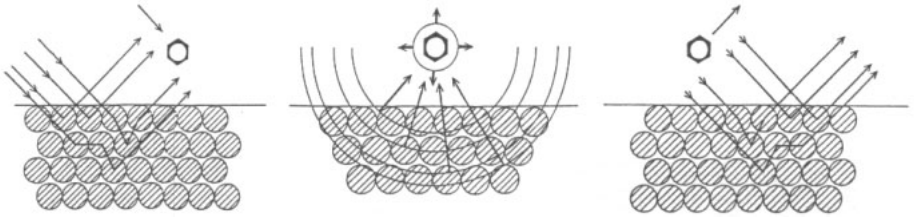

Figure 12. Three-step procedure of the cluster approach for the calculation of diffuse intensities generated by an adsorbed species (after Pendry and Saldin 1984).

the detector both directly and via the substrate. For a single adatom or small molecule adsorbed, the size of the cluster is determined by the electron attenuation length which is of order of only a few Å, i.e. the size of the unit mesh of an elemental substrate. Consequently, the intensities should exhibit only one or two maxima within the Brillouin zone, in agreement with experiment.

Though the cluster approach seems to be most appropriate for disordered adsorption, there is another way which even can use the conventional programs based on the presence of long range order. As the construction of the Y-function makes the interference of amplitudes between different clusters cancel one can arrange the adsorption cluster in any way as long as there is little or no multiple scattering between them, as is the case in the low coverage regime. If one arranges the adsorbates to form a large and primitive unit cell with translational symmetry, the corresponding conventional intensity calculations produces superstructure spots whose intensities sample the diffuse distribution caused by the single cluster. This large unit cell method which takes advantage of the fact that not all subsets of beams must be considered simultaneously (*beam set neglect method* (Van Hove *et al* 1983)) is equivalent to the cluster type calculation (Saldin *et al* 1985). The required sampling grid depends on the size of the adsorption cluster. For single atom adsorbates the variation of the diffuse intensities is quite slow as argued above. So, for an atomic adsorbate a superstructure unit mesh size of 4×4 (or larger) samples the diffuse distribution with sufficient density (Heinz *et al* 1992, Mendez *et al* 1993).

As an example of the successful determination of the local structure in the case of disordered adsorption, figure 13 displays the essential features of the disordered adsorption of oxygen on W(100) which was the first local structure solved by the DLEED technique (Heinz *et al* 1985b, Rous *et al* 1986). The W(100) surface exhibits a substantial reconstruction in $c(2 \times 2)$ symmetry when clean. This reconstruction is lifted when, e.g., oxygen is adsorbed by about 20% of a monolayer. Simultaneous with the disappearance of superstructure spots strong diffuse intensities appear as shown in the upper left of figure 13 together with the three-dimensional presentation for one quadrant in the middle. The relatively large coverage is likely to cause correlations between different adsorption clusters and so the Y-function has to be used for the retrieval of the local structure. It is displayed in the upper right panel of figure 13 again for one quadrant. Apparently it is rather unstructured. Below, the calculated best fit the Y-function is displayed which compares very well to the experiment corresponding to a Pendry R-factor $R = 0.05$. This is achieved by oxygen adsorbed in the hollow site and variation of both the adsorption height and a local reconstruction of the substrate according to the atomic model given in the lower left of figure 13. The R-factor map also displayed in the figure shows that oxygen is adsorbed at a height of 0.59 Å and induces a diagonal

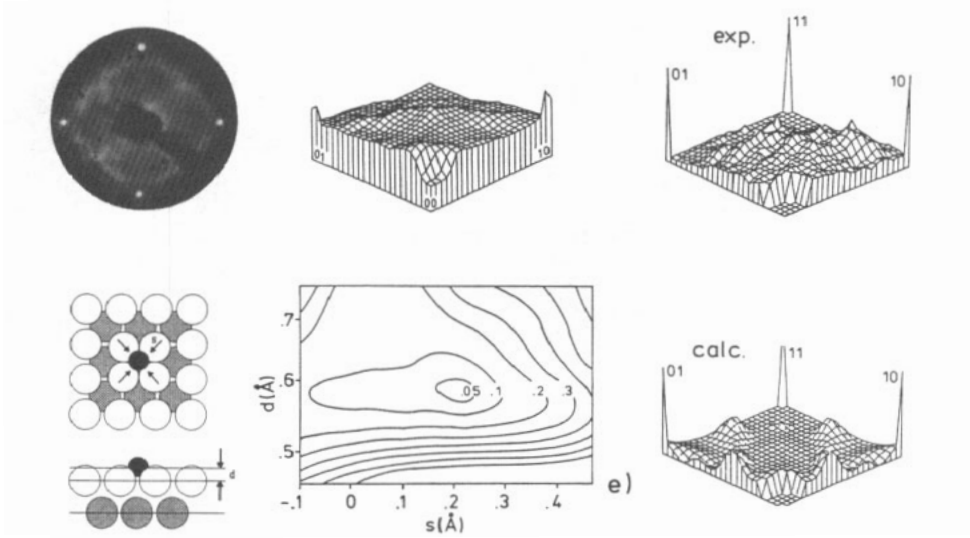

Figure 13. Retrieval of the local adsorption structure for disordered adsorption of oxygen on W(100). Top (from left): diffuse pattern at 41 eV, measured intensity distribution and *Y*-function for one quadrant. Bottom (from left): local adsorption model, *R*-factor map as a function of oxygen adsorption height and substrate atom displacements (in the x and y directions), best fit *Y*-function.

local reconstruction of tungsten atoms with an amplitude $0.15 \times \sqrt{2}$ Å $= 0.21$ Å. This demonstrates that the phenomenon of adsorbate induced reconstruction, which nowadays is viewed as more the rule than the exception, is caused by the local influence of the adsorbate, i.e. its binding to its local atomic surroundings.

A number of other disordered adsorption structures have been solved by the described mapping of two-dimensional DLEED intensities (for a review see Heinz 1990a). Both atomic and molecular adsorbate structure were determined, including substrate reconstructions for O/Ni(100) (Starke *et al* 1988), S/Ni(100) (Starke *et al* 1991), CO/Pt(111) (Blackman *et al* 1988), CO_2/Ni(110) (Illing *et al* 1988), CO/Ru(001) (Piercy *et al* 1989), C_6H_6/Pt(111) (Wander *et al* 1991) and Cl/Ti(0001) (Ri and Watson 1992). In spite of this successful work it must be admitted that DLEED in the version described puts substantial demands both on experiment and theory. As outlined above the experiment requires the measurement of two-dimensionally resolved diffraction patterns, i.e. images of low level data in second derivative. Their full dynamical interpretation both by the cluster and the large unit cell method is time consuming. This is the more true as single energy diffuse intensity maps in many cases are not sufficient to retrieve the local structure but data at several energies are needed. Fortunately, it could be shown that diffuse data can also be taken and analysed in the usual form of intensity against energy spectra. This comes from the intrinsic equivalence of LEED and DLEED which is illuminated next.

4.3. Equivalence of DLEED *and* LEED *as local probes of surface structure*

In figure 14 the diffraction from ordered and disordered adsorbates are contrasted for K/Ni(100) both schematically and by photographs of the diffraction patterns. The

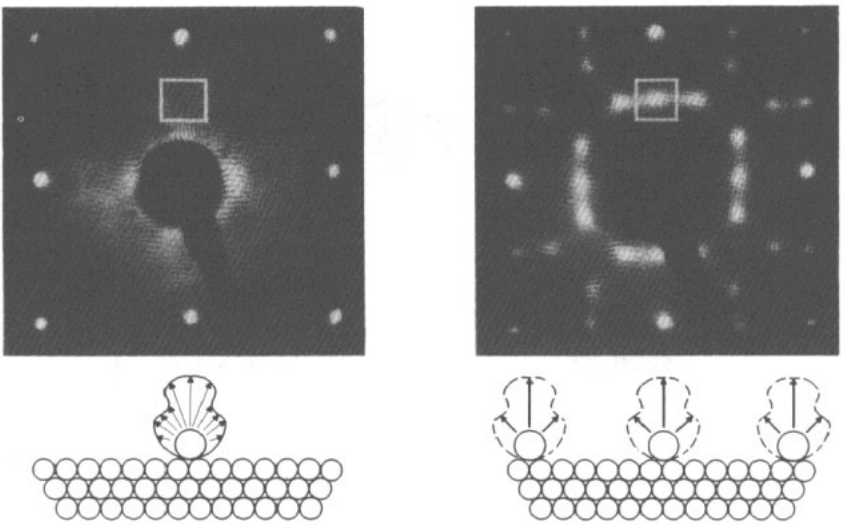

Figure 14. Diffraction from disordered (left) and ordered (right) adsorbates described schematically (bottom) and by the appearance of the diffraction patterns (top) for K/Ni(100). The disordered phase corresponds to coverage $\Theta = 0.04$, the ordered to $\Theta = 0.25$.

single adatom gives rise to a diffuse but anisotropic intensity distribution superimposed on the substrate beams. If order is made to develop at higher coverages and by careful annealing, there is interference between the different adsorption clusters and eventually intensities emerge only into directions allowed by the translational symmetry of the adlayer, i.e. into superstructure spots. As interference is just the linear superposition of amplitudes, the intensity of any superstructure spot is a constant multiple of the diffuse intensity measured for the same direction. This means that the superstructure spots of an ordered overlayer sample the diffuse distribution. This holds as long as multiple scattering between neighbouring adsorption clusters is negligible and the local adsorption structure is not modified by ordering (Mendez *et al* 1993). Of course, this is the philosophy of the large unit cell method. The expression $I(E, \boldsymbol{k}_{f\parallel}) = I_0(E, \boldsymbol{k}_{f\parallel}) S(\boldsymbol{k}_{f\parallel})$ given in section 4.1 fully describes this situation, where in the case of full order $S(\boldsymbol{k}_{f\parallel}) = N^2$ in the directions of superstructure spots and $S(\boldsymbol{k}_{f\parallel}) \approx 0$ otherwise (N = number of adatoms). In a more illustrative way one can say: dynamic electron diffraction intensities are formed locally, i.e. within a cluster limited by electron attenuation. When there is no systematic interference with other cluster contributions, diffuse intensities arise. In the case of long range order of the clusters, however, constructive and destructive interference makes intensities emerge in only discrete directions to form superstructure spots. In this sense DLEED and LEED are equivalent techniques which provide the local structure. Non-local features come only by the averaging over the area covered by the primary beam.

One can take advantage of this situation in a very efficient way. Instead of measuring diffuse intensity maps one can measure the diffuse signal at certain constant values of $\boldsymbol{k}_{f\parallel}$ as a function of energy, i.e. measure a 'diffuse spectrum' $DI(E)$ as if there were a discrete beam. This imaginary beam has to be tracked with sweeping energy as in the conventional measurement of a spot with $\boldsymbol{k}_{f\parallel} = \boldsymbol{k}_{i\parallel} + \boldsymbol{g}$. As for a flat surface $S(\boldsymbol{k}_{f\parallel}) =$ const for $\boldsymbol{k}_{f\parallel} =$ const the resulting $DI(E)$ spectrum is equivalent to a conventional $I(E)$

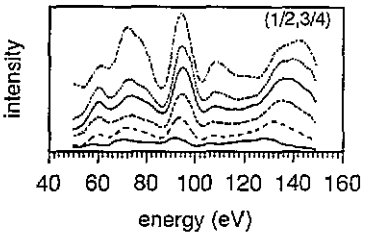

Figure 15. Comparison of $I(E)$ spectra for ordered c(4 × 2)K/Ni(100) (top curve, coverage $\Theta = 0.25$) and $DI(E)$ spectra for disordered or partially ordered K adsorption at $\Theta = 0.04$, 0.08, 0.14, 0.17 and 0.22 (from bottom) at the $\frac{1}{2}\frac{3}{4}$ position.

spectrum. This holds not only for complete order or disorder but for any degree of order. It has been observed and proved experimentally (Yang *et al* 1983, Heinz *et al* 1991a, Hu *et al* 1992) as well as by theoretical arguments (Pendry and Saldin 1984, Van Hove 1988).

If one arranges the positions of measurement $\{k_{f\parallel}\}$ so that a regular grid is formed, one can even evaluate the diffuse data in the conventional way, i.e. assuming translational symmetry present in the adsorbate. This brings both the DLEED measurement and its full dynamical intensity evaluation back to the procedures used in the conventional LEED analysis and has been used for the analysis of K/Ni(100) (Wedler *et al* 1993), K/Co(10$\bar{1}$0) (Hu *et al* 1992) and H_2O/Pt(111) (Starke *et al* 1992). As the degree of order is of no importance, the structure of adsorbates becomes accessible as function of coverage, as has been demonstrated for the adsorption of K on Ni(100) (Wedler *et al* 1993), for which depending on coverage, various degrees of order are observed. Figure 14 shows that at low coverages the intensity distribution is diffuse. With increasing coverage order gradually develops until at coverage 0.25 a c(4 × 2) superstructure is observed. As demonstrated in figure 15 for a certain value of $k_{f\parallel}$, the corresponding intensity spectra are almost constant in structure, reflecting that the local adsorption structure is almost independent of coverage. The small variations are due to small changes due to adatom–adatom interactions.

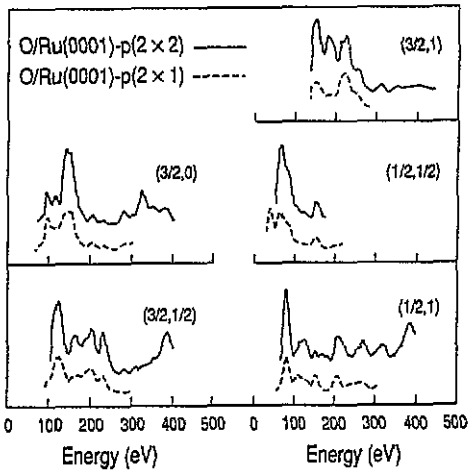

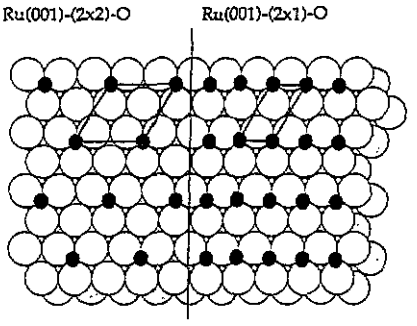

Figure 16. Models of phases (2 × 2)O/Ru(001) and (2 × 1)O/Ru(001) together with spectra of extra spots the two phases have in common (after Over *et al* 1994).

The local picture of diffraction also has consequences for the comparison of well ordered structures. If, for different phases of an adsorbate, the species adsorbed resides in the same local structure, the intensity spectra of spots emerging in the same direction for the different phases should be idéntical. Strictly speaking this holds only for non-overlapping adsorption clusters, but the spectra should be similar even in case of some overlap. This has been demonstrated, e.g., for different phases of Cs/Rh(100) (Heinz 1988). If the different phases have no superstructure spots in common, it is possible to interpolate spectra of neighbouring spots (Heinz *et al* 1992). Recently, these properties of spectra were proposed to be used as a fingerprint technique by which the adsorption geometry of a certain species can be identified by comparison with data of another phase of the same adsorbate (Over *et al* 1994). As an example, figure 16 displays spectra of various superstructure beams which two different phases of oxygen adsorbed on Ru(001) have in common. As apparent from the geometric models also given in the figure, there is certainly some overlap between neighboured adsorption clusters. Nevertheless the spectra compare very well.

5. Modern intensity calculations: tensor LEED

As described in section 2.3 the theory of dynamical low energy electron diffraction has been well developed since the 1970. It allows the reliable calculation of intensities for structures of—in principle—any complexity. However, though for clean and low index surfaces the calculation can even be performed on a minicomputer (Heinz *et al* 1985c), the necessary computer efforts grows considerably with increasing complexity. They scale, depending on the approximations used, with n^2–n^3 where n is the number of atoms in the unit cell. Though the calculations could be speeded up by the use of symmetry adapted functions in angular momentum expansion (Rundgren and Salwén 1975, Moritz and Wolf 1985, Tong *et al* 1988) this remained fatal for the retrieval of the correct values of the structural parameters when a scan of the parameter space is used to find the best theory–experiment fit in a trial-and-error procedure. This is because the number of trial structures grows exponentially with the dimensionality of the parameter space, i.e. the complexity of the structure.

Therefore, the strategy to solve complex structures by LEED must be twofold. On the one hand the computer efforts to calculate the intensities for a certain structure have to be reduced and, on the other hand, the scan of the parameter space has to be given up in favour of directed search procedures or direct methods. In fact, both strategies were followed during the last decade. In the present section we describe the substantial reduction of computer time for the intensity calculation made possible by the introduction of the perturbation method *tensor LEED*, whilst in section 6 we concentrate on the different methods followed to find the best fit structure in a more efficient way.

Of course, any reduction of computer time for the calculation of intensities of a trial structure must use certain approximations instead of applying the full dynamical theory (in the latter also approximations are used which, however, can be iterated to yield accuracy). Such approximations have been tried since the early days of LEED calculations, such as, e.g., the double diffraction approach (McRae 1968), the quasi-dynamical method which neglects intralayer scattering (Aberdam *et al* 1975, Tong *et al* 1977, Heinz and Besold 1983, Heinz *et al* 1985c), the beam-set-neglect approach which neglects coupling between certain sets of beams (Van Hove *et al* 1983) and other

partially kinematic type approximations (Meyer *et al* 1979, Jona *et al* 1985). All of them consider only a subset of the total of multiple scattering processes which is, of course, at the cost of accuracy. Nevertheless, these approximate schemes mentioned have proved to be useful in a number of cases. However, they were made largely superfluous with the development of the powerful tensor LEED method which is described in the following.

5.1. *Geometrical tensor LEED: displacements of atoms*

The basic idea of tensor LEED can be demonstrated by inspection of intensity data for structures which differ only by slight quantitative changes of the underlying structural parameters. As an example, the full curve spectra in figure 17 display intensities calculated fully dynamically for the 11 beam of a Ni(100) surface for different values of the first interlayer distance as indicated. It is obvious that there is no drastic change of the spectra when the structural change is small enough. So, one wonders if it is really necessary to apply a full dynamical calculation for each of the structures or if, instead, it is possible to produce the different spectra by perturbation of one of them calculated fully dynamically as a reference. In fact this is possible. The underlying theory *tensor LEED* was developed by the London Imperial College group and in the author's opinion marks the most important progress in LEED theory made during the last decade (Rous *et al* 1986, Rous and Pendry 1989a, b, Rous 1992). Its essentials are presented below.

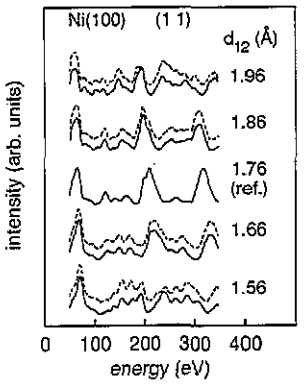

Figure 17. Spectra of the 11 beam of Ni(100) for different first interlayer spacings calculated full dynamically (full curves) and by tensor LEED (broken curves).

Assume that a full dynamical calculation has been carried out for a certain structure, i.e. a *reference structure*, and that the electron wave field $|\Psi(\boldsymbol{k}_\parallel)\rangle$ inside the surface has resulted according to an incident electron beam with surface parallel momentum $\boldsymbol{k}_\parallel$. Now some atoms at positions $\boldsymbol{r}_j$ with scattering t-matrix t_j are displaced by $\delta\boldsymbol{r}_j$ to form a certain trial structure. If the atomic scattering of the displaced atom is still to be described by a t-matrix t_j' located at its former position $\boldsymbol{r}_j$ one has to modify the old matrix according to

$$t_j' = t_j + \delta t_j(\delta \boldsymbol{r}_j). \tag{5.1}$$

Of course, the new matrix t_j' can no longer be diagonal because, as illustrated in figure 18, the displacement introduces a non-spherical distortion of the scattering potential.

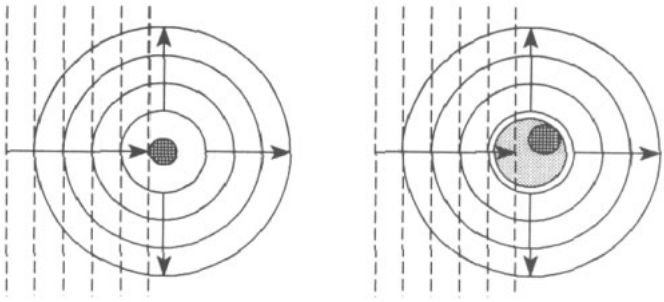

Figure 18. Scattering of a plane wave by an atom into a spherical wave centred at the atom's origin (left) and by a displaced atom (right) with the scattering expressed in terms of spherical waves centred at the original position (after Rous 1992).

In angular momentum basis using the abbreviation $L=(l, m)$ the change of the matrix can be calculated by

$$\delta t_{jLL'}=\sum_{L''} G_{LL''}(\delta \boldsymbol{r}_j)t_{L''}G_{L''L'}(-\delta \boldsymbol{r}_j)-t_{jl}\delta_{ll'} \tag{5.2}$$

whereby G represents the spherical wave propagator which converts a spherical wave centred at $\boldsymbol{r}_j$ to a set of spherical waves centred at $\boldsymbol{r}_j+\delta \boldsymbol{r}_j$. The atomic displacements cause a change of the diffraction amplitude which for the final direction with parallel momentum $\boldsymbol{k}_{f\parallel}$ can be calculated by first order perturbation

$$\delta A=\sum_j \langle \Psi(\boldsymbol{k}_{f\parallel})|\delta t_j|\Psi(\boldsymbol{k}_{\parallel})\rangle. \tag{5.3}$$

In angular representation this can be expressed by

$$\delta A=\sum_j \sum_{LL'} T_{jLL'}\delta t_{jLL'} \tag{5.4}$$

which eventually allows the calculation of the intensity of the new trial structure by

$$I=|A_0+\delta A|^2 \tag{5.5}$$

with $I_0=|A_0|^2$ the intensity of the reference structure (Rous and Pendry 1989a). The quantity T is a tensor in angular momentum representation and this explains the name *tensor* LEED or, more precisely, as geometrical displacements cause the t-matrix changes, *geometrical tensor* LEED. The tensor depends only on the reference structure and this mirrors the main advantage of the method: Once the tensor has been computed the intensity of any trial structure results very quickly using equations (5.2)–(5.5). This is similar to a kinematic description of diffraction: in equation (5.4) the tensor represents the form factor and the δt stand for the structure factor. In fact, scattering processes involving more than one δt, i.e. multiple scattering at changes of potentials, are neglected intensor LEED. In other words, the change of scattering due to the atomic displacements is calculated kinematically.

Of course, limitations of tensor LEED must exist with respect to the amount of $\delta \boldsymbol{r}_j$ by which atoms can be displaced. Unfortunately, because of the complexity of multiple scattering, no strict rules can be derived though tensor LEED is exact in the kinematic limit of diffraction. Experience tells that for displacements up to 0.2–0.5 Å tensor LEED works well, this limit and the accuracy reached depending largely on the extent of

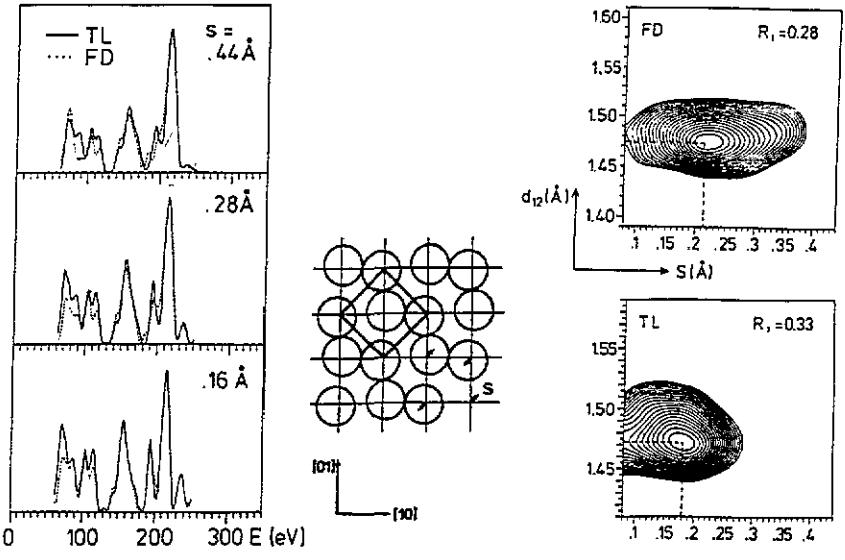

Figure 19. Left: comparison of $\frac{1}{2}\frac{1}{2}$ beam spectra of c(2×2)W(100) for different reconstruction amplitudes calculated full dynamically (full curves) and by tensor LEED (broken curves) using the unreconstructed surface ($s=0$) as a reference. Middle: model of the zigzag reconstruction (amplitude s) of W(100). Right: Pendry R-factor maps comparing experimental data of c(2×2)W(100) to full dynamical (top) and tensor LEED (bottom) calculations as a function of the top layer spacing d_{12} and the reconstruction amplitude s (after Bickel *et al* 1988).

multiple scattering correlations of displaced atoms. In turn this depends on the scattering strengths of the atoms, the number of atoms displaced, the direction of displacement and the electron energy. For the example of Ni(100) figure 17 demonstrates that tensor LEED reproduces the spectra for various values of surface relaxations, i.e. the movement of a complete layer, very well. However, this example does not fully reflect the real power of tensor LEED. This comes when the reference structure is of much less complexity than the trial structure. So, the reference can be a 1×1 structure and the superstructure develops only by atomic displacements. Then, though there are no extra beam intensities computed in the reference calculation, they easily result by the perturbation procedure. As an example, the left panel in figure 19 displays spectra of the $\frac{1}{2}\frac{1}{2}$ beam of c(2×2)W(100) for different zigzag displacement amplitudes of top layer atoms which are characteristic for the reconstruction of tungsten modelled in the middle panel (Bickel *et al* 1988). Though the unreconstructed surface has been used as a reference and though tungsten atoms are very strong scatterers, the tensor LEED data compare very well to the full dynamical calculation. Only for displacements of more than about 0.4 Å do untolerable deviations between exact and approximate data develop. Consequently, tensor LEED retrieve the correct structural data if the corresponding atomic displacements are not too large. This is demonstrated in the right-hand panels of figure 19 which compare R-factor maps for the full dynamical and the tensor LEED analysis.

The reader might have the impression that displacements of up to only a few tenths of an Ångstrøm are not very helpful to scan a substantial part of the parameter space. In fact it is true that a good initial guess, i.e. the reference structure chosen being near the true structure, is always of great advantage. However, one should also keep in mind that, within a certain model, there a serious restrictions put by chemical bonding.

Displacements of a few tenths of an Ångstrøm or more off the reference positions usually break bonds and so frequently lead to a qualitatively completely new model. So, in this respect displacements of a few tenths of an Ångstrøm are comparatively large. If the perturbation of a chosen reference fails to produce a satisfying fit to experiment one must try a new model and start a new reference calculation. This procedure is advisable anyway in order to avoid landing in a local minimum of the *R*-factor and is applied in demanding structure determinations, examples of which will be given in section 6.

If even smaller displacements are of interest, tensor LEED can be linearized with respect to the displacement (*linear tensor LEED*). In this case, i.e. for small enough δt_j, the first Born approximation $\delta t_j \approx \delta V_j$ can be used, where δV_j is the change of the scattering potential connected with the atomic displacement. Using the gradient of the potential, ∇V_j, this can be approximated by $\delta t_j \approx \delta V_j \approx \nabla V_j \cdot \delta r_j$. With equation (5.3) this leads to

$$\delta A \approx \sum_j \sum_i^3 T_{ij} \delta r_{ij} \tag{5.6}$$

with $T_{ij} = \langle \Psi(k_{f\parallel}) | \nabla_i V_j | \Psi(k_\parallel) \rangle$ and $i = 1, 2, 3$ denoting the coordinates x, y, z (Rous and Pendry 1989a, Rous 1992). Of course, with the tensor T_{ij} known from the reference calculation this is an even faster method to calculate δA. However, experience tells that it works only for displacements not larger than about 0.1 Å. Nevertheless, it is very useful for the direct structural refinement of a reference structure as will also be demonstrated in section 6. Moreover, linear tensor LEED can be applied to compute intensities of chemically disordered alloys or to simulate thermal vibrations of atoms, as will be shown in the remaining parts of the present section.

Once the reference structure calculation has been carried out, tensor LEED is extremely fast to compute the intensities for neighbouring structures. If there are n atoms per unit cell the CPU time to calculate any new structure simply scales with n, rather than with n^2-n^3 in the full dynamical procedure. If only a small number of structures has to be calculated the overhead burden to perform the reference calculation might favour the full dynamical calculation. However, as soon as a large number of trial structures has to be checked, as is usually the case, tensor LEED is—dependent on the complexity of the structure—faster by orders of magnitude (Rous and Pendry 1989b).

5.2. *Chemical tensor LEED: substitution of atoms*

Tensor LEED is designed to yield the change of the crystal's diffraction amplitude δA when one or several atoms change their scattering strength by δt_j. Obviously, δt_j may not necessarily be due to a displacement of atom j, although this was the original idea of tensor LEED. So, instead of moving an atom of type A we could simply substitute it by an atom of type B. This chemical substitution produces a change of scattering by

$$\delta t_j = \delta t_j^{\mathrm{B}} - \delta t_j^{\mathrm{A}} \tag{5.7}$$

and using equation (5.4) a diffraction amplitude change

$$\delta A = \sum_j T_j \delta t_j \tag{5.8}$$

results where the angular momentum indices were omitted in order to keep the notation

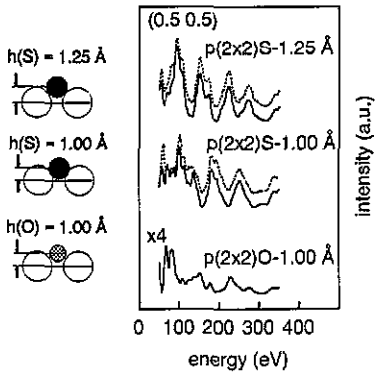

Figure 20. Left: adsorption models of c(2×2)O and c(2×2)S/Ni(100). Right: $\frac{1}{2}\frac{1}{2}$ beam spectrum of c(2×2)O/Ni(100) at 1.00 Å adsorption height serving as the reference (bottom), of c(2×2)S/Ni(100) at 1.00 Å (middle) and 1.25 Å adsorption height (top). Full and broken curves correspond to full dynamical and tensor LEED calculations, respectively (after Döll *et al* 1993, Döll 1994).

short. It is emphasized that in this *chemical tensor* LEED method (Döll *et al* 1993) the calculation of δt_j is even easier than by equation (5.2) because no propagators are involved. Also, the tensor T describes the electron wave field at the ideal, i.e. undisplaced, position of the atom and so one can expect a high degree of accuracy.

This accuracy is demonstrated in figure 20 where on the left the atomic models show (2×2) superstructures of two different adatoms, oxygen and sulphur, adsorbed in fourfold symmetric hollow sites on Ni(100) at different adsorption heights. The (2×2)O/Ni(100) phase is used as the reference with an (arbitrary) adsorption height of $h_O = 1$ Å. On the right, the bottom curve displays the spectrum of the $\frac{1}{2}\frac{1}{2}$ beam of this adsorption phase. Substitution of O by S using chemical tensor LEED produces the broken curve spectrum in the middle which is contrasted to the exact spectrum obtained by the conventional full dynamical calculation (full curve). The spectra compare very well, mirrored by an R-factor of $R_p = 0.07$, as averaged over all spots. This excellent agreement is in spite of the fact that by the substitution of oxygen by sulphur the spectra change dramatically due to the very different scattering behaviour of the two atoms (the average R-factor between extra spot spectra of the oxygen and sulphur adsorption phase is 0.78).

Of course, because of its size it is unlikely that sulphur resides at an adsorption site of 1 Å. In fact one knows from conventional analysis that the correct adsorption height is $h_S = 1.25$ Å (Oed *et al* 1990). The displacement of the adatoms to this position is an ideal task for geometrical tensor LEED and the result is shown in the top curve of figure 20 (broken curve) again contrasted to the exact data (full curve). There is almost ideal agreement ($R_p = 0.04$) although the perturbation is twofold, i.e. the adatoms are substituted *and* displaced (the fact that the R-factor is even better in the latter case compared to the R-factor for only the substitution is supposed to be accidental (Döll *et al* 1993)).

Though the above example demonstrates the power of chemical tensor LEED, it is certainly not the most practical case of application because normally the chemical species adsorbed is known and need not be substituted. However, the method can also be applied to create superstructures by substitution or even removal ($\delta t = -t$) of atoms

in a 1×1 structure, a procedure which saves much computer time (Döll *et al* 1993, Döll 1994). Yet, the largest field of application at present comes by the structure determination of surfaces of substitutionally disordered alloys. It was outlined in section 2.3 that the intensities of such surfaces can be calculated conventionally though in a strict sense the translational symmetry is broken. It is sufficient to use a (layer-dependent) average scattering matrix (*average t-matrix approximation* = ATA)

$$t_j = c_j t^A + (1 - c_j) t^B \tag{5.9}$$

and otherwise apply the computational schemes as usual. The index j denotes the number of the layer. If a reference calculation has been carried out for a certain geometrical structure and layer-dependent stoichiometry $\{c_j\}$, the intensities for a new stoichiometry $\{c_j + \delta c_j\}$ come easily by chemical tensor LEED, using

$$\delta t_j = \delta c_j t^A - \delta c_j t^B = \delta c_j (t^A - t^B) \tag{5.10}$$

together with equation (5.8). The power and validity of this approach is demonstrated in figure 21 for the (100) surface of the disordered alloy $Mo_{0.75}Re_{0.25}$ whereby spectra of a selected beam obtained by full ATA calculation (full curves) and by the chemical tensor LEED approach (broken curves) are compared. In the upper left panel the spectrum of the 10 beam of the bulk terminated sample with bulk stoichiometry in each layer is displayed which serves as the reference. In the following panels the concentration of Mo in the first two layers is decreased step by step as indicated, and the concentration of Re is increased accordingly. Though the spectra change drastically with varying stoichiometry chemical tensor LEED reproduces the correct data with high accuracy, as obvious from visual comparison and mirrored by the Pendry R-factors given in each case. This holds even for full depletion of Mo in the first two layers ($c_1 = c_2 = 0$) for which $R_p = 0.09$ results even though the spectra are very different from the reference data.

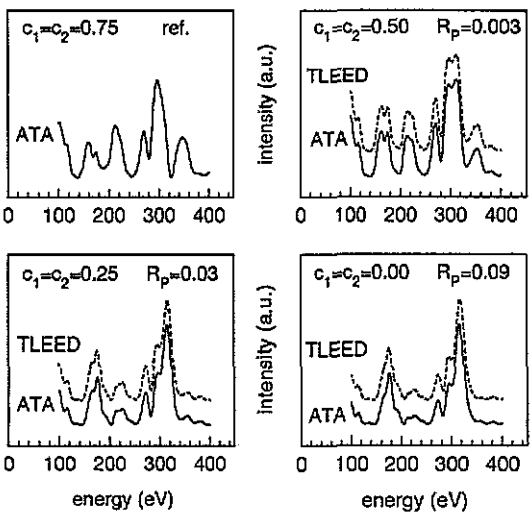

Figure 21. Spectra of the 10 beam of substitutionally disordered $Mo_{0.75}Re_{0.25}(100)$ calculated fully dynamically using ATA (full curves) and via chemical tensor LEED (broken curves) for various Mo concentrations $c_{1,2}$ in the first two layers. The bulk stoichiometry $c_1 = c_2 = 0.75$ serves as the tensor LEED reference Pendry R-factors are given for quantitative comparison.

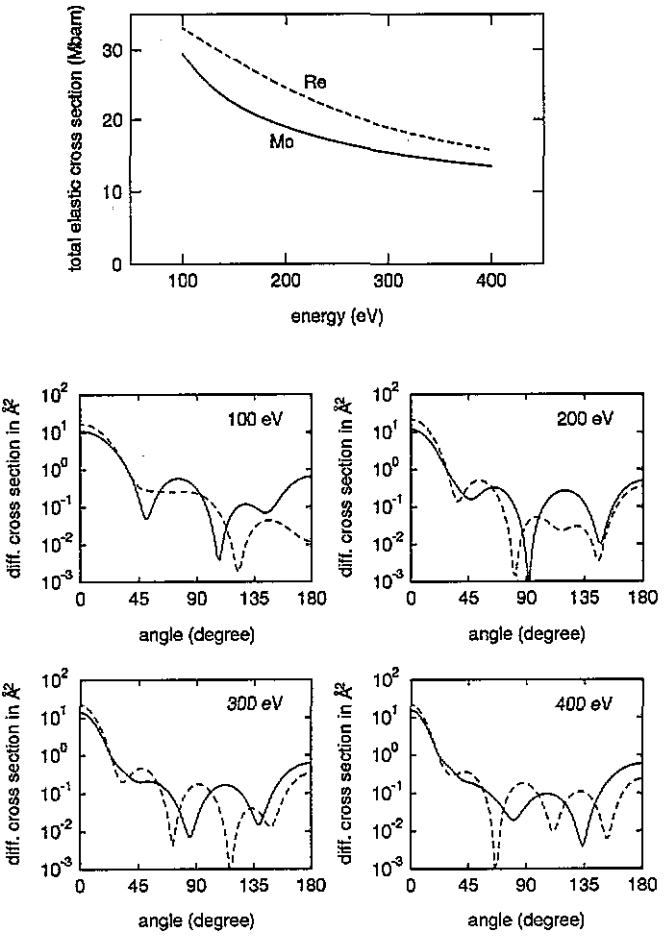

Figure 22. Total and differential elastic scattering cross sections for Mo (full curve) and Re (broken curve) as a function of energy and scattering angle, respectively.

The high sensitivity of the intensities with respect to stoichiometry must be due to different scattering properties of Mo and Re. As a demonstration, figure 22 displays both the total elastic scattering cross section of the two atoms as a function of energy, and the angular-dependent differential cross sections for some selected energies. Whilst the total cross sections are very similar in magnitude as well as in energy dependence, the angular dependence is very different (be aware of the linear and logarithmic scales in the two cases). This makes it obvious that it is the angular dependence which causes the observed sensitivity with respect to stoichiometry. As obvious from figure 20 chemical tensor LEED can easily be combined with geometrical tensor LEED, i.e. the deviation of both the location and chemical nature from a reference can be determined by tensor LEED in one run. Indeed, the application of tensor LEED to real experimental data yields best fit structures very close to those obtained conventionally (Döll *et al* 1994a). Large deviations from the bulk stoichiometry can be handled by chemical tensor LEED making repeated reference calculations superfluous in most cases. An example will be given in section 7. Of course, chemical tensor LEED can also be used to create partial substitutional order or disorder in a surface (Heinz *et al* 1995a).

5.3. Thermal tensor LEED: isotropic and anisotropic vibrations

In the above two subsections tensor LEED has been presented as a tool to describe the change of diffraction caused by atomic displacements $\delta \boldsymbol{R}$ or atomic substitutions A→B which enter the formalism by the corresponding change of the atomic t-matrix. Of course any change of the atomic scattering can be considered in this way and so also the modifications introduced by thermal atomic vibrations. A change of temperature δT will cause a change $\delta t = \delta t(\delta T)$ which enters the tensor LEED formalism as usual. If the reference is $T=0$, i.e. $\delta T = T$, the temperature comes in directly by $\delta t = \delta t(T)$. An early approach to consider thermal vibrations used linear tensor LEED (de Andres *et al* 1988), but as inherent to this linearized version of tensor LEED this applies only to small vibrational amplitudes below 0.1 Å.

As described in section 2.3 standard dynamical LEED calculations consider thermal vibrations by the use of complex phaseshifts whereby isotropic, harmonic and uncorrelated atomic movements are assumed. Normally, this approach is sufficient in the sense that it allows one to determine the correct structure, i.e. deviations from these assumptions are believed to have only negligible influence on the best fit structural parameters and only lead to an increased level of the R-factor. Therefore, efforts to consider, e.g., non isotropic vibrations have been underway only recently. One strategy uses conventional LEED programs (Over *et al* 1993) and will be reviewed in section 7.3. The other uses the tensor LEED approach (Pendry and Heinz 1990, Löffler *et al* 1995) and will be described in the present section. Before that, however, it should be mentioned that the conventional consideration of isotropic vibrations can also be the cause of substantial numerical effort. This is because the vibrational amplitude is only known for bulk atoms as, e.g., described by the bulk Debye temperature Θ_b. Amplitudes of near surface atoms can deviate substantially from that, and normally little is known of those for adsorbed species if no highly resolved energy loss spectra are available. Therefore, these amplitudes have to be fitted using different sets of complex phaseshifts. However, as phaseshifts are the initial input to LEED calculations, this means that for each set the whole intensity computation has to be repeated. This explains why normally only top layer vibrations are fitted. Even that, in many cases, is only done for the best fit structure and, of course, this is an unsatisfying approach. Fortunately, tensor LEED allows the efficient and easy fit of thermal vibrations during the process of the structure determination, whereby the vibrational amplitude or equivalently the corresponding Debye temperature is treated as an independent model parameter. In the following this feature is presented first and the treatment of anisotropic vibrations is addressed subsequently.

With $t(T, \Theta)$ and $t(0)$ the atomic scattering matrices for temperature T at Debye temperature Θ and zero temperature, respectively, the matrix change

$$\delta t(T, \Theta) = t(T, \Theta) - t(0) \tag{5.11}$$

results easily, whereby for isotropic vibrations expressions for $t(T, \Theta)$ in angular momentum representation can be taken from the standard literature (e.g., Pendry 1974). The quantity $t(0)$ can be made to consider the zero point vibrations with mean square amplitude $\langle u^2 \rangle_0 = 9\hbar^2/4mk_B\Theta$ where $\hbar$ and k_B are the Planck and Boltzmann constants, respectively, and m is the atomic mass. With the thermally activated vibrations $\langle u^2 \rangle_T = 9\hbar^2 T/mk_B\Theta^2$ the total mean square amplitude is $\langle u^2 \rangle = [(\langle u^2 \rangle_0)^2 + (\langle u^2 \rangle_T)^2]^{1/2}$. The validity of the method was demonstrated recently (Löffler *et al* 1994) and is similar to that of chemical tensor LEED due to the close relation of the two methods. Vibrations

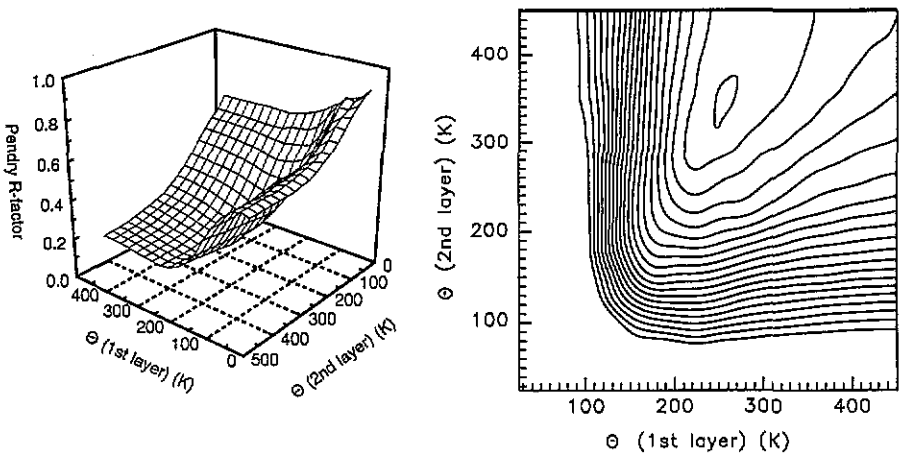

Figure 23. Pendry R-factor surface (left) and contour map (right) for Ni(100) as a function of the Debye temperatures of the first two nickel layers. The inner contour line corresponds to $R=0.18$, the following lines are incremented by $\Delta R=0.02$.

according to changes of temperature and/or Debye temperature of several hundreds of degrees can be considered with ease and high reliability. An example for the power of the method is given in figure 23 where the R-factor surface and contour map for Ni(100) is displayed as a function of the independently varied Debye temperatures of the first two layers (Löffler *et al* 1994). They are allowed to deviate from the bulk value ($\Theta_b=440$ K) which in an earlier investigation (Oed *et al* 1989) was assumed to hold for all layers. This yielded a first interlayer contraction $\Delta d_{12}/d_0=-1\%$ as the best fit to experimental data taken at 100 K according to an R-factor of $R_p=0.22$. Including zero point vibrations the new best fit develops for Debye temperatures $\Theta_1=250$ K and $\Theta_2=350$ K for the first and second layer, respectively, where the theory–experiment comparison improves significantly to a level given by $R=0.18$. This nicely demonstrates that the Debye temperature at the surface is reduced compared to the bulk and only layer by layer approaches the bulk value. It is also consistent with results obtained by ion scattering (Frenken *et al* 1983) and an effective value $\Theta_{eff}=335$ K obtained by a fit assuming the same Debye temperature for all atoms in the surface (Demuth *et al* 1975). Of course it should be checked if the interlayer contraction changes for the new best fit. Again this can be done by tensor LEED as geometrical displacements and thermal vibrations can easily be combined (Löffler *et al* 1994) using $\delta t(T,\delta r)=\delta t(\delta r)+G(-\delta r)\delta t(T)G(+\delta r)$. However, the independent variation of d_{12}, Θ_1 and Θ_2 yields no further change of $d_{12}/d_0=-1\%$, $\Theta_1=350$ K and $\Theta_2=250$ K.

Besides the effective treatment of isotropic oscillations tensor LEED is also capable of handling anisotropic thermal vibrations. Though the importance of the latter for top layer atoms, in particular for adsorbed species, was recognized early, until recently no efficient scheme has been developed for their proper consideration. The reason for this is because of the fact that standard LEED programs are based on spherically symmetric scatterers, i.e. the atomic scattering matrix is diagonal in the angular momentum representation. Efforts to develop LEED codes for non-spherical scatterers have been made earlier (Nagano and Tong 1985) but as the programs were rather complex there was no broad scale application. Fortunately, it turns out that tensor LEED is ideal to describe anisotropic scattering because δt needs not to be diagonal as it was, e.g., in the above

approach to describe isotropic vibrations. This is clear from the fact that $\delta t(\delta r)$ in geometrical tensor LEED is already non-diagonal in the angular representation because the displaced atom is no longer a spherical scatterer with respect to its original position. So, if $\delta t(T)$ can be calculated properly to describe anisotropic vibrations it only has to enter the tensor LEED formalism in the usual way with no further efforts needed.

This procedure has been realized only very recently (Löffler *et al* 1995) following ideas to use a cumulant expansion for the atomic scattering matrix (Fritzsche 1994). Starting with equation (5.2), which for a vibrational displacement $\boldsymbol{u}$ and omitting the indices may be written shortly as $\delta t = G(-\boldsymbol{u})tG(\boldsymbol{u}) - t$, the free propagator $G(\boldsymbol{u})$ is written in exponential form

$$G(\boldsymbol{u}) = \exp\left(\mathrm{i}k \sum_{\alpha} u_\alpha M^\alpha\right) \tag{5.12}$$

whereby α denotes the cartesian coordinates x, y, z and the M^α are a set of proper matrices describing the displacement. This can be used to produce the exponential series (Fritzsche 1994, Oed *et al* 1992, Löffler *et al* 1995)

$$\delta t = -\mathrm{i}k \sum_{\alpha} u_\alpha [M^\alpha, t] - \tfrac{1}{2}(-\mathrm{i}k)^2 \sum_{\alpha,\beta} u_\alpha u_\beta [M^\alpha, [M^\beta, t]] + \ldots \tag{5.13}$$

which can be rewritten in short form as

$$\delta t = \exp\left(-\mathrm{i}k \sum_{\alpha} u_\alpha [M^\alpha, \bullet]\right) t - t. \tag{5.14}$$

If now $\boldsymbol{u}$ is interpreted as the time-dependent amplitude of a harmonic vibration with average $\langle \boldsymbol{u} \rangle = 0$, the averaging procedure for δt leads to

$$\langle \delta t \rangle = \exp\left(-\tfrac{1}{2}k^2 \sum_{\alpha} \langle u_\alpha^2 \rangle [M^\alpha, \bullet]\right) t - t \tag{5.15}$$

where it has been assumed that the x, y, z coordinate system is chosen so that $\langle u_\alpha u_\beta \rangle = 0$ for $\alpha \neq \beta$. For small enough $\langle u_\alpha^2 \rangle$ this leads to an expression $\langle \delta t \rangle = \Sigma_\alpha \beta_\alpha \langle u_\alpha^2 \rangle$ as derived with linear tensor LEED (De Andres *et al* 1988). For isotropic vibrations

Table 1. Analysis of the adsorption phase c(4 × 2)K/Ni(100) at 175 K according to the model displayed in figure 24. The values in the left-hand column result from the assumption of a fixed and isotropic thermal vibration amplitude of adatoms. The parameters in the centre column result from the additional fit of isotropic vibrations and the right-hand column values from the fit of anisotropic vibrations allowing for different amplitudes perpendicular and parallel to the surface.

	Isotropic vibrations fixed ($u = 0.095$ Å)	Isotropic vibration varied	Anisotroic vibrations varied
d_{01} (Å)	2.68	2.70	2.74
d_{12} (Å)	1.76	1.76	1.76
d_{23} (Å)	1.76	1.76	1.75
Bu (Å)	—	−0.015	0.045
u (Å)	(0.095)	0.15	—
$u_\perp$ (Å)	—	—	0.05
$u_\parallel$ (Å)	—	—	0.50
R	0.37	0.30	0.21

($\langle u_x^2 \rangle = \langle u_y^2 \rangle = < u_z^2 \rangle$) the matrix δt is diagonal but becomes non-diagonal for anisotropic vibrations. Note that $\langle \delta t \rangle$ can be calculated for each atom separately, so in principle correlated vibrations of different atoms could also be handled. Also, non-harmonic vibrations can be treated with, however, expressions for $\langle \delta t \rangle$ more complex than that given above (Fritzsche *et al* 1994).

The above scheme was applied to the adsorption system c(4 × 2)K/Ni(100) for which a conventional analysis found potassium adsorbed in hollow sites (Muschiol *et al* 1992). The structural parameters determined by assumption of fixed isotropic potassium vibrations are given in the left-hand column of table 1. If isotropic vibrations are still assumed but used as a free parameter, the values in the centre column result with only small changes of the structural parameters but a decrease of the Pendry R-factor from 0.37 to 0.30. However, this reduction is also due to a small adsorbate-induced substrate reconstruction, i.e. some buckling allowed for the nickel atom below the adatom in the second substrate layer according to figure 24. The third column displays the results for anisotropic vibrations. There is another substantial reduction of the R-factor to $R_p = 0.21$. It turns out that the vibrational amplitude parallel to the surface is ten times as large as vertical to it, i.e. the assumption of isotropic vibrations does not hold at all. This is certainly due to the potassium diameter being much larger than that of nickel, so that the adatoms feel the substrate's corrugation only slightly. Moreover, it turns out that consideration of the correct surface vibrations can also modify structural parameters such as the adsorption height and the buckling amplitude in the present case. However, on an absolute scale this is below a half of a tenth of an Ångstrøm.

The capability of tensor LEED to describe non-spherical scattering certainly has a larger field of applications than anisotropic vibrations. Top layer atoms and in particular adsorbed atoms or atoms in adsorbed molecules are unlikely to be ideal spherical scatterers. Tensor LEED could easily handle the non-spherically symmetric parts and so further improve the quality of the theory–experiment fit.

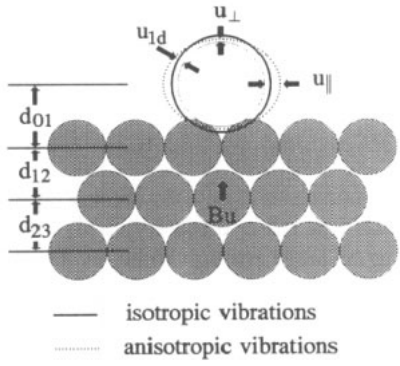

Figure 24. Structural and vibrational parameters for c(4 × 2)K/Ni(100) (Löffler *et al* 1995).

6. Structural search: linear LEED, automated search and direct methods

After the measurement the calculation of intensity spectra for a certain model is only the second step of the structural analysis. A task of substantial difficulty is still left, namely to find the correct model. This always starts with thinking about a reasonable

model on the basis of some pre-knowledge about the surface under consideration. So, one generally knows the crystallographic face and the elemental composition of the substrate. In most cases the latter is also known for the adsorbate or it can be deduced from independent Auger measurements and/or from thermal desorption spectroscopy. Vibrational loss spectroscopy can be used to provide information about the orientation and bonding of molecules, and images obtained by the tunnelling microscope may even suggest a single atomic model or rule out models which would be possible in principle. Last, but not least, experience from the structural solution of related surface systems can be of great help, too.

Once a reasonable and promising model is established, the parameters of this model need to be adjusted. There are several ways for this procedure which are described in the following. Except for one they are all based on a trial-and-error procedure, whereby the scan of the parameter space is the most basic procedure. As described in section 6.1 an approximative method (*linear* LEED (Wander *et al* 1992)) has been developed to allow a coarse scan of a large area of the parameter space in order to look for promising areas. However, when a large number of parameters on a dense grid has to be scanned, the necessary computational efforts grow dramatically and the scan must be replaced by some automated search to find the best fit structure (section 6.2). However, though by the use of R-factors as quantitative measures for the theory–experiment fit one always retrieves a best fit model, this need not to be the correct structure. If the quality of the fit is unsatisfying, additional parameters have to be investigated or a completely new model has to be tried. The judgment whether a fit, i.e. the lowest R-factor, is unsatisfying or not depends on the complexity of the structure under investigation and, of course, on the critical view of the investigator. For systems of medium complexity, i.e. with say no more than ten parameters, a model yielding a Pendry R-factor below 0.3 is frequently considered reliable. However, it is important to check also by visual comparison of experimental and calculated data.

In some favourable cases it is possible to circumvent the trial-and-error procedure: If there is a good guess of the correct structure due to some pre-information, it is possible to do the structural refinement in one step, equivalent to a direct method. This procedure is based on the inversion of linear tensor LEED, and is described in section 6.3.

6.1. Scan of the parameter space: practical limitations and linear LEED

Conventionally the adjustment of model parameters is done by a scan of the parameter space, and in fact the lion's share of existing LEED intensity analyses were performed in this way. The span of the space has to be large enough to cover all values reasonable by chemical and other considerations. Also, the density of the grid on which the scan is carried out has to be carefully selected. At each grid point a separate intensity calculation is carried out and the resulting spectra are compared to experiment. The quantitative measure provided by R-factors identifies the best fit model by the lowest R-factor value, i.e. the minimum of the R-factor hypersurface. If the level of agreement is convincing and the selected span of the parameter space was big enough one believes that the correct model has been found. At least within the parameter space scanned one is sure that one has not landed in a local minimum of the R-factor, a risk which automated search procedures run. Nevertheless, even in the grid search it might happen that different R-factor minima of very close depths are detected prohibiting a clear decision for the correct model. This is a hint that the model chosen is incomplete or even wrong.

Whilst the scan of the parameter space is straightforward, it suffers from severe limitations concerning the complexity of structures. So, if N is the number of atomic coordinates to be determined with M trial values for each, the number of different combinations is M^N. For five atoms in the unit cell ($N=15$) and $M=5$ this amounts to $\approx 3 \times 10^{10}$ structures to be tried. The situation becomes even worse if in addition non-structural parameters such as, e.g., thermal vibration amplitudes or the optical potential have to be adjusted. It is obvious that this exponential growth of the number of test structures with increasing number of parameters inhibits the application of the grid search method to complex structures. Even if the computation of intensities for a single grid point would need only 1 ms the scan of the parameter space would need a full year computer time. Evidently, there is need to find the best fit parameters by a more elegant and less time consuming procedure and this is the background of the automated methods which will be described in the next section.

Before that, however, it is fair to mention that in practice the grid search is not as unfavourable as described above. This is because there are often subgroups of parameters which influence intensity spectra (and so the R-factor) more than others. So, *intensities are more sensitive to parameters perpendicular to the surface compared to* those parallel to it. This is because the electron momentum transfer is predominantly normal to the surface. Also, electron attenuation provides more sensitivity to coordinates of near surface atoms compared to atoms in deeper layers. Generally, non-structural parameters are also less important, at least when varied in a reasonable range. These features allow a scan of the full parameter space to be avoided in favour of consecutive scans of subspaces, a procedure which normally needs to be iterated. So, one can first scan the subspace of vertical parameters, e.g., the first four interlayer distances which with $M=5$ trial values for each yields a total of $M^4=625$ grid points which can be easily scanned using intermediate storage of layer diffraction matrices. With perpendicular parameters now fixed the subspace of surface parallel parameters or other less influential parameters can be checked. Only a few iterations of this procedure usually leads to convergence and a number of rather complex structures were solved in this way (section 7 presents examples). In fact, automated search methods also frequently take advantage of the different sensitivity of intensities with respect to different groups of parameters. However, one must admit that the procedure described is not always possible and its applicability and reliability largely depends on the experience of the investigator.

Of course, a fast method for the intensity calculation is favourable both for the grid and the automated search. So, it is not surprising that tensor LEED today plays an important role in the structural search. However, care has to be taken that the range of validity is not exceeded while moving in the parameter space. Otherwise a new reference calculation is needed. In order to avoid that, a strategy for a fast and coarse search in order to look for promising models in a large area of the parameter space would be very helpful. With such a promising location found one could apply a fine grid to the surrounding subspace, or apply an automated search or even a direct method.

With the idea of *linear* LEED (Wander *et al* 1992) such a method has recently promised to be at hand. Imagine that in a simple case two atoms labelled 1 and 2 of a surface are displaced from position r_1 to $(r_1+\delta r_1)$ and from r_2 to $(r_2+\delta r_2)$, respectively. Then the corresponding change of the diffraction amplitude $\delta A = A(r_1+\delta r_1, r_2+\delta r_2) - A(r_1, r_2)$ is approximated by a *linear* combination of the amplitude changes which result by the displacement of each atom separately, i.e. by

$$\delta A \approx [A(r_1+\delta r_1, r_2) - A(r_1, r_2)] + [A(r_1, r_2+\delta r_2) - A(r_1, r_2)] \qquad (6.1)$$

where all amplitudes are calculated fully dynamically. So, with M trial values for each of the three coordinates of an atom there are M^3 trial positions. For n atoms in the unit cell nM^3 full dynamical intensity calculations have to be performed rather than a total of M^N with $N=3n$ necessary for the intensity calculation at each grid point. For $n=M=5$ ($N=15$) this reduces the number of full dynamical calculations from $M^N \approx 3\times 10^{10}$ to $nM^3=625$, a reduction which becomes even more dramatic for lager values of M and n.

The linear LEED approach is exact in the kinematic limit and, by design and different to tensor LEED, exact if only a single atom is displaced. Again different to tensor LEED it allows—at leat in principle—displacements of arbitrary size as long as the multiple scattering between the atoms does not change significantly by the displacement. As desired, this allows the scan of a large parameter space by large steps. A drawback with respect to tensor LEED is that superpositions of amplitude changes caused by different displacements of the same atom are not allowed, and that all single atom amplitude changes have to be calculated fully dynamically. Up to now linear LEED has been proved to work correctly only in one single application (Wander *et al* 1992). However, its potential with respect to a quick test scan of the parameter space is promising.

6.2. Automated structural search

As described above, the 'manual search' for the correct structure by scanning the parameter space is very cumbersome and except for special cases becomes impracticable when many structural parameters have to be determined. Then an automated search is needed, i.e. a numerical procedure which by built-in criteria finds the minimum of the R-factor automatically by a directed search. A number of such procedures were developed in recent years differing in requirements, strategies and efficiency, where experience from x-ray crystallography was very helpful (for a recent review see Van Hove *et al* 1993a). Requirements can differ by the need to use derivatives of the R-factor (and so of the intensities) with respect to parameters rather than only the intensities themselves. Derivatives in most cases are calculated numerically and so suffer from experimental noise and approximations used for the calculation of intensities (Rous 1992). Strategies differ by the numerical method to find the R-factor minimum and by the type of R-factor used. Some methods combine different procedures which work most efficiently far from or near the minimum.

The use of automated search procedures was frequently proposed (e.g., Adams 1985, Van Hove *et al* 1986) but first realized by the York group applying a form of steepest descent (Cowell and de Carvalho 1987). Starting with a certain reference structure the behaviour of the R-factor in the surrounding part of the parameter space is explored to find the direction in which the R-factor decreases most and this procedure is iterated. Soon after, and in parallel, different other groups developed procedures of their own. The Munich and Berlin groups (Kleinle *et al* 1989, 1990) use a non-linear least-squares fit procedure whereby the expansion method is combined with the method of steepest descent (Marquardt 1963). The linear expansion

$$I_{\mathrm{cal}}(\boldsymbol{p}) = I_{\mathrm{cal}}(\boldsymbol{p}_0+\Delta\boldsymbol{p}) = I_{\mathrm{cal}}(\boldsymbol{p}_0) + \sum_j^k \Delta p_j\, \partial I_{\mathrm{cal}}(\boldsymbol{p}_0)/\partial p_j \tag{6.2}$$

of calculated intensities in terms of the structural parameters $\boldsymbol{p}=(p_1,\ldots,p_k)$ is used to minimize the R-factor $R=\Sigma_i (I_{\mathrm{cal}}-cI_{\mathrm{exp}})^2$ which is similar to the R_2-factor defined

in section 2.3. This leads to a set of linear equations whereby linear approximations can be used to calculate the derivatives with high efficiency (Over *et al* 1992a). The system of equations can be solved by matrix inversion (expansion method), which works best near the minimum, or by the method of deepest descent to be preferred far from the minimum, so that a combination of both is optimal. Due to the non-linearity of the intensity function the procedure has to be iterated whereby the parameter controlling the mentioned combination is dynamically controlled. The method is reported to be very efficient, some additional advantage coming by the use of a modified *R*-factor which is taken at a wide spaced energy grid (typically 15 eV) as allowed by the redundancy of close spaced data. The intensities of only $(N+1)\nu$ models have to be calculated (N the number of parameters as above, ν the number of iterations) which is optimal in contrast to the scaling M^N applying for the grid search (M the number of trial values per parameter). For the system (2×1)O/Ni(110) with $N=6$ parameters a number of $\nu=8$ iterations proved to be sufficient (Kleinle *et al* 1990). This is equivalent to only 56 model calculations compared to a total of 15 625 models to be checked in a grid search with $M=5$. Examples of structures solved using the non-linear least square fit method will be given in section 7.

Though the number of trial structures is dramatically reduced with the automated search described above, there is a clear drawback. When the parameters are varied systematically a in a grid search, one can make multiple use of costly energy-dependent quantities, such as, e.g., layer diffraction amplitudes, before this quantity is calculated for the next energy. This advantage has to be given up in the automated search because for a new set of parameters the data at all energies are needed for the comparison to experiment and for the decision where to move next in parameter space. A way out of this situation is the use of tensor LEED together with a directed search as was accomplished by the Berkeley group (Rous *et al* 1990, Van hove *et al* 1993) and is displayed by the flowchart given in figure 25. For a certain reference structure, which is chosen in a promising area of the parameter space, the tensor is calculated and stored for each energy and beam needed as well as for each atom to be displaced from the reference position. The intensities for a trial structure are calculated and compared to experiment by the Pendry *R*-factor. A steepest descent method is used to reach the next trial structure point in parameter space. For this the Rosenbrook algorithm (Press *et al* 1986) is used which does without derivatives. This is found advantageous because of the presence of some noise ($\Delta R_p=0.001$) due to computational rounding errors. The procedure described is iterated until an *R*-factor minimum is reached. If on the way to the minimum the validity range of tensor LEED is left, a new reference calculation becomes necessary. Also, as the minimum eventually found need not to be the global minimum, it is recommended to repeat the entire search procedure starting with different reference structures well separated in parameter space. The deepest minimum found is believed to correspond to the correct model as long as the *R*-factor level reached is satisfactory. Figure 26 shows the progress of convergence for the system $(\sqrt{3}\times\sqrt{3})R30°$-CO/Pd(111). Yet, much more complex structures with many more parameters have been solved with the above method. Examples will be given in section 7. An alternative approach recently proposed to use linear LEED as an approximation to calculate trial structure intensities (Kothari *et al* 1994). The non-polynomial scaling of the parameter space scan is overcome by iterative optimization of a probability distribution for the trial structures. Though promising, the method up to now has been applied to only one test structure.

As mentioned one can never be sure that the best fit model found corresponds to the global best fit. This is an intrinsic feature because there is no mathematical criterion

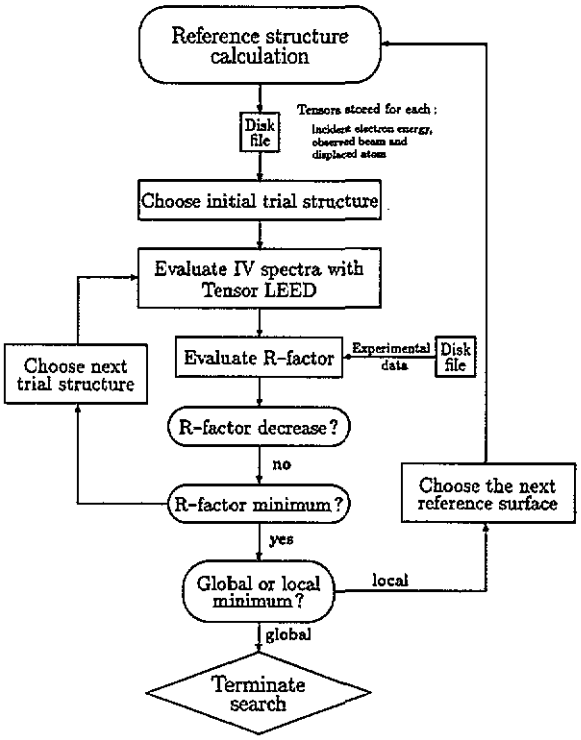

Figure 25. Flowchart for the *R*-factor optimization using tensor LEED (Rous *et al* 1990).

whether a minimum is local or global. Even with the grid search one can land in a local minimum if the span of the parameter space chosen was too small. Efforts to get around this problem, e.g., by application of a simulated annealing procedure (Press *et al* 1986) which makes large random jumps in parameter space, have only started. Also, at present methods following evolution strategies are discussed. However, it should be emphasized that none of the automated search procedures described or in sight is push-button safe. In spite of their high degree of automation they need the investigator's experience with respect to the selection of the parameter space and proper starting points as well as to the critical judgment of intermediate and final results. Of course, the same is true for automated techniques used for the measurement.

6.3. Inversion of linear tensor LEED as a direct method

In favourable cases it is possible to establish a model with parameter values very near the correct structure either by pre-information from other structural techniques, from the knowledge of related structures, or simply by a good guess. Then linear tensor LEED can be applied with these model parameters serving as the reference. Using equation (5.6) in a more general sense, i.e. replacing the geometrical displacement by a general parameter δp_i which with respect to the reference p_{i0} describes changes of atom i due to geometrical displacement, chemical substitution, thermal isotropic or anisotropic vibrations or non-spherical scattering caused by some other reason, the amplitude for

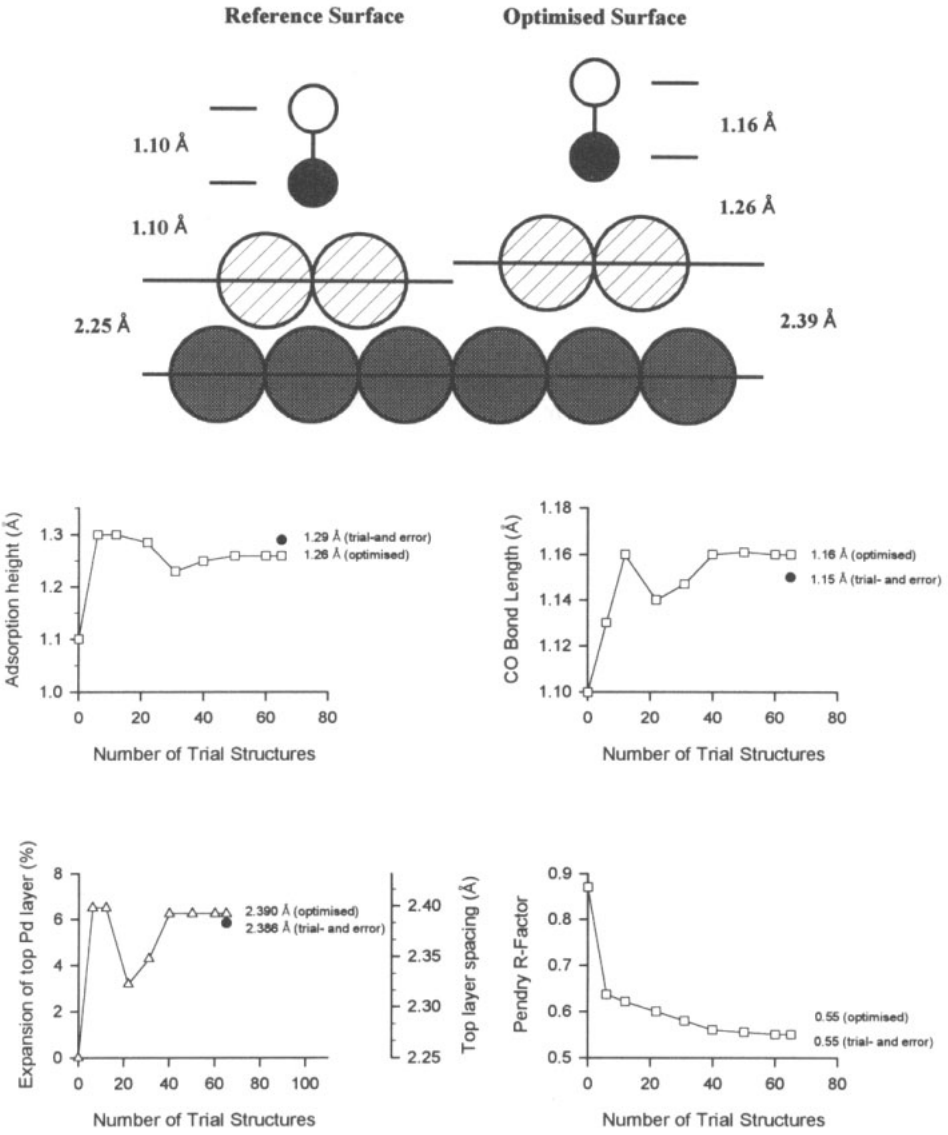

Figure 26. Top: structural model of $(\sqrt{3}\times\sqrt{3})R30°$-CO/Pd(111) with structural parameters given for the reference (left) and optimized (right) structure. Bottom: progress of the directed search using tensor LEED for the above structure as a function of the number of iterations (after Rous *et al* 1990).

the off-reference structure for a certain beam and energy labelled g is written as

$$A_g = A_{g0} + \sum_i T_{gi}\delta p_i \tag{6.3}$$

where A_{g0} is the amplitude of the reference structure. As the change of the amplitude is supposed to be small, the intensity can also be linearized yielding

$$I_g = I_{g0} + \sum M_{gi}\delta p_i \tag{6.4}$$

with $I_{g0}=|A_{g0}|^2$ and $M_{gi}=\mathrm{Re}[2(A_{0g})^* T_{gi}]$. Obviously, the matrix M_{gi} can be inverted to yield *directly* the wanted (general) displacement off the reference

$$\delta p_i=\sum_g (M_{gi})^{-1}(I_g-I_{0g}) \tag{6.5}$$

where for m unknown quantities δp_i the sum runs over m experimental data points I_g.

Evidently, this direct determination of the correct parameters $p_i=p_{i0}+\delta p_i$ needs at least as many data points as unknown quantities p_i. Ideally, each set of m data points $\{I_g\}$ should produce the same set of solutions $\{p_i\}$. However, this would only be true if both theoretical and experimental data were of ideal accuracy which, of course, is not the case. Therefore, in practice it has been found useful not to invert the matrix M_{gi} directly but to minimize the deviation between experimental and calculated intensities (or Y-functions). If this is done iteratively one can even account for the neglect of quadratic terms when the intensities (or Y-functions) are calculated from the amplitudes.

The above procedure has been proved to work for real space displacements $\delta p_i=\delta r_i$ (Pendry *et al* 1988, 1990b, Heinz *et al* 1990b, 1991b) as well as for chemical substitutions $\delta p_i=\delta c_i$ (Döll *et al* 1994b). As mentioned, the method works well for small displacements in real space as, e.g., in the determination of multilayer layer relaxation of low index metal surfaces where the bulk terminated surface serves as the reference. As an example the left-hand side of figure 27 displays the result for the first two interlayer distances of Rh(110), where the conventionally obtained values $(\Delta d_{12}/d_0, \Delta d_{23}/d_0)=(-6.9\%, +1.9\%)$ are closely approached by $(-5.7\%, +1.6\%)$ after a few steps of iteration (Pendry *et al* 1988). Also, the method is very helpful to retrieve small adsorbate induced displacive substrate reconstructions as determined for O/Ni(100) (Heinz *et al* 1990b), S/Ni(100) (Heinz *et al* 1991b), H/Rh(110) (Pendry *et al* 1990b) and O/Pt(111) (Döll 1994).

The direct method has been extended beyond the linear version of tensor LEED (Pendry and Heinz 1990) and applied to cases were not all adatoms reside precisely in the ideal adsorption site such as, e.g., due to thermal or other kinds of disorder. Then the probability function for the displacements off the ideal site can be determined by

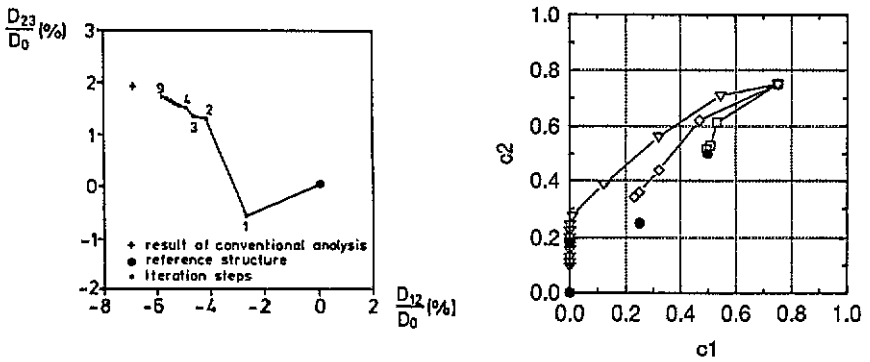

Figure 27. Left: two-layer surface relaxation of Rh(110) as determined through iteration by the direct method starting with the bulk terminated surface. Right: direct fit of data calculated for $Mo_{0.75}Re_{0.25}(100)$ with concentrations $c_{1,2}=0.50$, 0.25 and 0.00 in the first two layers as indicated by heavy points. The reference is the bulk stoichiometry $(c_1=c_2=0.75)$.

Fourier expansion of δt, or the moments $\langle(\delta r)^n\rangle$ for the displacements result by a power series expansion of δt in the atomic coordinates.

As demonstrated in section 5.2, chemical tensor LEED can handle rather large changes of concentrations by their linear relation to the diffraction amplitude (equations (5.8), (5.10)). This is ideal for the direct determination of the layer-dependent stoichiometry of, e.g., substitutionally disordered alloys (Döll *et al* 1994b). The right-hand side of figure 27 demonstrates for $Mo_{0.75}Re_{0.25}(100)$ that the Mo concentrations in the first two layers can be retrieved. The iterative fit is displayed for three test sets of data which are fully dynamically calculated for $c_{1,2}=0.50$, $c_{1,2}=0.25$ and $c_{1,2}=0$ as indicated by the full circles in the figure. Starting with the reference $c_{10}=c_{20}=0.75$ (bulk stoichiometry) a few iteration steps are sufficient to approach the sample stoichiometry very closely. This is also true for the application to real experimental data. Table 2 compares the Mo concentrations in the first four layers obtained directly and by conventional analysis.

Table 2. Comparison of Mo concentrations in the first four layers of $Mo_{0.75}Re_{0.25}(100)$ determined by trial and error and directly with the bulk concentration as reference.

	Results by trial and error	Results by the direct method
c_1	1.00 ± 0.14	0.97
c_2	0.53 ± 0.17	0.47
c_3	0.84 ± 0.22	0.81
c_4	0.76 ± 0.26	0.88

7. Accomplishments: accessible structural complexity and precision

With the above described modern tools for intensity calculations and the retrievement of the correct structure at hand rather complex surface structures have become accessible during the last decade. Clean and low index surfaces of elemental surfaces are structurally simple when unreconstructed, i.e. exhibit only some multilayer relaxation (examples of intensity calculations have been given in section 2.3). Higher index, i.e. stepped surfaces, however, cause unusual efforts even in the absence of reconstruction. This is because interlayer distances are too small to apply routine layer stacking procedures such as the layer doubling scheme. Complex structures were determined for clean but reconstructed elemental and compound semiconductor surfaces. There are heavy reconstructions extending deep into the surface as understandable through the covalent character of the chemical bonding. However, surface scientists had to learn that the reconstruction of clean metals can also extend to the second and third layer yielding rather complex atomic configurations. An additional degree of complexity comes for substitutionally disordered compounds, in particular random alloys which can show layer-dependent enrichment or depletion of their chemical constituents. Examples of all these types of structural complexity are given in section 7.1 whilst in 7.2 cases of adsorbate structures are presented. These are of medium complexity for atomic adsorbates when no reconstruction of the substrate is induced, i.e. when the original translational symmetry of the substrate is saved. However, the last decade has shown that adsorbate-induced reconstruction is rather the rule than the exception, whereby the reconstruction can be displacive with small local relaxations of the order of 0.1 Å or

even bond breaking with a local removal of atoms (Starke *et al* 1994). Small displacive reconstructions can happen even with molecular adsorbates which are chemically less aggressive than adatoms like hydrogen or oxygen. Even without substrate reconstruction, large adsorbed molecules are demanding cases for surface structure determination because there are many atoms in a large unit cell and the molecular configuration can be considerably distorted compared to the free molecule. Of course, coadsorption with other atoms or molecules makes the situation structurally even more complex. Anisotropic thermal vibrations of vertically bonded linear molecules prove to be important for the quality of the theory–experiment fit. Also, scattering from dipoles adsorbed or induced at the surface contributes to the intensities. As observed in a number of examples, adatoms may not simply reside on top of the first substrate layer, but can also substitute substrate atoms. This can lead to surface alloys with phases not existing in the bulk. On the other hand, multilayer epitaxial growth can also lead to new materials as well known for semiconductors from molecular beam epitaxy. This has been extended to metal-on-metal epitaxy where the structure of the epitaxial films is intimately correlated with, e.g., their magnetic properties. Whilst examples for all these phenomena connected with adsorption are given in section 7.2 the subject of accuracy and precision of the structure determination is raised in section 7.3.

7.1. Clean surfaces

Numerous structure determinations of clean surfaces in the last decade have shown that even adsorbate free surfaces exhibit a large variety of deviations of atoms from their bulk terminated positions. It appears that multilayer relaxation can extend deep into the surface and usually increases with the openness of the surface. Surfaces of compounds with more than one atom in the unit cell can buckle without losing the translational symmetry of the bulk terminated sample. In case of substitutionally disordered compounds there can be additional segregation or depletion of different constituents. *Surface reconstruction*, i.e. the change of translational symmetry, can happen both for elemental and compound surfaces, predominantly for semiconductors but also for a few metals. In all cases there is a high degree of complexity which can be detected by modern LEED as demonstrated by representative examples below.

7.1.1. Multilayer relaxation of unreconstructed low-index metal surfaces. Numerous structural investigations of clean metal surfaces have shown that they all show the phenomenon of *multilayer relaxation*, i.e. the change of distances between the first few layers of the solid compared to the bulk value whereby the translational symmetry is saved. These changes relax to zero with increasing layer depth (Jona and Marcus 1988, Marcus 1994). In many (though not all) cases the relaxation is oscillatory, i.e. layer distance contractions and expansions alternate until the bulk distance is reached. In the large majority of cases the top interlayer distance is contracted and the relative value of the contraction is the more pronounced the more open the surface. So, for the relatively open surface of, e.g., FCC(210) and BCC(210) the contraction of the top layer distance can be of the order of 20%. However, one has to keep in mind that high index surfaces correspond to stepped surfaces and so the simple picture of the distance relaxation of flat surface layers no longer applies. Conversely, close or nearly close packed surfaces like Ni(111), Ru(0001) or Fe(110) are only slightly contracted or practically bulk terminated. In very few cases also expansions of the first interlayer distance were reported such as, e.g., 3% for Pd(100) (Quinn *et al* 1990) and as large as

6% for Be(0001) (Davis *et al* 1992). As interlayer distances are parameters normal to the surface they can be determined with high accuracy and for distances more than five layers deep in the surface. Error limits given frequently are in the range of ±1% of the top interlayer distance and in favourable cases are even smaller than ±0.01 Å on the absolute scale. This in turn allows the check of first-principle total-energy calculations which in most cases are in line with the experimental result (for a recent overview see Feibelman 1994).

The relaxation saving the surface translational symmetry needs not to be exclusively normal to the surface. Atomic layers can move rigidly also parallel to the surface, a phenomenon labelled *registry shift* and observed only in rare cases (Jona and Marcus 1988, Van Hove *et al* 1986). The best investigated case is that of Fe(211) for which both lateral and vertical layer relaxations exist (Sokolov *et al* 1984). The registry shift of the top layer is in the $[1\bar{1}\bar{1}]$ direction by about 0.2 Å. Interestingly, every second atomic row close packed in this direction disappears by hydrogen adsorption, i.e. a missing row reconstruction is induced (Hassold *et al* 1995).

High-index surfaces are rather open and can be considered as stepped surfaces as demonstrated in figure 28 for a FCC(115) surface. On a microscopic scale the surface consists of facets of closer packed low-index surfaces as indicated. On the macroscopic scale, however, subsequent layers are very closely spaced with distances considerably below 1 Å. In this case the layer doubling method used to stack layers fails to converge, at least when there is strong multiple scattering between layers. An exception seems to be the example of Al(210) for which at a bulk distance of 0.90 Å layer doubling proved to work because of the comparably weak interlayer diffraction (Adams *et al* 1988). Therefore, in the usual case of strong multiple scattering, the stacking of layers has to be treated in real space rather than in reciprocal space. This can be approximated using a mixed method of calculation whereby multiple scattering in a thick composite layer is treated in real space spherical wave scattering theory with subsequent stacking of these composite layers as usual (Jepsen 1980, Sokolov *et al* 1985, Rous and Pendry 1986, MacLaren *et al* 1989). However, the full solution comes only by using real-space methods in the full surface which was done both by a real-space layer doubling scheme (Pinkava 1990, Pinkava and Crampin 1990) and by treating the full surface as a composite layer (Zhang *et al* 1990). The latter method was performed with additional use of tensor LEED (Zhang *et al* 1991) and by codes highly symmetrized in angular momentum space (Moritz *et al* 1995) whereby the multilayer relaxations of Pt(210) and Cu(115), respectively, were determined. The relative change of layer distances can be rather drastic and must not be alternating in sign for subsequent layers. In a simple picture this is due to the fact that the atoms in different (macroscopic) layers locally belong to different low-index surfaces and tend to relax according to the relaxation behaviour of

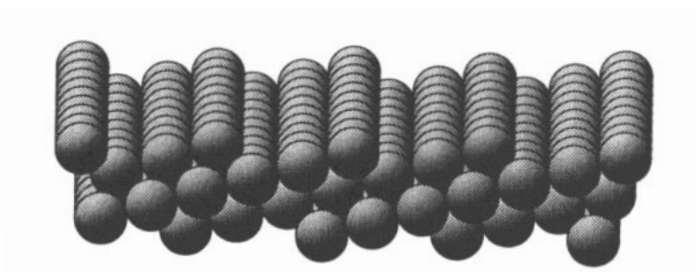

Figure 28. Structural model of an FCC(115) surface.

Table 3. Multilayer relaxation of some stepped surfaces with d_0 the bulk distance and Δd_{ik} the distance change between layers i, k.

	Al(311)[a]	Al(210)[b]	Pt(210)[c]	Fe(111)[d]	Cu(115)[e]	Fe(210)[f]
d_0 (Å)	0.926	0.903	0.877	0.827	0.696	0.641
$\Delta d_{12}/d_0$ (%)	−12	−16	−23	−17	−15	−22
$\Delta d_{23}/d_0$ (%)	−4	−1	−12	−10	−3	−11
$\Delta d_{34}/d_0$ (%)	+10	+9	+4	+4	+4	+17
$\Delta d_{45}/d_0$ (%)	−4	−4	−3	−2	−1	−5

[a] Adams and Sørenson (1986).
[b] Adams *et al* (1988).
[c] Zhang *et al* (1991).
[d] Sokolov *et al* (1986).
[e] Moritz (1995).
[f] Sokolov *et al* (1985).

the latter (Feibelman 1994, Williams 1994). Table 3 presents data of the multilayer relaxation of some stepped surfaces obtained with the methods described.

7.1.2. Geometrical relaxation of compound surfaces. The surfaces of compounds exhibit a much larger variety of atomic relaxations than elemental surfaces. The surface unit cell contains several atoms so that—additional to multilayer relaxation—different atoms can move differently without destroying the translational symmetry, i.e. without changing the geometry of the diffraction pattern. Of course this additional degree of freedom allows for additional complexity which is observed indeed and increases the computational demands for the structure determinations. Prominent candidates are compounds with covalent bonding, in particular the non-polar surfaces of semiconductors (for a recent review see Duke 1993) and also such insulators as metal oxides, whereby the relaxation can extend deep into the surface. Alloys show similar features though less pronounced (Gauthier and Baudoing 1990, Bardi 1994). Dependent on the surface orientation subsequent layers can be structurally non-equivalent, so that different surface terminations can coexist as determined for, e.g., $SrTiO_3(100)$ (Bickel *et al* 1989)

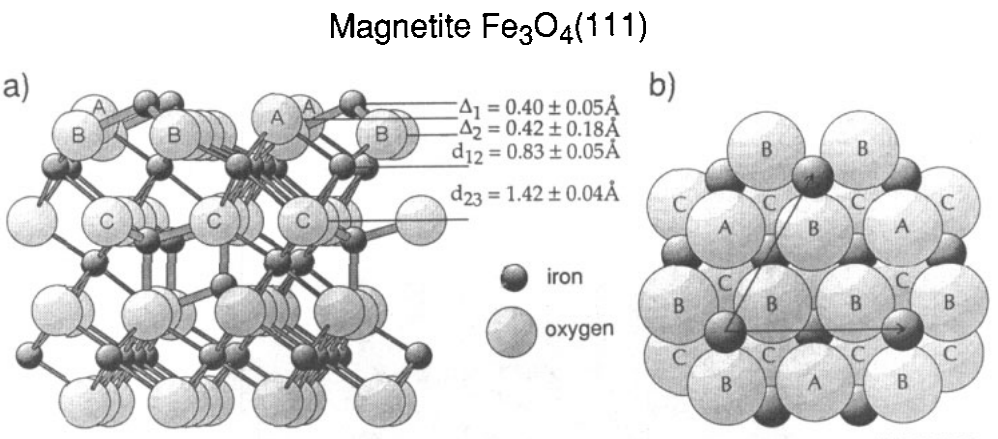

Figure 29. Structural model determined for a thin film of (111) oriented Fe_3O_4 grown on Pt(111) (after Barbieri *et al* 1994).

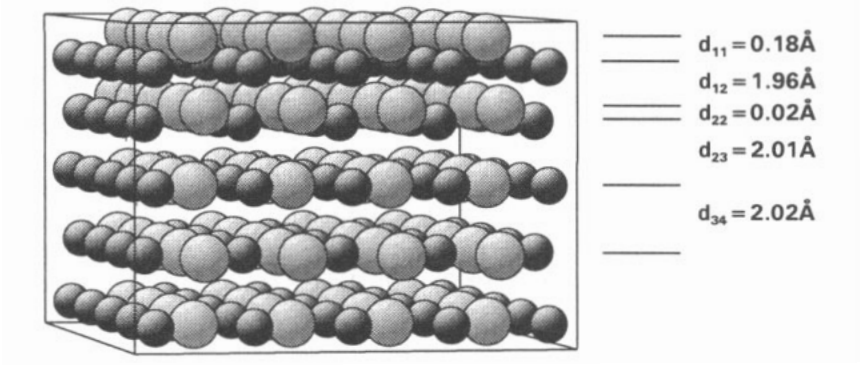

Figure 30. Rippled surface structure of CoAl(110) with the larger spheres representing A atoms (after Graupner *et al* 1995).

or for NiAl(111) (Davis and Noonan 1988). Different terminations put substantial demands to the *R*-factor analysis because this has to be calculated for any mixing of terminations. For insulators the acquisition of experimental data is problematic because of sample charging. A way out is the investigation of thin films deposited on a metallic substrate such as, e.g., recently accomplished for iron oxide which grown on Pt(111) develops the (111) surface of Fe_3O_4 (Barbieri *et al* 1994a). As displayed in figure 29 and retrieved by automated tensor LEED there is a strongly relaxed polar termination with iron atoms arranged over a distorted hexagonal close packed oxygen layer. A surface rippling was also found for mixed terminations of alloys such as, e.g., for NiAl(110) (Davis and Noonan 1988) and figure 30 displays the similar case of CoAl(110) with the rippling extending even to the second layer (Castro *et al* 1995). For Pt_3Ti an elemental flat termination was found with the mixed second layer buckled (Atrei *et al* 1992).

7.1.3. Chemical relaxation of alloys. Alloys can be both chemically ordered and disordered. As described in sections 2 and 4 LEED structure determination in the case of disorder still remains applicable by the use of weighted elemental averages of atomic *t*-matrices in spite of the loss of exact translational symmetry. In addition to multilayer relaxation chemical segregation and depletion takes place and can be determined for each layer separately. Numerous examples are given in the literature (Gauthier and Baudoing 1990, Bardi 1994) and table 4 displays the results for $Mo_xRe_{1-x}(100)$ which

Table 4. Mo concentrations and interlayer distance relaxations for the first four layers of Mo_xRe_{1-x} for $x = 0.75$, 0.85 and 0.85 (R_p is the Pendry *R*-factor in each case).

	$Mo_{75}Re_{25}(100)$	$Mo_{85}Re_{15}(100)$	$Mo_{95}Re_5(100)$
c_1 (Mo) (%)	100 ± 14	100 ± 15	96 ± 14
c_2 (Mo) (%)	53 ± 17	69 ± 15	80 ± 14
c_3 (Mo) (%)	84 ± 22	91 ± 18	96 ± 18
c_4 (Mo) (%)	76 ± 26	94 ± 23	100 ± 23
$\Delta d_{12}/d_0$ (%)	−11.6 ± 1.7	−11.0 ± 1.3	−10.7 ± 1.2
$\Delta d_{23}/d_0$ (%)	+4.7 ± 1.8	+4.3 ± 1.3	+3.0 ± 1.2
$\Delta d_{34}/d_0$ (%)	−2.8 ± 1.4	−3.3 ± 1.1	−2.0 ± 1.1
$\Delta d_{45}/d_0$ (%)	+3.4 ± 2.0	+2.8 ± 1.8	+1.5 ± 1.8
R_p	0.16	0.16	0.14

coincide when obtained conventionally (Davis *et al* 1991), by tensor LEED (Döll *et al* 1994a) as well as by its direct inversion (Döll *et al* 1994b). The error limits given result from the variance of the Pendry *R*-factor and are rather conservative for the concentrations. Also full chemical relaxation can take place as observed for TiAl(010) where Al replaces Ti to make the top layer all Al, while the second layer becomes all Ti (Wang *et al* 1995). The rearrangement of chemical species may even lead to new superstructures such as, e.g., found for $Pt_3Sn(111)$ (Atrei *et al* 1993a, b). Even the formation of an ordered underlayer was detected for a random substitutional alloy, $Cu_{85}Pd_{15}(110)$ (Lindroos *et al* 1990). All these examples nicely prove the chemical sensitivity of LEED.

7.1.4. Geometrical and chemical reconstruction. The truncation of bonds during the creation of a surface makes surface atoms search for new equilibrium positions. Besides the phenomenon of relaxation described above this may lead to atomic rearrangements which break the translational symmetry of the bulk terminated sample. The rearrangements can be displacive and/or bond breaking and the term *surface reconstruction* is used for both, though some authors apply it only for the latter case. Because of their covalent bonds very many semiconductor surfaces reconstruct, in particular when polar, where the reconstruction can extend deep into the surface (for recent reviews see, e.g., Duke 1993, Kahn 1994). An extreme case is the reconstruction of Si(111) with its large 7×7 supercell. The positions of 126 atoms in the first three layers were determined with a precision of better than 0.1 Å and 0.15 Å for the vertical and lateral coordinates, respectively (Huang *et al* 1988). As no structural search procedures were used, substantial pre-information from electron microscopy yielding a dimers–adatoms stacking faults model (Takayanagi *et al* 1985) was essential.

Though less numerous, metal surfaces are also observed to reconstruct. Again with normal incidence intensity data in-plane movements are determined with less accuracy than vertical displacements. So, the determination of the direction of the in-plane $c(2 \times 2)$ reconstruction of W(100) by full dynamical intensity analysis can be achieved only by the use of oblique incidence data (Schmidt *et al* 1992). Moreover, the power of today's quantitative LEED is also able to resolve the simultaneous appearance of layer dependent movements *and* chemical substitutions of atoms, i.e. the coupled geometrical and chemical reconstruction of a surface. An example of the accessible structural complexity is the (1×2) reconstruction of $Pt_{80}Fe_{20}(110)$ with as many as 26 parameters determined (Baudoing-Savois *et al* 1991). A missing row reconstruction in the top layer is accompanied by a buckling and pairing of atoms down to the fifth layer. Simultaneously, there is the usual multilayer relaxation and in addition a complex segregation behaviour of the chemical constituents dependent on the local structure in the different layers.

7.2. Adsorbates, adsorbate-induced reconstruction and growth of new materials

7.2.1. Atomic adsorbates. The structure determination of adsorbates is a standard procedure when the unit cell is small—as frequently in case of atomic adsorbates—and no adsorbate-induced reconstruction is involved. However, surface scientists had to learn during the last decade that the induction of substrate atomic movements by adsorbates is more the rule than the exception. A textbook case is that of O/Ni(100) where it was shown that neglect of the substrate reconstruction induced can even lead to a wrong adsorption site for the adatom (Oed *et al* 1989). The reconstructive movement of atoms

can be exclusively displacive with only modifications of the local bonding though the in-plane displacements can be as large as 0.4–0.5 Å as determined in the case of C/Ni(100) (Gauthier *et al* 1991) and buckling amplitudes of the order of 0.3 Å in the second substrate layer can be induced as found for N/W(100) (Bessent *et al* 1994). Even close packed surfaces can reconstruct (for a recent review see Starke *et al* 1994). Both the adatom–substrate bond length and the substrate reconstruction can be coverage dependent as retrieved in particular for alkali atoms adsorbed on metals (Over *et al* 1992*b*, *Gierer et al* 1992, Wedler *et al* 1993). Moreover, bond breaking reconstruction including the local removal of atoms can happen and is usually accompanied with additional displacive shifts. Reconstruction can also be lifted as found for Pd/Au(111) (Baddeley *et al* 1994). Occasionally, large unit cells with many structural parameters can result. Such structures can only be solved by the use of tensor LEED and/or effective structural search procedures. A rather complex example recently accomplished by quantitative LEED is that of $(2\sqrt{3}\times 2\sqrt{3})R30°$-6S/Re(0001) whose surface structural model with ten coordinates fitted is displayed on the left of figure 31 (Barbieri *et al* 1994c). A similar complex structure with an additional missing row reconstruction involved was solved recently for c(6 × 2)-O/Cu(110) with 13 coordinates fitted (Zuscke *et al* 1995). The structural complexity is even increased in the cases of adsorption on substitutionally disordered alloys where in addition to a geometrical reconstruction a chemical relaxation, i.e. a layer-dependent change of the surface stoichiometry, can take place. This is observed in the case of the missing row reconstruction $(2\times 1)O/Mo_{75}Re_{25}(100)$ as displayed on the right of figure 31 (only geometrical parameters are given). The oxygen adsorption site, the substrate layer reconstruction, buckling, paring and multilayer relaxation as well as the layer-dependent elemental concentrations can be safely determined with a convincing Pendry *R*-factor $R=0.24$ (Hammer *et al* 1995). Complex adsorption structures were also found for atomic adsorption on semiconductor surfaces such as, e.g., Au/Si(111) (Quinn *et al* 1992) or Ag/Ge(111) (Huang *et al* 1994).

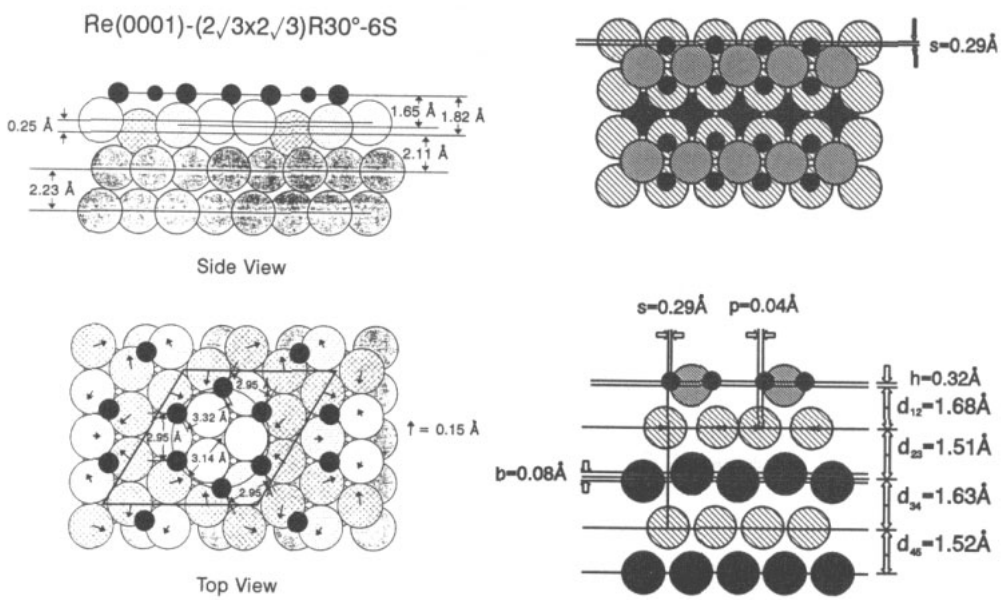

Figure 31. Structural model for $(2\sqrt{3}\times 2\sqrt{3})R30°$-6S/Re(0001) (left, after Barbieri *et al* 1994b) and for $(2\times 1)O/Mo_{75}Re_{25}(100)$ (right, after Hammer *et al* 1995).

A special case of structure determination is the positional detection of weak scatterers, in particular of hydrogen. Its scattering strength is only in the percentage region of that of, e.g., transition metal atoms and so the intensity of superstructure spots caused by hydrogen alone is rather low. With the sensitive intensity measurement techniques available today, however, the reliable measurement of spectra is possible. Usually, the intensities are increased by hydrogen-induced displacements of substrate atoms. Though this is favourable from the experimental point of view, it complicates the retrieval of the full structure: if the extra spot intensities are dominated by the contribution of a strong reconstruction the position of hydrogen often cannot be detected as experienced in the case of, e.g., H/Ni(110) (Kleinle *et al* 1987) or H/Fe(211) (Hassold *et al* 1995). In very many cases, and in spite of the chemical reactivity of hydrogen, the displacements are below 0.1 Å, and both the hydrogen position and the substrate reconstruction can be quantitatively determined (e.g., Hammer *et al* 1993, Heinz *et al* 1991c, Müller 1993). Because of the small displacements, the structure can be determined even directly by application of inverted tensor LEED. This has been demonstrated for (1 × 3)H/Rh(110) whose structure is displayed in figure 32. All atoms surrounding the hydrogen atom move by a few hundredths of an Ångstrøm (Döll 1994, Döll *et al* 1995).

7.2.2. Molecular adsorbates. Molecular adsorbates tend to influence the substrate less drastically than adatoms. However, as atomic shifts in the substrate are only to a less

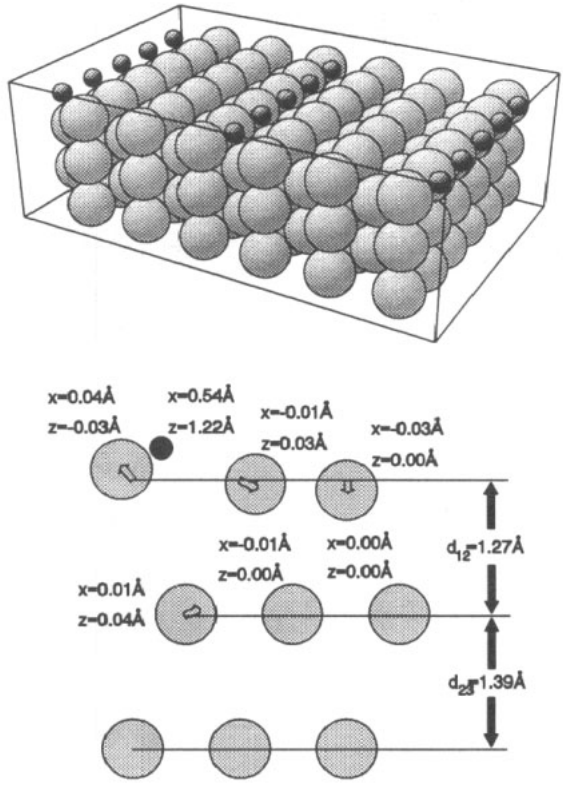

Figure 32. Structural model for (1 × 3)H/Rh(110) (after Döll 1994).

extent but still present, this makes no difference for the number of parameters to be determined. Even more, the arrangement of atoms within the molecule adds to the total structural complexity because the intramolecular bonding is modified by the new bonds to the substrate. By the early 1990s the modern techniques of intensity calculation and structural search allowed the determination of even coadsorption structures such as, e.g., (3×3)-$C_6H_6 + 2CO/Rh(111)$ (Barbieri *et al* 1994b) or (2×2)-$2O + CO/Ru(0001)$

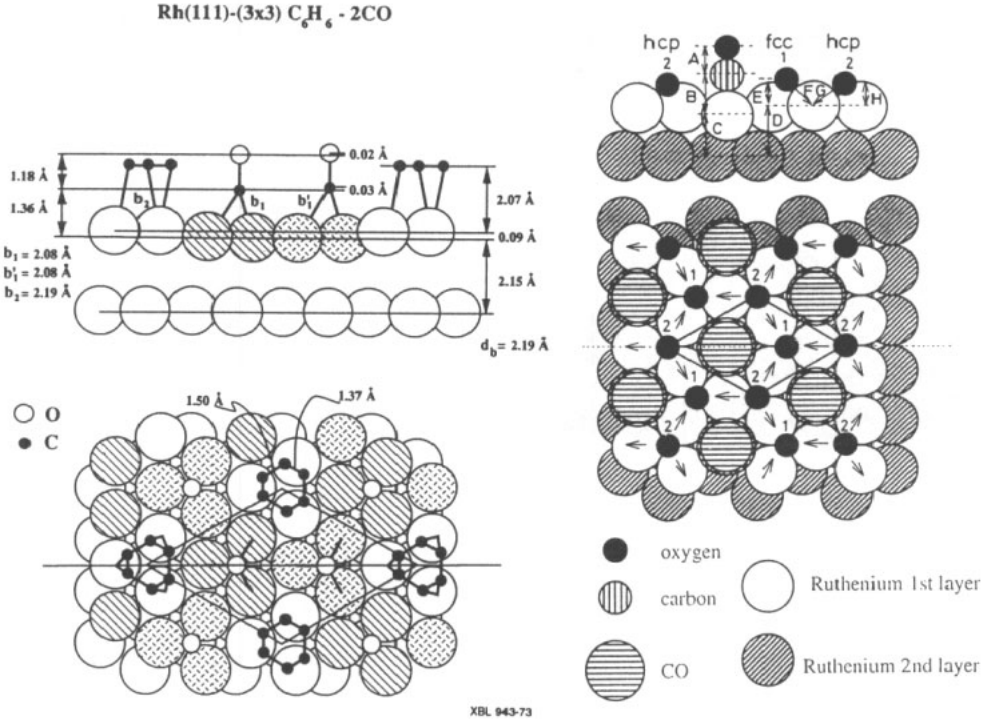

Figure 33. Structural models determined for $(3 \times 3) - C_6H_6 + 2CO/Rh(111)$ (left, after Barbieri *et al* 1994b) and for $(2 \times 2) - 2O + CO/Ru(0001)$ (right, after Narloch *et al* 1994).

(Narloch *et al* 1994) which both are displayed in figure 33. In particular molecules standing upright on the surface can have substantial and anisotropic vibrational amplitudes influencing the quality of the theory–experiment fit. Following the concept of *split positions*, i.e. a structural analysis considering the location of atoms most frequently occupied during their thermal vibration, it was possible for $(\sqrt{3} \times \sqrt{3})R30°$-CO/Ru(0001) to improve the *R*-factor whereupon a lateral vibrational amplitude of 0.4 Å was found for oxygen (Over *et al* 1993).

7.2.3. Adsorptive substitution and epitaxial growth. A special kind of reconstructive adsorption has been detected by quantitative LEED only very recently. Adatoms can substitute substrate atoms and so lead to the formation of a new compound material at least in the surface region and possibly not stable as a bulk phase. This adsorptive substitution was quantitatively determined by LEED for, e.g., the room temperature adsorption of K on Al(111) where the alkali atoms occupy substitutional sites of six-fold coordination and form a $(\sqrt{3} \times \sqrt{3})R30°$ superstructure (Stampfl *et al* 1992). Recent LEED work on (2×2)Na/Al(111) shows that room temperature adsorption of Na forms

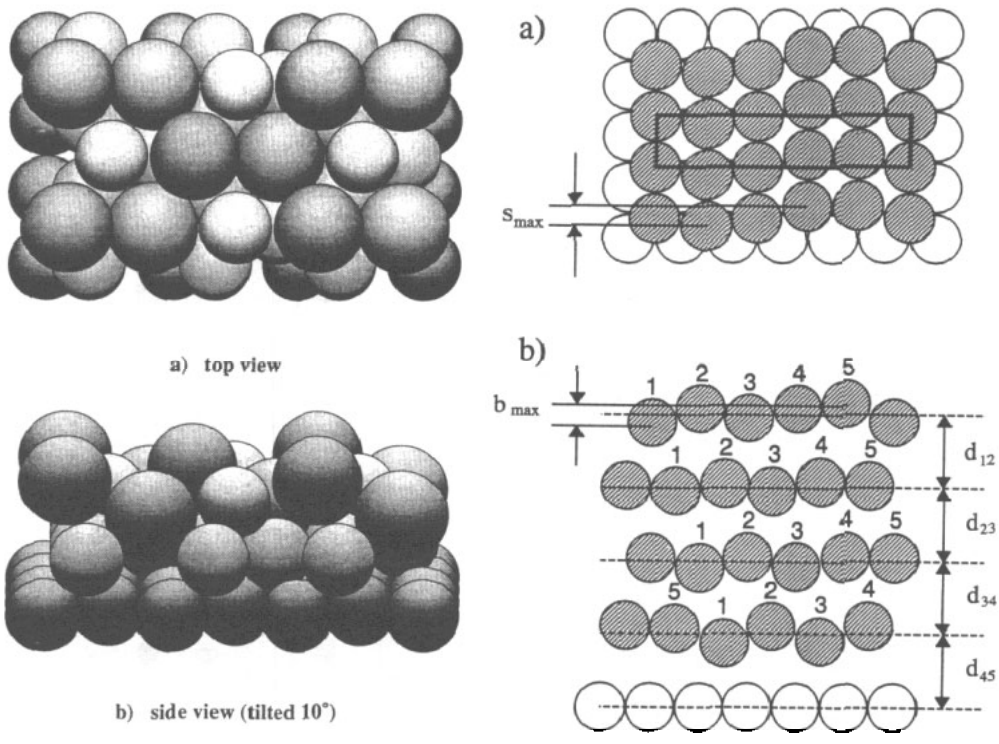

Figure 34. Left: model of the (2 × 2)NA/Al(111) surface (large spheres represent Al atoms). The top four layers, each of (2 × 2) periodicity, consist of a Na–Al–Na sandwich on a reconstructed Al layer with a (2 × 2) vacancy structure (Burchhardt *et al* 1995). Right: structural model of a four monolayer Fe film epitaxially grown on Cu(100). All Fe layers are both vertically and laterally reconstructed (Müller *et al* 1995a).

a surface alloy (Burchhardt *et al* 1995). As displayed on the left of figure 34 the first four layers consist of a Na–Al–Na sandwich on a reconstructed aluminium substrate layer. A complex mix of substitution and overlayer is also observed for (3 × 3)-5Li/Cu(100) (Mizuno *et al* 1995).

New materials can also be formed by epitaxial growth where, with respect to LEED crystallography, there was much concentration on metal-on-metal systems recently, last but not least because of the interesting magnetic properties such epitaxial films can exhibit. Films grown on cubic materials usually are tetragonally distorted due to epitaxial strain (Marcus and Jona 1994). The films can be under enormous strain and still remain crystalline (e.g., Li *et al* 1991). Of particular interest was the system Fe/Cu(100) which exhibits a considerable complexity and an intimate relation between structural and magnetic properties (Heinz *et al* 1995b, Zillgen *et al* 1995) where iron is distorted FCC for ultrathin films up to 10 monolayers where the transition to BCC takes place. In the low coverage regime the structure is rather complex as displayed for four monolayers of Fe in the right-hand panels of figure 34. All layers show substantial in-plane and vertical reconstructions so that as many as 40 coordinates must be determined for the atoms in the (5 × 1) unit mesh of the different layers. This could be accomplished recently by extensive use of tensor LEED showing also that the structural outcome is well in line with the magnetic properties of the film (Müller *et al* 1995a).

7.3. *Accuracy and precision*

The accuracy of quantitative LEED structure determination is hard to judge. Unfortunately, systematic errors possibly made in both the measurement and computation of intensities are only poorly known and cannot even be well estimated. Possible experimental errors are numerous and can come, e.g., by ill defined angles of incidence of the primary beam (possibly changing with energy because of residual magnetic fields), by inaccurate measurement of the electron energy, or by incomplete background subtraction. On the computational side, besides the approximations due to, e.g., the use of finite sets of spherical and plane waves or the description of electron attenuation by an optical potential, there are additional inaccuracies from the assumption of, e.g., spherical scatterers in the muffin-tin approximation, isotropic atomic vibrations or ideal cleanliness and lateral periodicity of the sample. So, the accuracy may only be judged by comparison of structural results with those achieved by other structure sensitive methods. Though these have deficiencies of their own a conservative overall estimate supported by experience is that the accuracy is better than 0.05 Å for the most sensitive structural parameters, i.e. vertical interlayer spacings.

About the same quantity holds for the precision of quantitative LEED, as can be estimated by the evaluation of different subsets of data for a certain structure under investigation. The precision is highest for atomic coordinates in the direction of the momentum transfer, i.e. coordinates normal to the surface for normal incidence data. Using appropriate off-normal data the precision can be extended to other coordinates but is rarely done because the angles of incidence are difficult to adjust precisely because the symmetry in the diffraction pattern is lost. A quantitative estimate of the precision comes by the use of standard deviations assuming statistical errors. Most frequently used is the variance of the Pendry R-factor (Pendry 1980, see also section 2.3). The precision achieved depends on the level of the minimum R-factor and the energy width of the data base as summed over all energy ranges for which independent beams have been measured. For simple structures the minimum R-factor can be $R < 0.1$ (e.g., Müller *et al* 1995b) which with a data base of several thousand eV can yield a precision of better than 0.01 Å for interlayer distances.

8. Reinterpretation of the DLEED pattern: an electron hologram?

8.1. *The adatom as a microscopic beamsplitter*

Optical holography is well known as an exciting technique for the storage and reconstruction of three-dimensional image information. Until relatively recently, holography using electrons has not had quite the same success as optical holography, in spite of the fact that the original ideas focused on the use of electrons rather than photons in order to improve the resolution of the electron microscope (Gabor 1948). Immediate success was prohibited by the short coherence length of electrons emitted by conventional electron sources. Being of the order of 100 Å, it prevents the straightforward application of holographic ideas because the path length difference between reference and object wave must not exceed the coherence length. However, recent developments of field-emission sources have given a new impetus to Gabor's original suggestion (Tonomura 1987, Orchowski *et al* 1995).

Novel proposals to circumvent the difficulty of short coherence length in order to allow the direct imaging of surface structures came up about ten years ago (Szoeke

1986). The key idea is to use an inner atomic source electron, which travels to the outside detector both directly (reference wave) and after scattering with the surrounding atoms (object wave). The interference of both waves forms a two-dimensional intensity distribution which is supposed to be an electron hologram, whereby the image of object atoms can be reconstructed on the computer. The inner source can be an atom excited to emit photoelectrons or Auger electrons and even Kikuchi electrons can be interpreted to be emitted from an atom. These ideas were quickly taken up both by theoreticians and experimentalists (Barton 1988, Harp *et al* 1990, Wei *et al* 1990, Thevuthasan *et al* 1991, Hu and King 1992) and subdisciplines such as photoelectron holography, Auger electron holography and Kikuchi electron holography developed (for recent reviews see Fadley 1993, Tong *et al* 1994, Wei *et al* 1994a).

In 1990 it was suggested to also interpret DLEED patterns as electron holograms (Saldin and de Andres 1990). The basic idea behind this comes from reinspection of the scattering processes responsible for the creation of diffuse patterns as displayed in figure 12. The last step, which ultimately leads to the formation of the diffuse intensity distribution, shows that an adsorbed atom can be interpreted as an inner electron source. It emits a wave directly towards the detector (reference wave) and via a final scattering by substrate atoms (object wave), and the diffuse pattern forms by their interference. Alternatively, as the true electron source is external, the adatom can be viewed as a *microscopic beamsplitter* which, as indicated in the left-hand panel of figure 35, creates a reference and an object wave. Their path difference is on a microscopic scale so that the limited coherence length is of no importance. In the kinematic approximation and with the origin of coordinates centred at the adatom the interference amplitude can be written as

$$R_{K0} + O_0 \exp(ikr_s - i\boldsymbol{k}_f \cdot \boldsymbol{r}_s) \tag{8.1}$$

where $\boldsymbol{r}_s$ denotes the position of substrate atoms, k is the modulus of the wave vector and $\boldsymbol{k}_f$ the wave vector into the final direction towards the detector. Supposing that the amplitudes R_{K0} and O_0 are almost isotropic, i.e. independent of $\boldsymbol{k}_f$, the intensity except for a constant term contains the interference terms

$$I(k, \boldsymbol{k}_f) \sim (R_{K0})^* O_0 \exp(ikr_s - i\boldsymbol{k}_f \cdot \boldsymbol{r}_s) + \text{conj. compl.} \tag{8.2}$$

A holographic wavefront reconstruction method as first proposed for photoelectron holography (Barton 1988), equivalent to a phased Fourier transform is used,

$$A(\boldsymbol{r}) = \left| \int I(k, \boldsymbol{k}_f) \exp(i\boldsymbol{k}_f \cdot \boldsymbol{r})\, \mathrm{d}\boldsymbol{k}_{f\parallel} \right|^2. \tag{8.3}$$

With the integration made for fixed energy over the surface parallel component of $\boldsymbol{k}_f$, an image function $A(\boldsymbol{r})$ results which should peak at the positions $\boldsymbol{r} = \boldsymbol{r}_s$ and $\boldsymbol{r} = -\boldsymbol{r}_s$ and so should produce a real and a twin image of the surface atom positions.

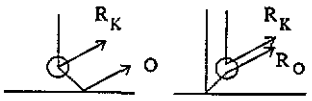

Figure 35. Scattering processes for the holographic interpretation of diffuse patterns.

8.2. Failure of image reconstruction from single energy diffuse patterns

Though the above procedure applied to DLEED data looked promising when proposed (Saldin and de Andres 1990), it generally failed to produce reliable information about the surface structure. Applications to test cases, for which the structure was known from conventional analyses, showed that the image function can have peaks considerably displaced from the true atomic positions or may even have only little resemblance to the real structure (Mendez *et al* 1992). The reason for this is mainly due to the fact that the assumption that the reference wave amplitude is isotropic—and so is well defined—does not hold. The scattering processes indicated in the left panel of figure 35 are incomplete, an important contribution adds to the reference wave as indicated in the right-hand panel of the figure which shows that the true reference wave $R = R_K + R_O$ includes a contribution R_O determined by the (unknown) object.

This has important consequences as demonstrated by model calculations performed for the adsorption system K/Ni(100) (Heinz *et al* 1993). Figure 36 in the top panel displays the kinematic reference wave R_K which, as assumed so far, exhibits a high degree of isotropy. However, when the object influenced part R_O of the reference wave is added—where fully dynamical scattering in the substrate is considered—a strong anisotropy develops as displayed in the second panel. This is because both, R_K and R_O, are of the same order of magnitude as both processes have encountered only one backscattering event. Also, the object wave can be as large as the reference wave as demonstrated by the considerable change which results by the interference of both waves (third panel in figure 36). Consistently, the total interference pattern $|R_K + R_O + O|^2$ given in the bottom panel is different to all other intensity distributions shown. Obviously, the integration over $k_{f\parallel}$ according to equation (8.3) makes processes additional to $|R_K + O|^2$ not or not sufficiently cancel when single energy data are used.

8.3. Multiple energy image reconstruction

A way out of the dilemma comes from the use of a larger data base, i.e. intensity maps taken at multiple energies. Again this was first suggested in the field of photoelectron holography (Barton 1991, Tong *et al* 1991a). In DLEED, multiple energy data more efficiently eliminate the disturbing process R_O by proper averaging (Wei and Tong 1992). This is done by introducing a stationary phase condition into the averaging integral

$$\phi(\boldsymbol{k}_f, \boldsymbol{k}_i, \boldsymbol{r}) = \int \chi(\boldsymbol{k}_f, \boldsymbol{k}_i) \exp(-ikr + i\boldsymbol{k}_f \cdot \boldsymbol{r}) k^2 \, dk \tag{8.4}$$

where $\boldsymbol{k}_i$ denote the incident wave vector and χ is the normalized difference intensity $\chi(\boldsymbol{k}_f, \boldsymbol{k}_i) = [I(\boldsymbol{k}_f, \boldsymbol{k}_i) - I_A(\boldsymbol{k}_f, \boldsymbol{k}_i)]/I_A(\boldsymbol{k}_f, \boldsymbol{k}_i)$ into the final direction with parallel momentum $\boldsymbol{k}_{f\parallel}$ and $I_A(\boldsymbol{k}_f, \boldsymbol{k}_i)$ the least-square straight line fit to $I(\boldsymbol{k}_f, \boldsymbol{k}_i)$ in the energy range used. The phase $(-kr + \boldsymbol{k}_f \cdot \boldsymbol{r})$ makes the first term in equation (8.2) dominate and so the integral produces strong peaks at the correct atomic positions. Other interference terms, in particular those introduced by R_O, are averaged out to a large extent (Wei and Tong 1992). The final image function is produced by summation over all measured directions $\boldsymbol{k}_f$

$$\phi(\boldsymbol{k}_i, \boldsymbol{r}) = \sum_f \phi(\boldsymbol{k}_f, \boldsymbol{k}_i, \boldsymbol{r}) \tag{8.5}$$

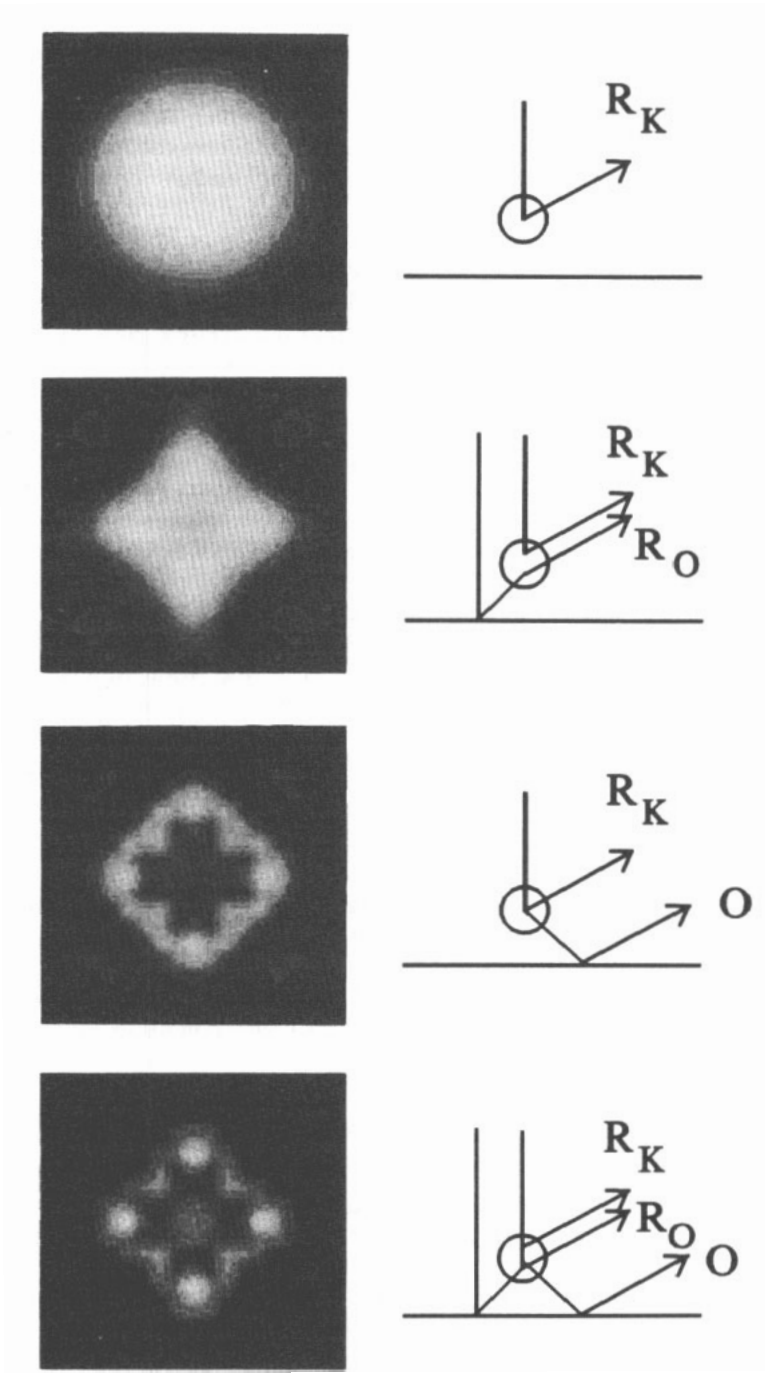

Figure 36. Contributions of different scattering processes for the formation of diffuse intensity distributions calculated at 150 eV for K residing at 2.66 Å adsorption height in the fourfold symmetric hollow position of Ni(100).

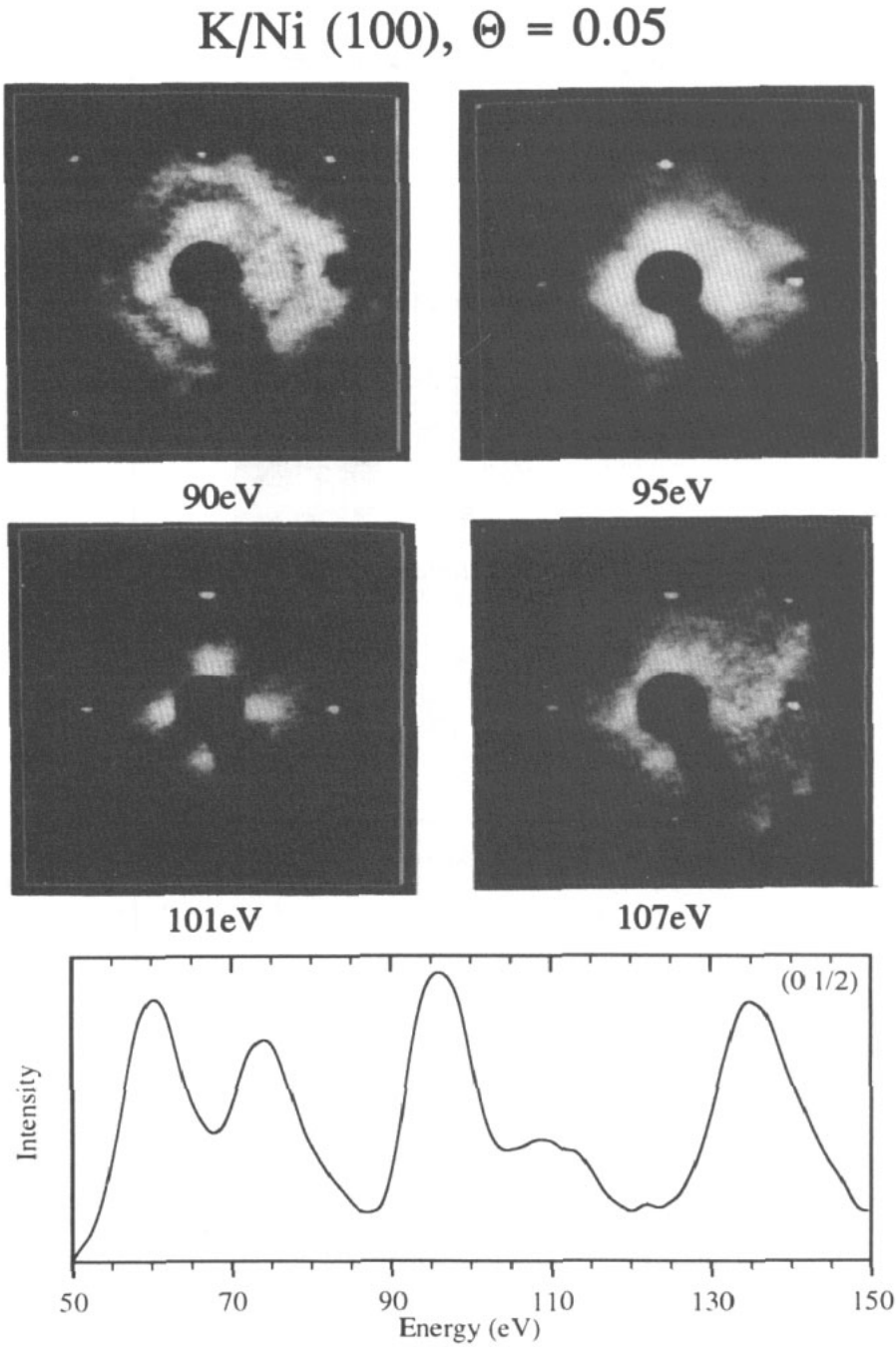

Figure 37. Clean surface corrected diffuse intensity maps for K/Ni(100) at coverage $\Theta_K = 0.05$ and temperature $T = 90$ K for the energies given. The bottom panel displays the $DI(E)$ spectrum for the $0\frac{1}{2}$ position.

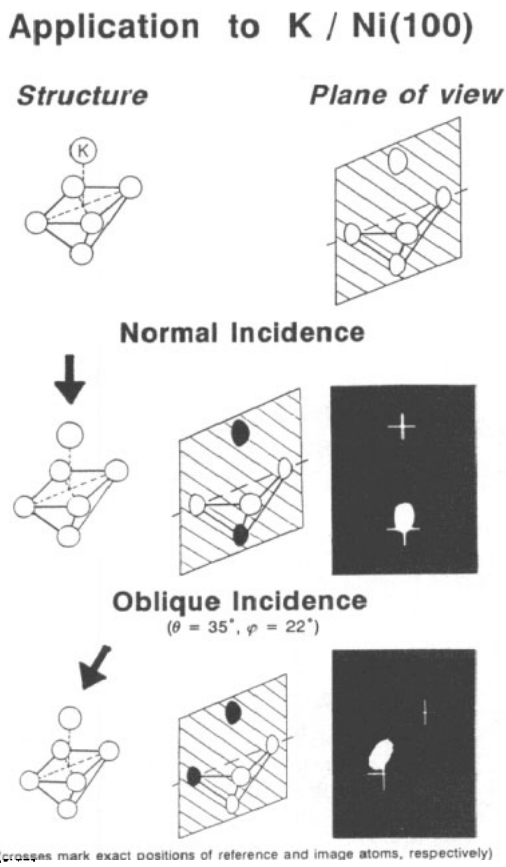

Figure 38. Atomic images reconstructed for K/Ni(100) for different angles of incidence of the primary beam. Upper and lower crosses mark the exact positions of the adatom (reference) and the substrate atom in the direction of the incident beam, respectively.

yielding eventually

$$A(\boldsymbol{k}_i, \boldsymbol{r}) = |\phi(\boldsymbol{k}_i, \boldsymbol{r})|^2 \tag{8.6}$$

which is still a function of $\boldsymbol{k}_i$. Because of the electron attenuation, only those atoms are supposed to show up in the reconstructed image which are near neighbours of the reference atom. The dependence on $\boldsymbol{k}_i$ means that predominantly those object atoms show up which are in the forward scattering cone of the adatom determined by the direction of incidence. So, the image reconstruction can be compared with a procedure in which the investigator sits on the adatom and illuminates the surrounding substrate atoms with a torch. Atoms only show up if they are hit by the torch light (Wei and Tong 1992).

The price to be paid for this successful image reconstruction is the measurement of diffuse data at many energies. Figure 37 presents some intensity maps which are corrected for the clean surface diffuse signal and are displayed for some consecutive energies equally spaced with respect to k ($\Delta k = 0.075$ au). The patterns change dramatically similar to the $0\frac{1}{2}$ $DI(E)$ spectrum displayed in the bottom panel. Diffuse data in the

range up to 180 eV were made to enter equations (8.4)–(8.6) after cut off and interpolation of the areas around the discrete substrate beams (Wei *et al* 1994b, Heinz and Wedler 1994). The resulting image with the atomic positions known from the conventional analysis (Wedler *et al* 1993) marked by crosses are displayed in figure 38 together with the structural model. The upper and lower panels are for normal and oblique primary beam incidence, respectively. Obviously, in each case only one image atom shows up. It is the near neighbour in the direction of the incident beam, i.e. the second substrate layer atom below the adatom for normal incidence and a top layer atom for oblique incidence. It is not critical to choose the oblique incidence direction (here arbitrarily $\vartheta = 35°$ and $\varphi = 22°$ were chosen) because it is sufficient that the atom to be imaged lies within the forward scattering cone. As indicated by the crosses, the image positions are displaced off the exact positions by about 0.4 Å. This is caused by the backscattering phaseshift of the illuminated atom. Its proper consideration is supposed to remove this shift (Tong *et al* 1991b).

Obviously, the object wave can be reliably reconstructed from multiple energy diffuse maps and this may justify the therm 'holography', though 'direct inversion' of diffraction data is also an appropriate name for the method. An advantage over other techniques such as, e.g., 'photoelectron holography' is that the measurement of diffuse data can be done in the home laboratory. However, it remains delicate because very weak signals and a large amount of data have to be recorded. The atomic images have a width of about 1 Å at half intensity maximum and so provide a good idea of what the structure under investigation is like. A structural refinement could be done by a conventional method as described in the preceding chapters. However, the above described case is only the first successful image reconstruction and the real strength of the method has yet to be proved by application to still unknown and less trivial structures.

9. Conclusion and outlook

As described, low energy electron diffraction remains a powerful surface structural tool even with the emergence of other structure sensitive techniques. The development of sophisticated experimental equipment for the fast and low dose measurement of diffraction intensities allows access to very accurate and reliable data. By the introduction of tensor LEED the computation of intensities was speeded up by orders of magnitude. A fast scan of the parameter space around a certain reference structure is possible where the differences with respect to the reference can be positional, chemical or vibrational. Rather complex structures can be solved with—in favourable cases—up to 40 model parameters to be determined. This is in particular true with the additional use of structural search procedures guided by R-factors for the quantitative theory–experiment comparison, though none of the automated search procedures or direct methods in use are push-button safe. For surface crystallography this is an important step forward. This is because LEED is one of the very few methods—if not the only one—which provides the full surface structure with high precision (frequently well below 0.1 Å) and not only special features such as, e.g., bond lengths or the top layer atomic arrangement. In addition to this substantial progress electron diffraction has been made applicable to the measurement and analysis of diffuse intensities (DLEED) which allows access to the local structure in the case of disordered adsorption on a crystalline substrate. This is both by the interpretation of two-dimensional intensity maps and by the conventional

analysis of diffuse intensity against energy spectra. Also, with the holographic interpretation of the diffuse pattern there seems to be a method at hand which provides atomic images in a direct way. However, it must be emphasized that this method is still in its infancy.

With all this progress made LEED is very likely to keep its important role with respect to the retrieval of surface structure in the future. Nevertheless, in spite of its present power and potential there is need for further development. Thermal vibrations, static disorder and non-spherical scattering should be considered routinely, and access should also be made to incommensurate structures. Moreover, compared to the complexity of structures approached by x-ray diffraction, the structures safely resolvable by LEED are relatively simple. Access to more complex structures, as they may appear in situations of technical relevance, requires an even higher degree of automation and the use of more sophisticated structural search procedures such as simulated annealing or the use of evolution strategies. Of course, faster computers working in parallel for, e.g., data at different energies certainly would be of help in this respect. Also, the use of LEED in parallel with other techniques, in particular with scanning tunnelling microscopy, should become more routine for access to very complex structures.

Acknowledgments

The author is indebted to many students of his research group and in particular to Mrs R Müller for technical help in producing the figures. He is also grateful to many colleagues who provided reprints and figures of their recent work concerning the determination of complex surface structures. Special thanks are due to Professor D K Saldin for reading the manuscript.

References

Aberdam D, Baudoing R and Gaubert C 1975 *Surface Sci.* **52** 125–50

Adams D L 1985 *Proc. 1st Int. Seminar on Surface Structure Determination by LEED (Erlangen)* ed K Heinz and K Müller pp 28–32

Adams D L, Andersen S P and Buchhardt J 1991 *The Structure of Surfaces III* ed S Y Tong, M A Van Hove, k Takayanagi and X D Xie (Berlin: Springer) pp 156–61

Adams D L, Jensen V, Sun X F and Vollesen J H 1988 *Phys. Rev.* B **38** 7913–31

Adams D L and Sørenson C S 1986 *Surface Sci.* **166** 495–511

Anderegg J W and Thiel P A 1986 *J. Vac. Sci. Technol.* A **4** 1367–71

Atrei A, Bardi U, Torrini M, Zanazzi E, Rovida G, Kasamura H and Kudo M 1993a *J. Phys. Condens. Matter* **5** L207–12

Atrei A, Bardi U, Wu J X, Zanazzi E and Rovida G 1993b *Surface Sci.* **290** 286–294

Atrei A, Pedocchi L, Bardi U, Rovida G, Torrini M, Zanazzi E, Van Hove M A and Ross P N 1992 *Surface Sci.* **261** 64–8

Baddeley C J, Barnes C J, Wander A, Ornerod R M, King D A and Lambert R M 1994 *Surface Sci.* **312** 54

Barbieri A, Jentz E D, Materer N, Held G, Dunphy J, Ogletree D F, Sautet P, Salmeron M; Van Hove M A and Somorjai G A 1994c *Surface Sci.* **312** 10–20

Barbieri A, Van Hove M A and Somorjai G A 1994b *Surface Sci.* **306** 261–8

Barbieri A, Weiss W, Van hove M A and Somorjai G A 1994a *Surface Sci.* **302** 259–79

Bardi U 1994 *Rep. Progr. Phys.* **57** 939–87

Barton J J 1988 *Phys. Rev. Lett.* **61** 1356–9

—— 1991 *Phys. Rev. Lett.* **67** 3106–9

Baudoing-Savois R, Gauthier Y and Moritz W 1991 *Phys. Rev.* B **44** 12977–90
Bessent M P, Hu P, Wander A and King D A 1995 *Surface Sci.* in press
Bickel N and Heinz K 1985 *J. Phys. C: Solid State Phys.* **18** 933–45
Bickel N, Heinz K, Landskron H, Rous P J, Pendry J B and Saldin K 1988 *The Structure of Surfaces II* ed J F van der Veen and M A Van Hove (Berlin: Springer) pp 19–25
Bickel N, Schmidt G, Heinz K and Müller K 1989 *Phys. Rev. Lett.* **62** 2009–11
Blackman G S, Xu M-L, Ogletree D F, Van Hove M A and Somorjai G A 1988 *Phys. Rev. Lett.* **61** 2352–5
Burchhardt J, Nielsen M M and Adams D L 1995 *Phys. Rev. Lett.* in press
Carvalho V E, Cook M W, Cowell P G, Heavens O S, Prutton M and Teat S P 1984 *Vacuum* **34** 893–7
Castro G R, Blum V, Rath C, Kottcke M, Hammer L and Heinz K 1995 *Verhandl. DPG VI* **30** 1640
Chinn M D and Fain S Jr 1976 *J. Vac. Sci. Technol.* **14** 314–7
Clarke L J 1985 *Surface Crystallography—An Introduction to Low Energy Electron Diffraction* (Chichester: Wiley)
Cowell P G and de Carvalho V E 1987 *Surface Sci.* **187** 175–93
Crampin S and Rous P J 1991 *Surface Sci. Lett.* **244** L137–42
Davis H L, Hannon J B, Ray K B and Plummer E W 1992 *Phys. Rev. Lett.* **68** 2632–5
Davis H L and Noonan J R 1988 *The Structure of Surfaces II* ed J F van der Veen and M A Van Hove (Berlin: Springer) pp 152–9
Davis H L, Zehner D M, Dötsch B, Wimmer A and Müller K 1991 *Bull. Am. Phys. Soc.* **36** 105
De Andres P L, Rous P J and Pendry J B 1988 *Surface Sci.* **193** 1–9
Demuth J E, Marcus P M and Jepsen D W 1975 *Phys. Rev.* B **11** 1460–74
Döll R 1994 *Thesis* Erlangen
Döll R, Kottcke M and Heinz K 1993 *Phys. Rev.* B **48** 1973–6
—— 1994b *Surface Sci.* **304** 309–15
Döll R, Kottcke M, Heinz K, Hammer L, Müller K and Zehner D M 1994a *Surface Sci.* **307–9** 434–9
Duke C B 1993 *Adv. Solid St. Phys.* **33** 1–36
—— (ed) 1994a *Surface Science: The First Thirty Years* (*Surface Sci.* **299/300**)
—— 1994b *Surface Sci.* **299/300** 24–33
Ertl G and Küppers J 1985 *Low Energy Electrons and Surface Chemistry* (Weinheim: Verlag Chemie)
Fadley C S 1993 *Surf. Sci. Rep.* **19** 231–64
Feibelman P J 1994 *Surface Sci.* **299/300** 426–32
Frenken J W M, Smeenk R G and van der Veen J F 1983 *Surface Sci.* **135** 147–63
Fritzsche V 1994 *Phys. Rev.* B **50** 1922–8
Gabor D 1948 *Nature* **161** 777
Gauthier Y and Baudoing R 1990 *Surface Segregation, Related Phenomena* ed P A Dowben and A Miller (Baton Rouge, LA: CRC) p 169
Gauthier Y, Baudoing-Savois R, Heinz K and Landskron H 1991 *Surface Sci.* **251/252** 493–7
Gauthier Y, Joly Y, Baudoing R and Rundgren J 1985 *Phys. Rev.* B **31** 6216–18
Gauthier Y, Joly Y, Rundgren J, Johansson L and Wincott P 1990 *Phys. Rev.* B **42** 9328
Gierer M, Bludau H, Hertel T, Over H, Moritz W and Ewrtl G 1992 *Surface Sci. Lett* **279** L170–4
Guo T, Atkinson R E and Ford W K 1990 *Rev. Sci. Instrum.* **61** 968–74
Hammer L, Landskron H, Nichtl-Pecher W, Fricke A, Heinz K and Müller K 1993 *Phys. Rev.* B **47** 15969–72
Hammer L, Seiferlein F, Dingfelder U, Kottcke M, Döll R, Heinz K and Müller K 1995 *Surface Sci.* in press
Harp G R, Saldin D K and Tonner B P 1990 *Phys. Rev. Lett.* **65** 1012–15
Hartner W 1994 *Diploma thesis* Erlangen
Hassold E, Löffler U, Schmiedl R, Grund M, Hammer L, Heinz K and Müller K 1995 *Surface Sci.* in press
Heilmann P, Lang E, Heinz K and Müller K 1976 *Appl. Phys.* **9** 247–51
Heinz K 1988 *Prog. Surface Sci.* **27** 239–326
—— 1990a *Vacuum* **41** 328–32
—— 1994 *Surface Sci.* **299/300** 433–46
Heinz K, Bayer P and Müller S 1995b *Surface Rev. Lett* **2** in press
Heinz K and Besold G 1983 *Surface Sci.* **125** 515–29
Heinz K, Bickel N, Besold G and Müller K 1985c *J. Phys. C: Solid State* **18** 933–45
Heinz K, Döll R and Kottcke M 1995a *Surface Rev. Lett.* accepted
Heinz K, Döll R, Wagner M, Löffler U and Mendez M A 1993 *Appl. Surf. Sci.* **70/71** 367–77
Heinz K and Müller K 1982 *Structural Studies of Surfaces* (*Springer Tracts Mod. Phys.* **91**) (Berlin: Springer) pp 1–53

Heinz K, Nichtl-Pecher W, Oed W, Landskron H, Michl M and Müller K 1991c *The Structure of Surfaces III* ed S Y Tong, M A Van Hove, K Takayanagi and X D Xie (Berlin: Springer) pp 401–5
Heinz K, Oed W and Pendry J B 1990b *Phys. Rev.* B **41** 10179–81
Heinz K, Oed W and Pendry J B 1991b *The Structure of Surfaces III* ed S Y Tong, M A Van Hove, K Takayanagi and X D Xie (Berlin: Springer) pp 139–43
Heinz K, Saldin D K and Pendry J B 1985b *Phys. Rev. Lett.* **55** 2312–15
Heinz K, Schmidt G, Hammer L and Müller K 1985a *Phys. Rev. B* **32** 6214–21
Heinz K, Starke U and Bothe F 1991a *Surface Sci. Lett.* **243** L70–3
Heinz K, Starke U, Van Hove M A and Somorjai G A 1992 *Surface Sci.* **262** 57–63
Heinz K and Wedler H 1994 *Surf. Rev. Lett.* **1** 319–34
Henzler M 1985a *Surface Sci.* **152/153** 963–76
—— 1985b *The Structure of Surfaces* (*Springer Ser. Surf. Sci.* **2**) (Berlin: Springer) pp 351–6
—— 1993 *Festkörperprobleme* **XIX** 193–208
Henzler M and Göpel W 1991 *Oberflächenphysik des Festkörpers* (Stuttgart: Teubner)
Hu P, Barnes C J and King D A 1992 *Phys. Rev.* B **45** 13595–8
Hu P and King D A 1992 *Nature* **360** 656
Huang H, Over H, Tong S Y, Quinn J and Jona F 1994 *Phys. Rev.* B **49** 13483–7
Huang H, Tong S Y, Packard W E and Webb M B 1988 *Phys. Lett.* **130A** 166–70
Ibach H and Lehwald S 1986 *Surface Sci.* **176** 629–34
Illing G, Heskett D, Plummer E W, Freund H-J, Somers J, Lindner Th, Bradshaw A M, Buskotte U, Neumann M, Starke U, Heinz K, de Andres P L, Saldin D K and Pendry J B 1988 *Surface Sci.* **206** 1–19
Jepsen D W 1980 *Phys. Rev.* B **22** 5701–17
Jona F and Marcus P M 1988 *The Structure of Surfaces II* ed J F van der Veen and M A Van Hove (Berlin: Springer) pp 90–9
Jona F, Strozier J A Jr and Marcus P M 1985 *The Structure of Surfaces* ed M A Van Hove and S Y Tong (Berlin: Springer) pp 92–9
Jona F, Strozier J A Jr and Yang W S 1982 *Rep. Prog. Phys.* **45** 527–85
Kahn A 1994 *Surface Sci.* **299/300** 469–86
Kleinle G, Moritz W, Adams D L and Ertl G 1989 *Surface Sci.* **219** L637–45
Kleinle G, Moritz W and Ertl G 1990 *Surface Sci.* **238** 119–31
Kleinle G, Skottke M, Penka V, Ertl G, Behm R J and Moritz W 1987 *Surface Sci.* **189/190** 177–84
Kothari N C, Over H and Saldin D K 1994 *Phys. Rev.* B **49** 11088–92
Lagally M G 1985 *Solid State Physics: Surfaces* vol **22** ed R L Park and M G Lagally (Orlando: Academic) pp 237–98
Lagally M G and Martin J A 1983 *Rev. Sci. Instrum.* **54** 1273–88
Lang E, Heilmann P, Hanke G, Heinz K and Müller K 1979 *Appl. Phys.* **9** 287–93
Le Bossé J C, Lopez J, Rousseau J, Zasada I and Wojtczak L 1990 *J. Phys. Condens. Matter* **2** 3143–65
Leonhard H, Gutman A and Hayek K 1980 *J. Phys. E: Sci. Instrum.* **13** 298–301
Li Y S, Quinn J, Li H, Tian D, Jona F and Marcus P M 1991 *Phys. Rev.* B **44** 8261–6
Lindroos M, Barnes C J, Bowker M and King D A 1991 *The Structure of Surfaces III* ed S Y Tong, M A Van Hove, K Takayanagi and X D Xie (Berlin: Springer) pp 287–92
Löffler U, Döller K, Heinz K and Pendry J B 1994 *Surface Sci.* **301** 346–52
Löffler U, Muschiol U, Bayer P, Heinz K, Fritzsche V and Pendry J B 1995 *Surface Sci.* in press
MacLaren J M, Crampin S and Vvedensky D D 1989 *Phys. Rev.* B **40** 12176–82
Marcus P M 1994 *Surface Sci.* **299/300** 447–53
Marcus P M and Jona F 1994 *Surf. Rev. Lett.* **1** 15–21
Marquardt D W 1963 *J. Soc. Ind. Appl. Math.* **11** 431–41
Martin C, Jelinsky P, Lampton M, Mailina R F and Anger H O 1981 *Rev. Sci. Instrum.* **52** 1067–74
McRae E G 1968 *Surface Sci.* **11** 479–91, 492–507
McRae E G and Malic R A 1986 *Surface Sci.* **177** 74–89
Mendez M A, Glück C, Guerrero J, De Andres P L, Heinz K, Saldin D K and Pendry J B 1992 *Phys. Rev.* B **45** 9402–5
Mendez M A, Glück C, Wagner M, Löffler U, Döll R and Heinz K 1993 *Surface Sci.* **290** 45–54
Meyer R J, Duke C B, Paton A, Kahn A, So E, Yeh J L and Mark P 1979 *Phys. Rev.* B **19** 5194–205
Mizuno S, Tochihara H, Barbieri A and Van Hove M A 1995 *Phys. Rev.* B in press
Moritz W 1995 Private communication to be published
Moritz W and Wolf D 1985 *Surface Sci.* **163** L655–65
Müller K 1993 *Prog. Surf. Sci.* **42** 245–255

Müller S, Bayer P, Kinne A, Schmailzl P and Heinz K 1995b *Surface Sci.* **322** 21–33
Müller S, Bayer P, Resichl C, Heinz K, Feldmann B, Zillgen H and Wuttig M 1995a *Phys. Rev. Lett.* **74** 765–8
Müller K and Heinz K 1985 *The Structure of Surfaces* ed M A Van Hove and S Y Tong (Berlin: Springer) pp 105–12
Muschiol U, Bayer P, Heinz K, Oed W and Pendry J B 1992 *Surface Sci.* **275** 185–9
Nagano S and Tong S Y 1985 *Phys. Rev.* B **32** 6562–70
Narloch B, Held G and Menzel D 1994 *Surface Sci.* **317** 131–42
Nichtl-Pecher W 1990 *Thesis* Erlangen
Nichtl-Pecher W, Gossmann J, Stammler W, Besold G, Hammer L, Heinz K and Müller K 1991 *Surface Sci.* **249** 61–74
Oed W, Lindner H, Starke U, Heinz K, Müller K and Pendry J B 1989 *Surface Sci.* **224** 179–94
Oed W, Rous P J and Pendry J B 1992 *Surface Sci.* **273** 261–70
Oed W, Starke U, Both F and Heinz K 1990 *Surface Sci.* **234** 72–8
Ogletree D F, Blackman G S, Hwang R Q, Starke U, Somorjai G A and Katz J E 1992 *Rev. Sci. Instrum.* **63** 104–13
Orchowski A, Rau W D and Lichte H 1995 *Phys. Rev. Lett.* **74** 399–402
Over H, Bludau H, Skottke-Klein M, Ertl G, Moritz W and Campbell C T 1992b *Phys. Rev.* B **45** 8638–49
Over H, Grierer M, Bludau H, Ertl G and Tong S Y 1994 *Surface Sci.* **314** 243–68
Over H, Ketterl U, Moritz W and Ertl G 1992a *Phys. Rev.* B **46** 13438–46
Over H, Moritz W and Ertl G 1993 *Phys. Rev. Lett.* **70** 315–18
Pendry J B 1974 *Low Energy Electron Diffraction* (London: Academic)
—— 1980 *J. Phys. C: Solid State Phys.* **13** 937–44
—— 1994 *Surface Sci.* **299/300** 375–90
Pendry J B and Heinz K 1990a *Surface Sci.* **230** 137–49
Pendry J B, Heinz K and Oed W 1988 *Phys. Rev. Lett.* **61** 2953–6
—— 1990b *Vacuum* **41** 340–2
Pendry J B and Saldin D K 1984 *Surface Sci.* **145** 33–47
Piercy P, Heimann P A, Michalk G and Menzel D 1989 *Surface Sci.* **219** 189–205
Pinkava P 1990 *Thesis* University of London
Pinkava P and Crampin S 1990 *Surface Sci.* **233** 27–34
Press W H, Flannery B P, Teukolksky S A and Vetterling W T 1986 *Numerical Recipes* (Cambridge: Cambridge University Press)
Quinn J, Jona F and Marcus P M 1992 *Phys. Rev.* B **46** 7288–91
Quinn J, Li Y S, Tian D, Li H, Jona F and Marcus P M 1990 *Phys. Rev.* B **42** 11348–54
Ri C-S and Watson P R 1992 *J. Vacuum Sci. Technol.* A **10** 2535–45
Rous P J 1992 *Prog. Surf. Sci.* **39** 3–63
Rous P J and Pendry J B 1986 *Surface Sci.* **173** 1–19
—— 1989a *Surface Sci.* **219** 355–72
—— 1989b *Surface Sci.* **219** 373–94
Rous P J, Pendry J B, Saldin D K, Heinz K, Müller K and Bickel N 1986 *Phys. Rev. Lett.* **57** 2951–4
Rous P J, Van Hove M A and Somorjai G A 1990 *Surface Sci.* **226** 15–25
Rundgren J and Salwén A 1975 *Comput. Phys. Commun.* **9** 312–26
Saldin D K and de Andres P L 1990 *Phys. Rev. Lett.* **64** 1270–3
Saldin D K, Pendry J B, Van Hove M A and Somorjai G A 1985 *Phys. Rev.* B **31** 1216–18
Scheithauer U, Meyer G and Henzler M 1986 *Surface Sci.* **178** 441–51
Schmidt G, Zagel H, Landskron H, Heinz K, Müller K and Pendry J B 1992 *Surface Sci.* **271** 416–26
Sokolov J, Jona F and Marcus P M 1985 *Phys. Rev.* B **31** 1929–35
—— 1986 *Phys. Rev.* B **33** 1397–404
Sokolov J, Shih H D, Bardi U, Jona F and Marcus P M 1983 *J. Phys. C: Solid State* **17** 371–83
Somorjai G A and Van Hove M A 1989 *Prog. Surf. Sci.* **30** 201–31
Stair P C 1980 *Rev. Sci. Instrum.* **51** 132–5
Stampfl C, Scheffler M, Over H, Burchhardt J, Nielsen M M, Adams D L and Moritz W *Phys. Rev. Lett.* **69** 1532–5
Starke U, de Andres P L, Saldin D K, Heinz K and Pendry J B 1988 *Phys. Rev.* B **38** 12277–82
Starke U, Bayer P, Hloch H and Heinz K 1989 *Surface Sci.* **216** 325–42
Starke U, Heinz K, Materer N, Wander A, Michle M, Döll R, Van Hove M A and Somorjai G A 1992 *J. Vac. Sci. Technol.* A **10** 2521–8

Starke U, Oed W, Bayer P, Bothe F, Fürst G, de Andres P L, Heinz K and Pendry J B 1991 *The Structure of Surfaces III* ed S Y Tong, M A Van Hove, K Takayanagi, X D Xie (Berlin: Springer) pp 427–31
Starke U, Van Hove M A and Somorjai G A 1994 *Prog. Surf. Sci.* **46** 305–19
Szoeke A 1986 *Short Wavelength Coherent Radiation: Generation and Applications* (*AIP Conf. Proc. No.* **147**) ed D T Attwood and K Boker (New York: AIP) pp 361–7
Thevuthasan S, Herman G S, Kaduwela A P, Saiki R S, Kim Y J, Niemczura W, Burger M and Fadley C S 1991 *Phys. Rev. Lett.* **67** 469–72
Tong S Y 1975 *Prog. Surface Sci.* **7** 1
—— 1994 *Surface Sci.* **299/300** 358–74
Tong S Y, Hua Li and Huang H 1994 *Surf. Rev. Lett.* **1** 303–18
Tong S Y, Huang H, Wei C M, Packard W F, Men F K, Glander G and Webb M B 1988 *J. Vac. Sci. Technol.* A **6** 615–24
Tong S Y, Li H and Huang H 1991a *Phys. Rev. Lett.* **67** 3102–5
Tong S Y, Van Hove M A and Mrstik B J 1977 *Proc. 7th Int. Vacuum Congr. & 3rd Int. Conf. on Surface Science* (*Vienna*) ed R Dobrozemsky, F Rüdenauera and F P Viehböck pp 2407–9
Tong S Y, Wei C M, Zhao T C, Huang H and Hua Li 1991b *Phys. Rev. Lett.* **66** 60–3
Tonomura A 1987 *Rev. Mod. Phys.* **59** 639–69
Van Hove M A 1988 *Chemistry and Physics of Solid Surfaces VII* ed R Vanselow and R F Howe (Berlin: Springer) p 513
Van Hove M A and Koestner R J 1984 *Determination of Surface Structures by LEED* ed P M Marcus and F Jona (New York: Plenum) pp 357–83
Van Hove M A, Lin R F and Somorjai G A 1983 *Phys. Rev. Lett.* **51** 778–81
Van Hove M A, Moritz W, Over H, Rous P J, Wander A, Barbieri A, Materer N, Starke U, Jentz D, Powers J M, Held G and Somorjai G A 1933b *Surface Sci.* **287/288** 428–31
Van Hove M A, Moritz W, Over H, Rous P J, Wander A, Barbieri A, Materer N, Starke U and Somorjai G A 1993a *Surface Sci. Rep.* **19** 191–229
Van Hove M A and Somorjai M A 1994 *Surface Sci.* **299/300** 487–501
Van Hove M A and Tong S Y 1979 *Surface Crystallography by LEED* (Berlin: Springer)
Van Hove M A, Weinberg W H and Chan C-M 1986 *Low Energy Electron Diffraction* (Berlin: Springer)
Walls J M (ed) 1989 *Methods of Surface Analysis* (Cambridge: Cambridge University Press)
Wander A, Pendry J B and Van Hove M A 1992 *Phys. Rev.* B **46** 9897–9
Wang C P, Kim S K, Jona F, Strongin D R, Sheu B-R and Marcus P M 1995 *Phys. Rev.* B in press
Watson P R, Van Hove M A and Hermann K 1994 *Atlas of Surface Structures Based on the NIST Surface Structure Database* (*J. Phys. Chem. Ref. Data Monograph* **5**) (American Institute of Physics)
Wedler H, Mendez M A, Bayer P, Löffler U, Heinz K, Fritzsche V and Pendry J B 1993 *Surface Sci.* **293** 47–56
Weeks S P, Rowe J E, Christmann S B and Chaban E E 1979 *Rev. Sci. Instrum.* **50** 1249–55
Wei C M, Hong I H nd Chou Y C 1994a *Surf. Rev. Lett.* **1** 335–58
Wei C M and Tong S Y 1992 *Surf. Sci. Lett.* **274** L577–82
Wei C M, Tong S Y, Wedler H, Mendez M A and Heinz K 1994b *Phys. Rev Lett.* **72** 2434–7
Wei C M, Zhao T C and Tong S Y 1990 *Phys. Rev. Lett.* **65** 2278–81
Welkie D G and Lagally M G 1979a *J. Vac. Sci. Technol.* **18** 784–8
—— 1979b *Appl. Surf. Sci.* **3** 272–92
Willimas E D 1994 *Surface Sci.* **299/300** 502–24
Woodruff D P and Delchar T A 1986 *Modern Techniques of Surface Science* (Cambridge: Cambridge University Press) ch 2
Yang W S, Jona F and Marcus P M 1983 *Phys. Rev.* B **27** 1394–6
Zhang X-G, Rous P J, Gonis A, MacLaren J M, Van Hove M A and Somorjai G A 1990 *Surface Sci.* **239** 103–18
Zhang X-G, Van Hove M A, Somorjai G A, Rous P J, Tobin D, Gonis A, MacLaren J M, Heinz K, Michl M, Lindner H, Müller K, Ehsasi M and Block J H 1991 *Phys. Rev. Lett.* **67** 1298–301
Zillgen H, Feldmann B and Wuttig M 1995 *Surface Sci.* **321** 32–46
Zuscke R, Zi Pu Hu, Wolf D, Moritz W, Fischer N, Dürr P and Fauster Th 1995 *Surface Sci.* submitted